AD-A246 890

PL-TR-91-2097

$E200 S$

WAVE PROPAGATION AT REGIONAL DISTANCES

Charles A. Langston

Pennsylvania State University
114 Kern Building
University Park, PA 16802

23 April 1991

DTIC
ELECTE
JAN 15 1992
S
B

Final Report
10 January 1989–30 April 1991

PHILLIPS LABORATORY
AIR FORCE SYSTEMS COMMAND
HANSCOM AIR FORCE BASE, MASSACHUSETTS 01731-5000

92-01223
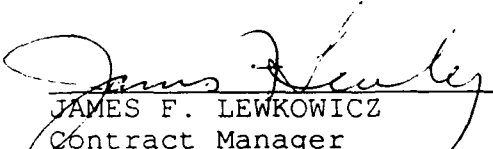
92 1 14 009

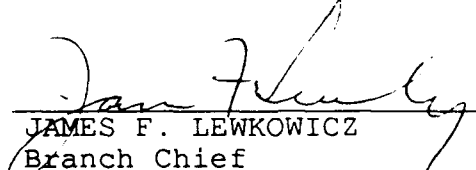This technical report has been reviewed and is approved for publication.

JAMES F. LEWKOWICZ
Contract Manager
Solid Earth Geophysics Branch
Earth Sciences Division

JAMES F. LEWKOWICZ
Branch Chief
Solid Earth Geophysics Branch
Earth Sciences Division

DONALD H. ECKHARDT, Director
Earth Sciences Division

REPORT DOCUMENTATION PAGE			*Form Approved* *OMB No. 0704-0188*

1a. REPORT SECURITY CLASSIFICATION		1b. RESTRICTIVE MARKINGS	
Unclassified			
2a. SECURITY CLASSIFICATION AUTHORITY		3. DISTRIBUTION/AVAILABILITY OF REPORT	
		Approved for public release;	
2b. DECLASSIFICATION/DOWNGRADING SCHEDULE		**Distribution unlimited**	
4. PERFORMING ORGANIZATION REPORT NUMBER(S)		5. MONITORING ORGANIZATION REPORT NUMBER(S)	
		PL-TR-91-2097	

6a. NAME OF PERFORMING ORGANIZATION	6b. OFFICE SYMBOL (If applicable)	7a. NAME OF MONITORING ORGANIZATION
Pennsylvania State University		**Phillips Laboratory**
6c. ADDRESS (City, State, and ZIP Code)		7b. ADDRESS (City, State, and ZIP Code)
114 Kern Building **University Park, PA 16802**		**Hanscom AFB** **Massachusetts 01731-5000**
8a. NAME OF FUNDING/SPONSORING ORGANIZATION	8b. OFFICE SYMBOL (If applicable)	9. PROCUREMENT INSTRUMENT IDENTIFICATION NUMBER
		F19628-89-K-0013

8c. ADDRESS (City, State, and ZIP Code)	10. SOURCE OF FUNDING NUMBERS			
	PROGRAM ELEMENT NO	PROJECT NO	TASK NO	WORK UNIT ACCESSION NO
	61101E	**9A10**	**DA**	**AG**

11. TITLE (Include Security Classification)

Wave Propagation at Regional Distances

12. PERSONAL AUTHOR(S)

Charles A. Langston

13a. TYPE OF REPORT	13b. TIME COVERED	14. DATE OF REPORT (Year, Month, Day)	15. PAGE COUNT
FINAL	FROM **1/10/89** TO **4/30/91**	**1991 April 23**	**156**

16. SUPPLEMENTARY NOTATION

17.	COSATI CODES		18. SUBJECT TERMS (Continue on reverse if necessary and identify by block number)
FIELD	GROUP	SUB-GROUP	**Regional wave propagation Scattering P coda**
			Body waves Norres
			Surface waves Finite difference

19. ABSTRACT (Continue on reverse if necessary and identify by block number) **Broad-band, digital, teleseismic P-wave data from the University of California, Berkeley, stations BKS, MHC, and SAO are used to study the character of teleseismic P coda. Velocity heterogeneity in structure near these stations gives rise to a variety of scattering effects which include azimuthly dependent receiver functions, large tangential component particle motions, and high levels of P coda. P codas for shallow and deep teleseisms are analyzed for three frequency bands centered at 1.5, 0.75, and 0.375 hz. Observed coda decay rate and level are fit with an energy flux theory to parameterize scattering effects near the source and at the receiver. Coda decay rate and level for deep earthquakes are seen to be stable observables between stations, implying that the scattered coda field is homogeneously distributed over the receiver network validating a major assumption in the energy flux model. Scattering Q, Q_s is not particularly well constrained by the data and is inferred to be affected by focusing and defocusing effects of the direct P-waves.**

20. DISTRIBUTION/AVAILABILITY OF ABSTRACT	21. ABSTRACT SECURITY CLASSIFICATION
☐ UNCLASSIFIED/UNLIMITED ☒ SAME AS RPT ☐ DTIC USERS	**Unclassified**
22a. NAME OF RESPONSIBLE INDIVIDUAL	22b. TELEPHONE (Include Area Code)	22c. OFFICE SYMBOL
James Lewkowicz		**PL/LWH**

DD Form 1473, JUN 86   *Previous editions are obsolete*   SECURITY CLASSIFICATION OF THIS PAGE

There is a pronounced difference in coda decay rate between shallow and deep earthquakes for 1.5 hz coda where coda decay rate for deep events is about a factor of two greater than for shallow events. There is no difference in coda decay rate between the two pupulations of events in the lower frequency bands. The observation at 1.5 hz is consistent with a simple model of P-wave coda formation where most coda forms in a scattering layer near the surface of the earth in regions near the source and near the receiver. The homogeneity of coda decay at 0.75 and 0.375 hz for deep shallow events suggests that a large, near-receiver scattering mechanism, such as surface wave formation, dominates the coda.

Events recorded by NORESS are analyzed to determine the velocities and times of coherent crustal phases to be used in accurate locations and determination of crustal structure. The events straddle two azimuthal directions, and range in distance from 50 to 300 km, thus sampling two cross-sections of the crust and upper mantle; one in the Caledonides to the north west of NORESS, and the other to the south along the eastern rim of the Oslo Graben. F-k analysis is used to search for coherent phases in the data. All vertical channels are then stacked with the appropriate time delays calculated from the phase velocities and azimuths obtained for the coherent arrivals. Finally, a composite seismogram is made for each event by piecing together time sections from the stacks, where each time piece represents a coherent arrival. All detectable coherent phases are enhanced in the composite seismograms and on closer inspection it is possible to improve some of the locations from the NORESS bulletin. This causes a number of events to group together to the same location. Travel time curves are constructed from plane layered homogeneous models to match travel times and phase velocities in the composite seismograms.

Numerical simulations of teleseismic wave propagation in a heterogeneous layer over a homogeneous half-space are conducted to further understanding of teleseismic coda generation and complex teleseismic particle motions. Acoustic and elastic finite difference synthetics are generated for more than 150 different layer over a half-space models. The models vary in scattering layer thickness (L), heterogeneity correlation distance(s) (a, or a_x, a_z), and heterogeneity standard deviation (σ). The synthetic data are examined using relative coda intensity envelopes, to determine relationships that exist between the model parameters and the level and rate of coda decay, and frequency-wavenumber analysis to determine the wave types present in the scattered wavefield. The level of scattered energy is found to be controlled by the ka value and the magnitude of the standard deviation of the perturbations. Coda levels increase with ka from $ka < 1$ to $ka \sim 1$, and decrease with increasing ka for $ka > 1$. Scattered energy levels are found to always increase with increasing A more complex relationship is found to exist between the coda level and decay rate, and variations in the scattering layer thickness. For models that vary in scattering layer thickness alone, coda level and decay rate changes did not occur independently of the values of ka and/or σ. The rate of coda decay is found to be controlled by the aspect ratio (a_x/a_z) of the heterogeneities (spatial anisotropy). The two extreme models are those with homogeneous plane-layers, which exhibit the most rapid coda decay rates, and those with spatially isotropic heterogeneities ($a_x/a_z = 1$), which exhibit the slowest decay rates. Acoustic and elastic models exhibit similar coda intensity envelope characteristics. Apparent scattering attenuation of the direct pulse is found to be strongest for models with spatially isotropic heterogeneities. Frequency-wavenumber analysis of the elastic synthetics reveals the mechanism responsible for the generation of coda in the synthetic data. For models with spatially isotropic heterogeneities, the coda is composed largely of low apparent

velocity (LAV) waves (scattered S and possibly body-to-surface scattered waves) while the coda for models with homogeneous plane-layers is composed solely of vertically propagating layer reverberations. Decreasing the heterogeneity aspect ratio increases the total amount of scattered LAV energy produced. The onset time of the LAV energy is also controlled by the heterogeneity aspect ratio. For models with spatially isotropic heterogeneities, the LAV energy appears immediately after the initial arrival. For models with homogeneous, plane-layers, LAV energy never appears.

Teleseismic data recorded at the NORESS seismic array are examined to determine the degree and scale of lithospheric heterogeneities beneath the array, and to locate local scattering sources. The data are examined using relative coda intensity envelopes, frequency-wavenumber spectra, and particle motion polarizations. The coda intensity envelopes do not exhibit any clear ka trends; the 0.5 Hz pass-band data does, however, contain higher energy levels and a high energy packet ~ 15 seconds after the first arrival. Frequency-wavenumber analysis shows the most of the teleseismic coda is vertically propagating. The window centered near 15 seconds, however, contains energy travelling to the north-east at a low apparent velocity. Particle motions in this window follow a retrograde elliptical pattern characteristic of Rayleigh surface waves. The scattering source presumed to be responsible for the observed body-to-surface wave scattered energy is Lake Mjosa, located approximately 50 km west-southwest of the array.

Accession For

NTIS GRA&I	☑
DTIC TAB	☐
Unannounced	☐
Justification	

By
Distribution/

Availability Codes

| Dist | Avail and/or Special |
| A-1 | |

iii

Table of Contents

List of Scientists Contributing to Research in This Report

Charles A. Langston, P.I.
Charles J. Ammon, Research Assistant
Kristin S. Vogfjord, Research Assistant
Gregory S. Wagner, Research Assistant

List of Previous Contracts Related to This Research

Calculation of Source and Structure Parameters at Regional and Teleseismic Distances, Contract #F19628-87-K-0024

List of Publications Supported by This Contract

Vogfjord, K.S., and C.A. Langston, Analysis of regional events recorded at NORESS, Bull. Seism. Soc. Am., 80:2016-2031 (1990).

Langston, C.A., and C.J. Ammon, Scattering of teleseismic body waves along the Hayward-Calaveras fault system, Bull. Seism. Soc. Am., 81:576-591 (1991).

Wagner, G.S., and C.A. Langston, Scattering effects for teleseismic plane wave propagation in a heterogeneous layer over a homogeneous half-space, submitted to Geophysical Journal International (1991).

Wagner, G.S., and C.A. Langston, Body-to-surface wave scattered energy in teleseismic coda observed at the NORESS seismic array, submitted to Bull. Seism. Soc. Am. (1991).

Report Summary

Task Objectives

Characterization of local and regional wave propagation in the lithosphere around the NORESS array.

Theoretical and observational study of teleseismic P-wave coda near seismic receivers.

Technical Problem

Small aperture seismic arrays, like the NORESS array, are central in the problem of underground nuclear test detection, discrimination and yield estimation. Array geometries allow an analysis of the wave field of propagating high frequency regional waves which can be used to determine source location and size. Integral to the location problem is detailed knowledge of wave propagation through the crust and mantle between the source and array. The accuracy of a location is intimately tied to simple identification of discrete phases which arrive at the array which are used to estimate source distance and azimuth. This work addressed several fundamental seismological problems in wave propagation dealing with the identification of important phases in the NORESS data and propagation of those phases through the crust and mantle.

We examined two broad areas of wave propagation important in characterizing the nature of wave propagation at regional distances. The first was a fundamental observational study of seismic wave propagation near NORESS. Basic observational data were needed to analyze the excitation and behavior of common regional phases such as Pn, Pg, Sn, Lg and Rg. The other general area approached the problem of the effect of wave scattering in the crust and mantle and how it could be characterized using a "simpler" data set consisting of teleseismic P waves. A working assumption was that observation of near-receiver scattering in teleseismic P wave coda could help characterize the general nature of scattering due to near-receiver velocity

heterogeneity for local and regional events. Teleseismic NORESS data were incorporated in this aspect of the observational study.

General Methodology

The study of local and regional phases was performed through direct observation using NORESS data and applying array processing techniques. Theoretical studies of wave propagation in layered media were performed using computer simulation to examine the expected nature of wave propagation in simple crustal models. Finite Difference simulations were also performed to examine the problem of scattering in a layered halfspace assuming incident teleseismic P plane waves. Teleseismic data at NORESS were examined to infer the nature of scattering in the lithosphere under NORESS.

Technical Results

Section 1 describes the results of careful examination of regional phases in the NORESS data set. Array techniques were used to decompose the seismogram into constituent phases for analysis in the time domain. Gross designation of regional phases are commonly used in routine seismic analysis. Phases such as Pg and Lg are picked from the data using rough estimates of phase velocity and arrival time and are then incorporated into location algorithms. Our study showed that the crust in Fennoscandia generates a suite of clear, understandable arrivals which are poorly described by previous simple labels. These P, S, and Rayleigh wave arrivals contain important information on phase velocity and timing which can be used for more accurate event distance estimates. Indeed, we found that standard procedures used to generate the NORESS catalog often misidentified S and P phases resulting in mislocations of 80 km or more. We also found that much of the wave propagation could be understood with fairly simple layered models. The effect of scattering due to heterogeneity, while important for some azimuths and ranges, was not overwhelming. Thus, future array observations may be able to take advantage of more accurate processing to identify phases in the regional wave form.

Sections 2, 3, and 4 contain results on the nature of velocity heterogeneity seen in the lithosphere near receivers from incident teleseismic P waves. This work grew out of studies performed under the previous contract on the nature of scattering which produces teleseismic P wave coda. In Section 2, an observational study was performed to examine two assumptions in the energy flux model of coda generation developed in past work. Data from the Berkeley broad-band network were analyzed to determine if coda levels and decays are constant over a large region. This would substantiate the assumption of homogeneity of coda energy distribution behind the incident wavefront, important in developing the energy flux theory. We found that this was indeed true. However, we found that assuming that the direct wave is little affected by heterogeneity is not very good. Near-receiver effects serve to focus and defocus the direct wave invalidating the normalization required by the theory to infer the scattering Q parameter. We also found that teleseismic P wave coda can contain a significant portion due to scattering near the source.

Section 3 describes an extensive theoretical study of teleseismic P wave coda using 2D finite difference techniques to solve the acoustic and elastic wave equation. A scattering layer over an isotropic, non-scattering halfspace was assumed. We were interested in determining which factors were most important in controlling coda decay and level. Langston(1989) asserted that the distribution of scatterers in a layer could be very important for both the level and decay of coda. The simulations showed a surprising result that isotropic scattering produced the same coda decay for wide variations in layer thickness and amplitude of the velocity perturbations. The rate of coda decay was most sensitive to the anisotropy of the scatterers. Models which were plane-layered-like produced the highest decay rates. Decay rates were slowest for the isotropic scatterers. This presents the important possibility that reconnaissance of the gross geometry of scatterers in the lithosphere may be possible by examining coda decay rates and the directionality of the scattered coda field.

This was attempted using teleseismic P waves recorded by NORESS and is described in Section 4. It was found that teleseismic coda waves from deep events are generally dominated by propagation in near-vertical directions,

implying that local scattering is probably dominated by plane-layered-like structure. However, a discrete and significant P to Rg scattering event was found in the data and was associated with the Lake Mjosa topographic feature near the NORESS array.

Important Findings and Conclusions

Wave propagation in Fennoscandia is generally understandable in terms of simple plane layered structure models. Although the data show deviations from such models in terms of effects of layer dip, discrete phases are generated by these crust and mantle structures and are not significantly degraded by heterogeneity. Phase attributes, such as time and phase velocity, can be used to accurately identify arrivals. It was found that S waves are often misidentified at NORESS resulting in poor event locations.

The nature of lithospheric heterogeneity which produces P wave coda may be amenable to analysis since it was found that scatterer anisotropy appeared to be the strongest effect in controlling coda decay rate in the wave propagation simulations. The NORESS data suggest that scattering in the vicinity of the array is caused by highly anisotropic scatterers (plane-layered-like) with the exception of a discrete scattering events caused by P-to-Rg scattering off of topographic features.

Significant Hardware Development

N/A

Special Comments

N/A

Implications for Further Research

The careful analysis of a commonly available NORESS data set points out that there is still much to learned about the propagation of regional phases through direct observation. Other arrays of the area are currently being

studied in a companion project to broaden our experience with the generation of high-frequency regional phases. A challenge will be to implement these results into fast, array algorithms to refined location estimates.

Analysis of Regional Events Recorded at NORESS

Kristin S. Vogfjord and Charles A. Langston

February 23, 1990

Department of Geosciences

The Pennsylvania State University

University Park, Pennsylvania 16802

Abstract

Events recorded by NORESS are analyzed to determine the velocities and times of coherent crustal phases to be used in accurate locations and determination of crustal structure. The events straddle two azimuthal directions, and range in distance from 50 to 300 km, thus sampling two cross-sections of the crust and upper mantle; one in the Caledonides to the north west of NORESS, and the other to the south along the eastern rim of the Oslo Graben. F-k analysis is used to search for coherent phases in the data. All vertical channels are slant-stacked using the phase velocities and azimuths obtained in the windows containing coherent arrivals. A composite seismogram is then made for each event by piecing together slant-stacked sections representing all the detectable phases. Coherent phases are greatly enhanced by the procedure, and on closer inspection it is possible to improve some

of the locations from the NORESS bulletin. This causes a number of events to group together to the same location. PmP and SmS are the largest arrivals on all records from distances greater than 80 km. Closer in, the largest arrivals are P and S waves turning or reflecting in the upper crust. Rg waves are also prominent in records from that distance range. Pn is detected at distances around 200 km and further and has a very high phase velocity in the Caledonian record section, between 9 and 10 km/s. Sn can also be found in some events. Double crustal reverberations of P and S are observed at distances greater than 200 km. Travel time curves are constructed from plane layered homogeneous models to match travel times and phase velocities in the composite seismograms.

Introduction

Studies of wave propagation from regional seismic events and seismic refraction lines have generally been hampered by low signal-to-noise ratio and by poor phase identification. With the use of high-frequency, small-aperture seismic arrays, such studies can be greatly improved. Array analysis not only enhances the s/n ratio to bring out more details in the seismograms, but also allows the association of phase velocities and backazimuths with the arrivals. At regional distances, the prominent phases in the seismograms are the Pg and Lg wave trains, which are made up of a sequence of multiply reflected postcritical P and S waves trapped in the crustal waveguide. The main reflectors are the free surface and the Moho, but internal discontinuities in the crust also act to increase the complexity of the wave trains. The number of multiples increases with source distance as the critical distance for each multiple reflection is reached (Bouchon, 1982). The relative arrival times and amplitudes of the phases in the wave trains are sensitive to crustal

structure and source depth. They are therefore ideally suited for studying crustal structure and source effects in regional events.

The present study uses regional events recorded by the NORESS array, which was designed to enhance the detection of such events (Mykkeltveit et al., 1983), to study structure and its effects on wave propagation at regional distances. The array is located in the Baltic Shield, northeast of the Oslo Graben, which was formed by a continental rifting episode during the Permian. Volcanics and intrusions are prevalent in the Graben area, and results from previous seismic and gravity studies indicate undulations of several kilometers in the Moho under the Oslo Graben (Ramberg, 1976; Wessel and Husebye, 1987; Kanestrom and Haugland, 1971).

The events were chosen from the NORESS bulletin based on location and local magnitude to allow sampling of the crust on two different profiles extending from the array. The location of events, which range in magnitude from 1.7 to 3.8, is shown in Figure 1. The NW-SE crustal profile, delineated by the event distribution extends into the Caledonian mountain range, while the N-S profile, runs along the eastern rim of the Oslo Graben. The events are subject to f-k analysis to search for coherent arrivals; these are then used to infer crustal structure and to improve event locations, where necessary. The seismograms are compared with travel time curves calculated for two different crustal models obtained from previous refraction studies in the region (Sellevoll and Warrick, 1971; Kanestrom and Haugland, 1971).

Data Analysis

In order to find coherent phases in the data and to identify their phase velocities, f-k analysis is performed in sliding time windows on the 25 vertical components of the array. Window lengths and their locations in time are chosen after

inspection of the record sections, so that the window will contain the entire phase, which is at the center of the window. The data are then multiplied by a Hanning smoothing function and Fourier transformed in time to find the spectral peaks within the window. Two-dimensional Fourier transform on the space dimensions is then calculated at the peak frequencies to obtain the power spectrum in the wavenumber plane. If the window contains a coherent arrival, then there will be a distinct maximum peak of power somewhere in the wavenumber plane. The location of the peak determines the phase velocity and the direction from which the wave is coming. Phase velocities and backazimuths obtained for the various frequency peaks within a window often show some variation. This can be due to interference between phases with different travel paths, caused by layering or heterogeneities in the crust. Lack of resolution can also be the cause if phase velocities are high. In this situation the phase velocity and backazimuth of the frequency with the greatest power is chosen to represent the arrival. When there is variation in backazimuth between the main P and S phases within one event, the backazimuth of the largest phase is chosen to represent the event.

With the backazimuth and phase velocities for all detectable phases of an event in hand, the vertical channels are slant stacked and corrected to zero level. Time sections from the different slant stacks are then pieced together to form one composite seismogram as shown in Figure 2. The composite has a greatly improved signal-to-noise ratio so that the major crustal phases clearly stand out and some of the more obscure ones, such as Pn, become apparent. In some of the more distant events with small magnitudes, the signal-to-noise ratio is only 2 - 5. In such cases, the f-k analysis is performed on the raw data, but the channels are high-pass filtered with a 3-pole, zero-phase Butterworth filter before slant stacking to eliminate the

low-frequency noise.

When the channels are slant-stacked, coherent arrivals with the preferred backazimuth and incidence angle are enhanced, while the incoherent amplitude, and coherent amplitude arriving with a different backazimuth and incidence angle, are diminished. If a substantial variation in backazimuth and phase velocity occurs within an arrival the event will appear to have low coherency. For a quantitative estimate of the coherency in each event, and in order to compare the effects of different travel paths, the envelopes of all vertical channels are slant-stacked and time sections pieced together in the same manner as the seismograms; this composite envelope approximates the true total amplitude. The envelope of the composite seismogram, which approximates the true coherent amplitude is then subtracted to obtain the incoherent amplitude.

Event Locations

After slant stacking the events presented in Figure 1, it became apparent that several were mislocated, some by as much as 80 km. The composite seismograms for the events in question are presented in Figures 3, 4 and 5, where the arrows indicate the time picks of coherent arrivals from the NORESS bulletin. Some of the events were recorded during a period of unknown time drift of < 2 sec, occurring in the on-line data. This time drift is indicated in the figures by the time bars. The two thicker arrows in each event indicate the arrivals of the P and Lg waves, which were used to locate the event.

There are two main reasons for the mislocations. The first main reason involves the picking of the largest S wave arrival on the record as the arrival of the Lg wave. The two events in Figure 2 have two main S arrivals: Sg, which is used

here to represent an S wave that turns or reflects in the crust, with a phase velocity of 3.7 km/s, and the longer period Rg surface wave, with a velocity of 3 km/s. A schematic plot explaining the travel paths of the various phases is shown in Figure 6. By picking the larger amplitude Rg wave as the onset of Lg in event 88316, the source distance is overestimated by 40 km. Figure 3 shows the same misinterpretation of the onset of Lg for four nearly identical events, with three major S wave arrivals: Sg, the Moho reflected SmS, and Rg. Depending on which phase is picked as the Lg arrival, the events are misplaced from the actual distance of about 85 km, by as much as 80 km.

The second main reason for mislocation is demonstrated in Figure 5, which shows four events with the same relative arrival times but located over a 70 km distance range. The two closer events, 882205 and 88286, have local magnitudes of 2.3 and 2.2, whereas the other two, 88257 and 87294 have local magnitudes 2.6 and 2.8. Lg is picked at about the same time in all events, at the arrival of SmS. Pn is picked as the first P arrival in the two more distant events, but due to its smaller amplitude it is missed in events 88286 and 88205; 2xPmP is picked for event 88205 and the time pick for 88286 is late in the PmP phase. Thus small distant events tend to be mislocated closer than they actually are when the first arriving P phases are not detected. The actual distance for the four events is about 240 km, depending on velocity model. The mislocated events show a distribution in backazimuth, of up to 6 degrees, indicating some errors in backazimuth also.

Figure 1 shows three events with local magnitudes above 3. These are erroneous magnitudes, and when recalculated according to Bath (1976) they decreased to between 1.1 and 1.8. NORESS magnitudes were used for all the other events. The events are replotted in Figure 7 in their relocated positions.

Record Sections

NW-SE Section

The NW-SE record section has five events, which range in distance and backazimuth from about 50 to 300 km, and 293 to 314 degrees, respectively. Two events, 87183 and 85313, have been high-pass filtered for clearer phase identification. The record section is shown in Figures 8 and 9. Pg is the first arrival in the two closest events, but PmP takes over before the source distance of the third event is reached. Event 88244, which is the closest at about 50 km distance, has well-defined Pg and Sg phases and a large Rg phase, but no mantle reflection is apparent. Event 88133, on the other hand, is close to the critical distance for mantle reflection and therefore has large PmP and SmS arrivals following Pg and Sg. The Rg phase is also still prominent.

Pn is the first arrival on the remaining events with a phase velocity of about 10 km/s. Sn is also found in the two farthest events with a phase velocity of about 5.2 km/s. A large PmP phase follows Pn in all three events, with a phase velocity of about 7.2 km/s, and 2xPmP with a phase velocity of around 8 km/s starts building up from a distance of 200 km and further. The corresponding SmS and 2xSmS are also clearly observed, in fact 2xSmS is detected in event 87183, when 2xPmP is not.

Arrival times in the events were fitted to travel time curves calculated for the P and S phases reflected off the interfaces of the two crustal models given in Table I. They were obtained for the E-W trending Flora-Asnes profile by Sellevoll and Warrick (1971), and the N-S trending Profile 3-4 by Kanestrom and Haugland (1971). The locations of the profiles are shown in Figure 7. The fitting was done by adjusting source distances and origin times until an acceptable match in travel

time was obtained. Travel time curves for the Flora-Asnes profile and for Profile 3-4 are plotted with the record sections in Figures 8 and 9, respectively. Distance adjustments were within 10 km for all events except 85313, which moved from a distance of 251 km to 287 km, for the Flora-Asnes profile, and 305 km for Profile 3-4. An acceptable fit was obtained for both models, but the slopes of the travel time curves for Profile 3-4 better match the observed phase velocities of the seismograms; the slopes on the PmP and SmS curves approach the limits 7.2 km/s and 4.1 km/s, respectively. Slopes on 2xPmP and 2xSmS, however, are somewhat lower than the observed phase velocities. Slopes on the Flora-Asnes travel time curves are generally lower than the observed phase velocities. Travel time curves for P-to-S-converted phases are also included in Figure 8. However, they do not correlate with any detectable arrivals in the composite seismograms indicating that the discontinuities are more gradual than in the model.

N-S Section

This record section has four events, which after relocation, range in distance and azimuth from 73 to 170 km and 157 to 202 degrees, respectively; the two farthest events have been high-pass filtered before stacking (see Fig. 10). All events have a clear Pg arrival, with a phase velocity of approximately 6.2 km/s, but a less prominent Sg. PmP is very faint in the two closest events (around 80 km), which is near the critical distance, but becomes clearer with increasing distance. Pg is the first arrival in all events, but PmP has started to interfere with it in event 88075, at 170 km distance, so the crossover from a Pg to a PmP first arrival must occur just after that distance. SmS is the largest arrival in all but one event; Event 88237 has an Rg wave of larger amplitude arriving just before SmS. A relatively smaller Rg wave arrives before SmS in event 88099. Neither Pn nor Sn are found in event

88154. Event 88075, on the other hand, has a faint high-frequency arrival, which can be identified with Pn. With a phase velocity around 9 km/s, it arrives 0.6 seconds before PmP.

Arrival times for this record section were also fitted to travel time curves for the two crustal models. Both models can match the observed arrival times in the records, except for the Moho reflections in event 88099, which require a 34-km-thick crust. The slopes of the travel time curves for the slower Flora-Asnes model, however, better match the observed phase velocities. The travel time curves for that model are overlaid on the record section in Figure 10 The crossover from a Pg to a PmP first arrival occurs at 200 km distance, which is in agreement with the phase velocities obtained for event 88075, whereas the crossover occurs too early in the Profile 3-4 model. P-to-S-conversions are not detected.

The effects of heterogeneous structure on the wave propagation along the eastern rim of the Graben are frequency dependent: Waves with frequencies less than about 10 Hz do not appear to be affected by irregular structure, while higher frequencies tend to have a broad power maximum in the wavenumber plane, with the peak stretched toward the Graben. Because of differences in frequency content, the four events are affected to a varying degree. The average frequency spectra of the events are shown in Figure 11. Due to the low signal-to-noise ratio in events 88154 and 88075 (approx. 4 and 2, respectively) their spectra peak below 1 Hz. Above that peak most of their energy is carried with 4.-5. Hz and 6.-8. Hz waves, respectively. Most of the energy of event 88099 is concentrated between 5 and 10 Hz; event 88237, apart from the 1.1 and 1.6 Hz Rg waves, has most of its energy carried at frequencies between 8 and 14 Hz. Due to their deficiencies in high frequencies, events 88099, 88154, and 88075 are not affected by heterogeneous

structure. However, event 88154, due to its closeness to the Graben area may exhibit reflections from within the Graben; the two small phases detected between the P and the S phases have backazimuths of 213, whereas all other phases have backazimuths around 200. Event 88237, due to its high frequencies, is greatly affected by irregular crustal structure. Its location, however, is farthest from the Graben. P waves with peak frequencies above 10 Hz generally have more than one power maximum in the wavenumber plane, at backazimuths around 130, 155, and 170, whereas lower frequency P and S waves have only one at backazimuths between 155 and 160. When relocating the event, a backazimuth of 157 was chosen.

Discussion

The relatively simple structure of the Baltic Shield is the dominant cause for the clear separation and sharpness of the observed crustal arrivals in the events of both record sections and accounts for the successful modeling of the arrivals with homogeneous plane layered models. A comparison of the two, however, reveals some differences in crustal structure: The NW-SE trending profile that reaches into the Caledonian mountains appears to have higher crustal velocities than the N-S profile that runs along the eastern edge of the Oslo Graben. Reflections off the Moho are sharper near the critical distance and have higher phase velocities in the Caledonides than do those east of the Graben, indicating higher average velocities in the crust and a sharper velocity contrast at the crust mantle interface. Average crustal thickness appears to be similar for both profiles, approximately 37 km, but near the Graben the crust thins to about 34 km. This is in agreement with previous studies, which have shown thinning of the crust, by several kilometers in the Graben area (Kanestrom, 1973, Kanestrom and Haugland, 1971, Cassel et al., 1983).

The high phase velocities obtained for Pn also indicate a dip in the Moho near the array of approximately 10 degrees, depending on velocity model. High Pn velocities under the NORSAR array have also been reported previously by Kanestrom and Haugland (1971) and Kanestrom (1973). Indeed, velocities in a NNW direction were found to be 10 km/s.

Another noticeable difference between the two profiles is the scattering of waves with frequencies above 10 Hz in the N-S profile. This scattering is not observed in the NE-SW profile. To illustrate this point, Figure 12a shows the double power peak in the wavenumber plane, observed in the Pg phase of event 88237 for the peak frequency of 10.8 Hz. A secondary frequency peak in the same time window, but of lower power is at 4.8 Hz. This lower frequency has no sign of scattering, as shown in Figure 12b. For a comparison with the Caledonian profile, Figure 12c shows the power spectrum for the peak frequency in the Pg window of event 88267. Its amplitude in this event is about twice the amplitude in event 88237. At a frequency of 13.7 Hz, there is much less scattering and no apparent multipathing as in the southern profile.

For a comparison of the coherency in the events, Figure 13 shows plots of the envelope stacks (dashed lines), which estimate the total amplitude in each event, and the incoherent amplitude (solid lines) for four of the events. The difference between the two represents the coherent amplitude. Between the major phase arrivals, the incoherent amplitude is about 70 percent of the total amplitude, but at the arrivals of the large crustal phases, it drops down to about 20 percent for the P phases, somewhat higher for the S phases. The incoherency is also higher for the most distant event, 88286, indicating more scattering due to the longer travel path. Event 88237, which showed evidence of multipathing has high incoherency

throughout all the crustal reflections due to scattering in the high-frequency range, and to the stacking, which favored the 157 degree backazimuth. The only phase with high coherency in that event is the low-frequency Rg wave at about 20 sec. on the plot. Event 88159 also has high coherency during the arrival of Rg. Therefore, as expected, incoherency increases with source distance and frequency, and combining slant-stacks to approximate a seismogram is a permitted procedure, since incoherency during the arrivals of the major phases is low.

Although plane layered constant velocity models can account for all major arrivals in the seismograms, data from events at a distances < 50 km require velocity gradients near the surface. This is in accordance with the refraction study of Mykkeltveit (1980) of a profile north of the Caledonian cross section presented here. A future improvement of the structure model will include this effect.

The events presented here clearly show that the Pg and Lg wave trains on regional seismograms have separate arrivals within them with distinctive phase velocities, which constrain their travel path, and at the same time the crustal structure. These phases can be valuable in modeling structure, as well as in event location and source depth determination. Describing these phases only in terms of Pg and Lg is therefore an oversimplification and leaves valuable information contained in them unused.

Acknowledgements

References

Bath, M. (1976). Engineering analysis of ground motion in Sweden, Seismological Institute Report, Uppsala, Sweden, pp. 17-19, 44.

Bouchon, M. (1982). The complete synthesis of seismic crustal phases at regional distances, J. Geophys. Res., 87, 1735-1741.

Cassel, B. R., S. Mykkeltveit, R. Kanestrom and E. S. Husebye (1983). A North Sea-southern Norway seismic crustal profile, Geophys. J. R. astr. Soc., 72, 733-753.

Kanestrom, R. and K Haugland (1971). Profile section 3-4, in Deep Seismic Sounding in Northern Europe, pp. 76-91, ed Vogel, A., Swedish Natural Science Research Counsil, Stockholm.

Kanestrom, R. (1973). A crust mantle model for the NORSAR area, Pure appl. Geophys., 105, 729-740.

Mykkeltveit S. (1980). A seismic profile in southern Norway, Pure appl. Geophys., 118, 1310-1225.

Mykkeltveit, S., K. Astebol, D. J. Doombos, and E. S. Husebye (1983). Seismic array configuration optimization, Bull. Seism. Soc. Am., 73, 173-186.

Ramberg, I. (1976). Gravity interpretation of the Oslo Graben and Associated igneous rocks, Norg. geol. Unders.. No. 325.

Sellevoll, M. A. and R. E. Warrick (1971). Refraction study of the crustal structure in southern Norway, Bull. Seism. Soc. Am.. 61, 457-471.

Wessel, P. and E. S. Husebye (1987). The Oslo Graben gravity high and taphrogenesis, Tectonophysics. 142, 15-26.

TABLE I.

Flora-Asnes Crustal Model (Sellevoll and Warrick, 1971). *			
Vp (km sec^{-1})	Vs (km sec^{-1})	Density (g cm^{-3})	Thickness (km)
5.20	3.00	2.60	1
6.00	3.46	2.80	14
6.51	3.76	3.00	22
8.05	4.65	3.30	Half-space

Profile 3-4 Crustal Model (Kanestrom and Haugland, 1971). *			
Vp (km sec^{-1})	Vs (km sec^{-1})	Density (g cm^{-3})	Thickness (km)
5.20	3.00	2.60	1 **
6.20	3.58	^ °8	16
6.55	3.78	2.98	10
7.20	4.16	3.13	10
8.20	4.73	3.35	Half-space

* S wave velocities are calculated assuming a Poissons solid.

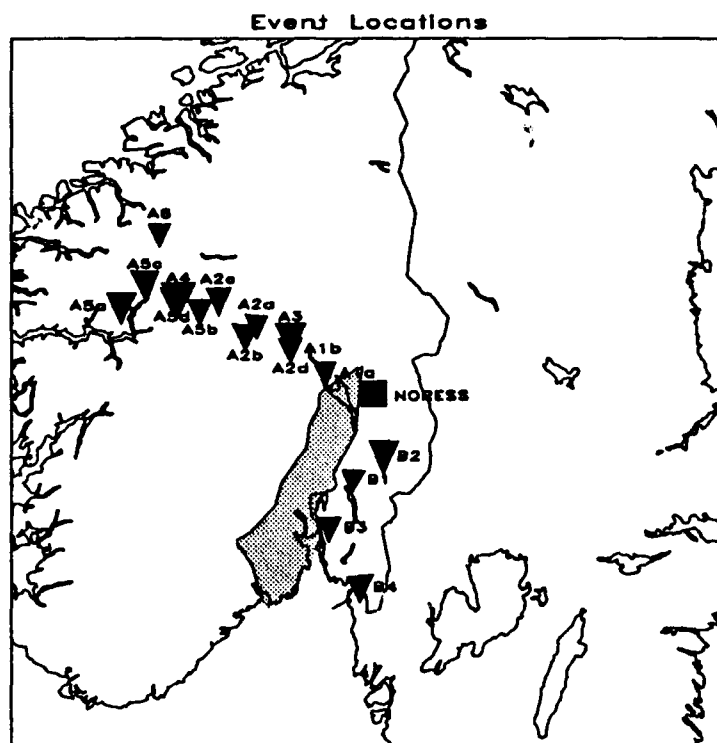** Surface layer added to the model.

Figure 1: Map showing event locations (triangles) and location of NORESS (square). Shaded area represents the Oslo Graben.
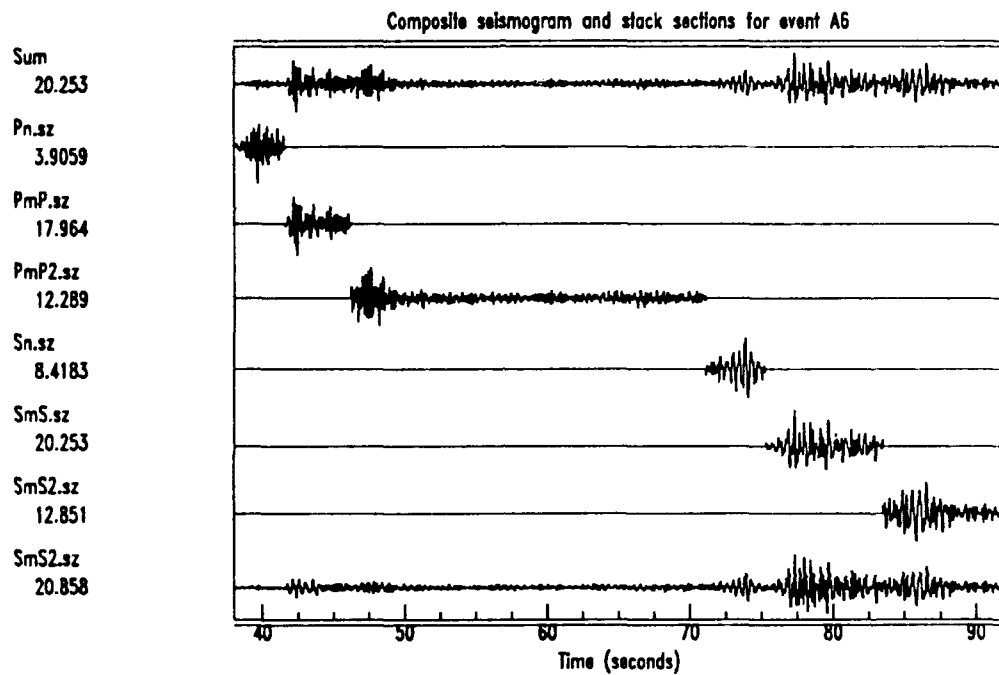
Figure 2: Composite seismogram for event A-6 and time sections from the array
beams used to make up the composite. Bottom trace shows the whole
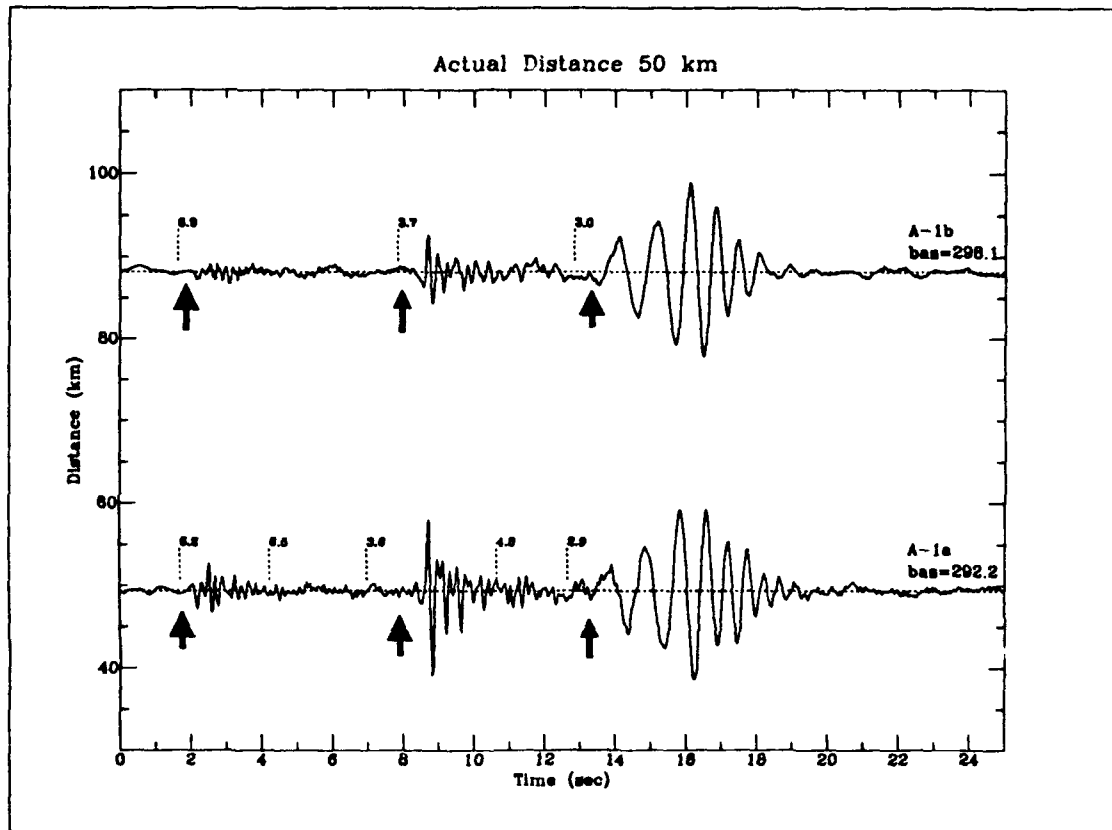2xSmS beam.

Figure 3: Composite seismograms for events A-1a and A-1b plotted at the source distance determined by NORESS. The traces are normalized to their maximum amplitude. The stacking windows are indicated by dashed lines, and the stacking velocities are shown on the left margin of each window. Arrows indicate arrival times of phases as listed in the NORESS bulletin. The thick arrows represent the phases picked by NORESS as P and Lg and are used in the automatic location.
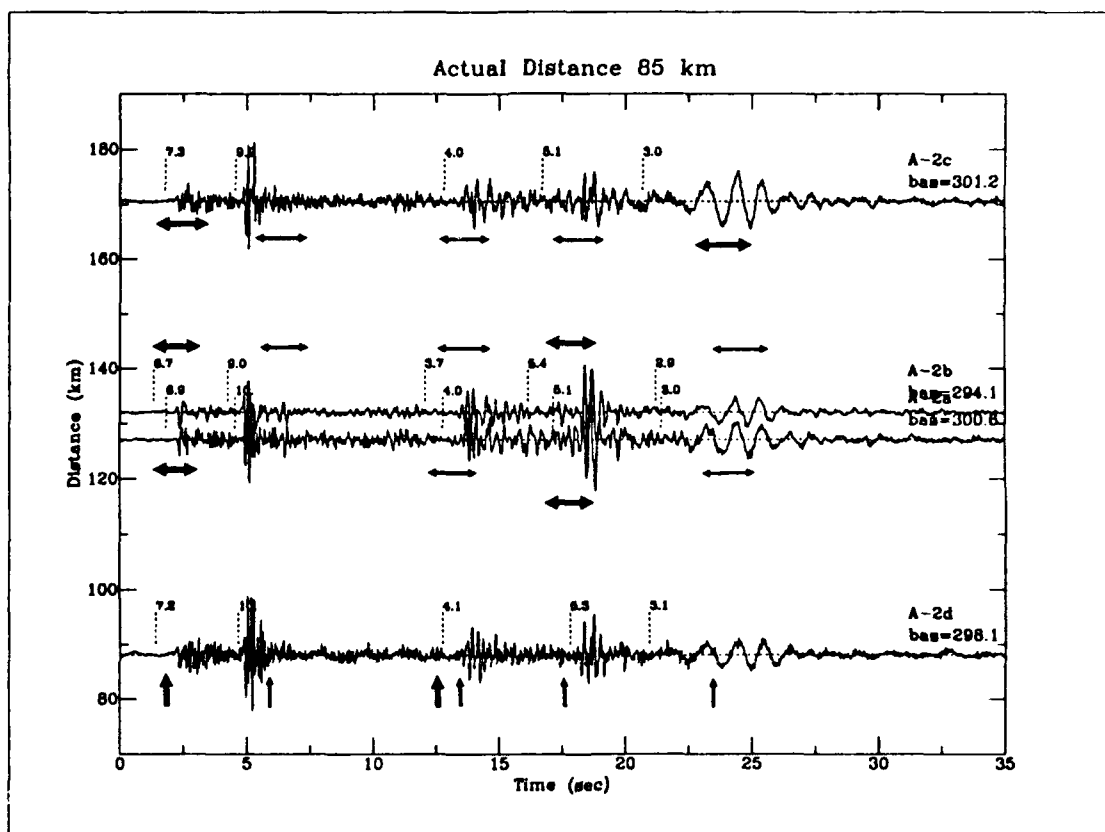
Figure 4: Composite seismograms for events A-2a, A-2b, A-2c and A-2d plotted at their source distance from NORESS. Same scheme as Figure 3, except for arrival times in events A-2a, A-2b and A-2c, which were recorded during a period of unknown time drift of < 2 sec, occurring in the on-line data. The arrow bars indicate the uncertainty in the arrival times and the thick bars represent NORESS automatic time picks.
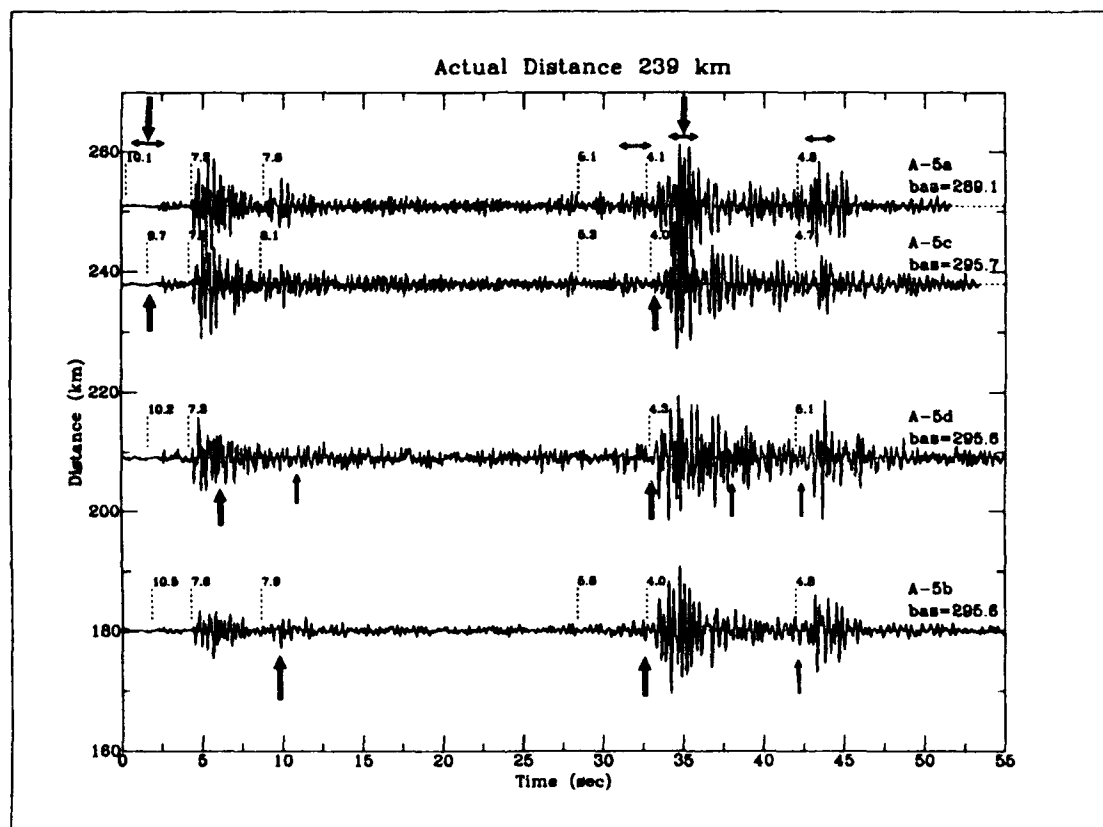
Figure 5: Composite seismograms for events A-5a, A-5b, A-5c and A-5d. Same scheme as Figures 3 and 4.
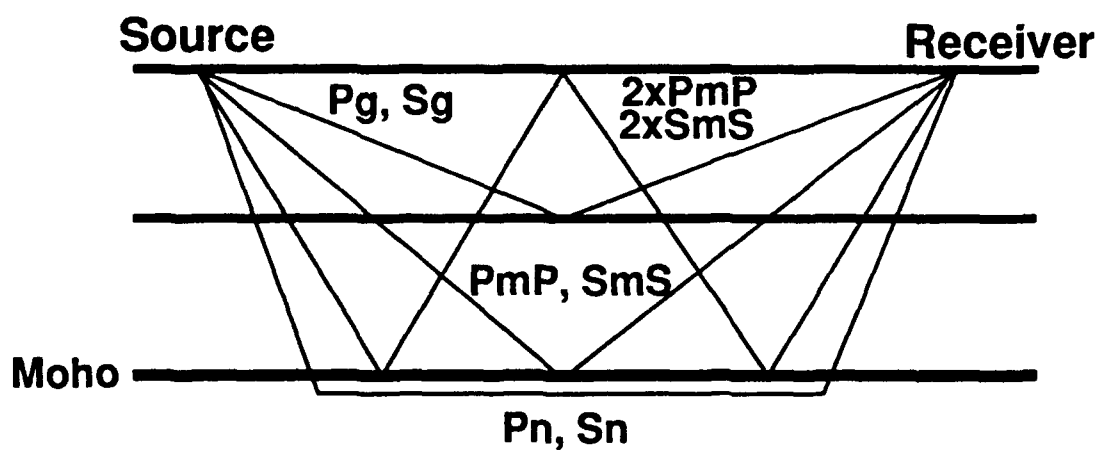
Figure 6: A schematic explaining the notation and travel paths of the major crustal and upper mantle phases. P waves converted to S waves at the crustal and mantle interfaces will be denoted by Pg-S and PmS, respectively.

Figure 7: Map showing relocated events (solid triangles) and location of NORESS (solid square). Hatched area represents the Oslo Graben. The NW-SE line represents the Flora-Asnes refraction line, and the N-S line represents the Profile 3-4 refraction line.
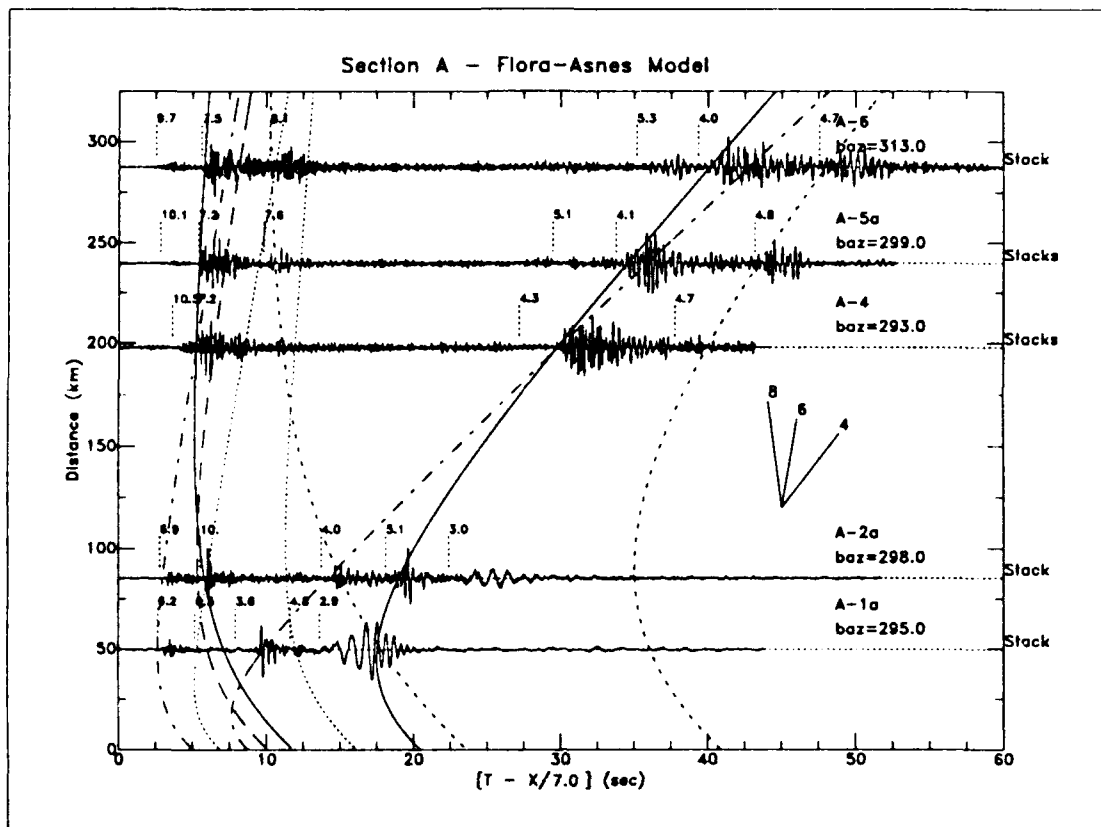
Figure 8: Composite seismograms for the events from the Caledonian section
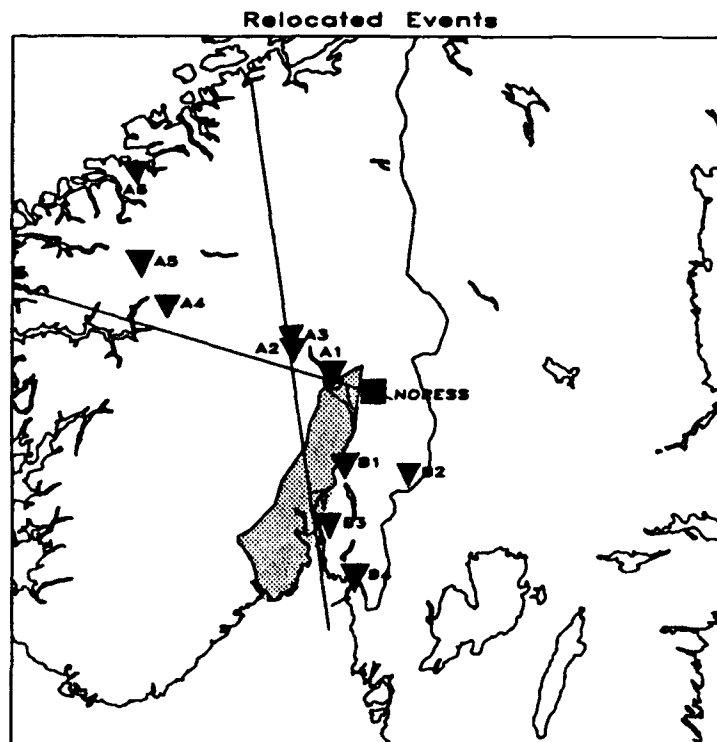plotted as a function of distance, reduced with a velocity of 7 km/s
and normalized to maximum amplitude. Dashed lines above seismograms
indicate where the slant-stack sections have been pieced together.
Stacking velocity is shown on the left margin of each interval.
Travel time curves for the Flora-Asnes model are overlaid on the
plot. They represent: (———) PmP and SmS; (—·—) Pg and Sg;
(···) Pg-S and PmS; (—–) 2xPmP and 2xSmS; (——) 2xPg. Slopes
representing velocities on the curves can be read from the velocity
template to the right of center on the plot.

-23-

Figure 9: Same record section as in Figure 8, but with the travel time curves
for the Profile 3-4 model overlaid. Reflections off the two inter-
faces in the crust are referred to as Pg1 and Pg2, respectively.
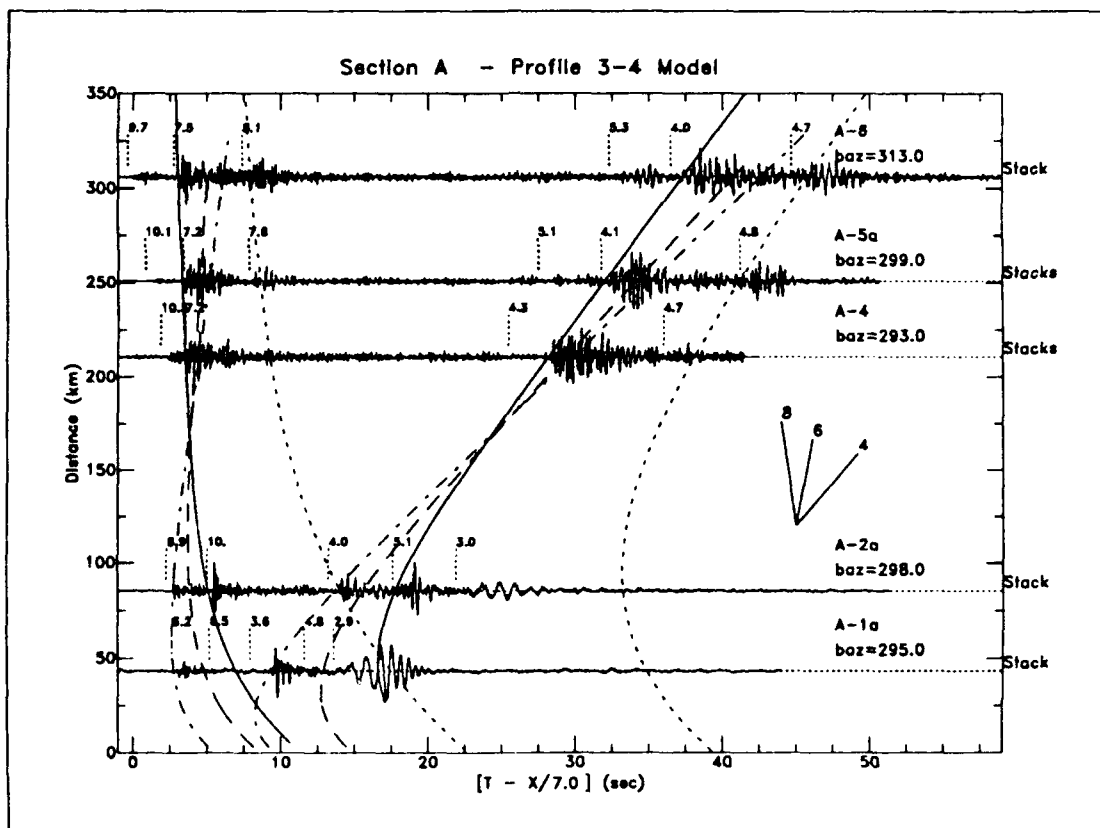A similar notation is used for S-waves. Travel time curves
represent: (←·→) Pg1 and Sg1; (←—→) Pg2 and Sg2. Same notation for
Moho reflections as in Figure 8.

Acknowledgements

*Formerly Geophysics Laboratory

References

Ammon, C.J. (1985). Time domain teleseismic P waveform modeling and the crust and upper mantle structure beneath Berkeley, California, M.A. Thesis, SUNY Binghamton.

Aki, K., and B. Chouet (1975). Origin of coda waves: Source, attenuation, and scattering effects, J. Geophy. Res., 80, 3322-3342.

Blakeslee, S.N., and P.E. Malin (1990). A comparison of earthquake coda waves at surface versus subsurface seismometers, J. Geophys. Res., 95, 309-326.

Bolt, B.A., J.E. Friday, and R.A. Uhrhammer (1988). A PC-based broadband digital seismograph network, Geophysical Journal, 93, 565-573.

Bungum, H., E.S. Husebye and F. Ringdal (1971). The NORSAR array and preliminary results of data analysis, Geophys. J. R. astr. Soc., 25, 115-126.

Collins, E.R., and R.A. Uhrhammer (1988). Bulletin of the Seismographic Stations of the University of California, vol 57, Nos.1 and 2, University of California, Berkeley.

Dainty, A.M. and D.B. Harris (1989). Phase velocity estimation of diffusely scattered waves, Bull. Seism. Soc. Am., 79, 1231-1250.

Dainty, A.M., M.N. Toksoz, K.R. Anderson, P.J. Pines, Y. Nakamura, and G. Latham (1974). Seismic scattering and shallow structure of the Moon in Oceanus Procellarum, Moon, 9, 11-29.

Frankel, A. and L. Wennerberg (1987). Energy-flux model of seismic coda: separation of scattering and intrinsic attenuation, Bull. Seism. Soc. Am., 77, 1223-1251.

Herraiz, M., and A.F. Espinosa (1987). Coda waves: a review, PAGEOPH, 125, 499-577.

Korn, M. (1990). A modified energy flux model for lithospheric scattering of teleseismic body waves, Geophys. J. Int., 102, 165-175.

Langston, C.A. (1979). Structure under Mount Rainier, Washington, inferred from teleseismic body waves, J. Geophys. Res, 84, 4749-4762.

Langston, C.A. (1989a). Scattering of teleseismic body waves under Pasadena, California, J. Geophy. Res., 94, 1935-1951.

Langston, C.A. (1989b). Scattering of long-period Rayleigh waves in western North America and the interpretation of coda Q measurements, Bull. Seism. Soc. Am., 79, 774-789.

McLauglin, K.L., L.M. Anderson, and Z.A. Der (1985). Investigation of scattering and attenuation of seismic waves using two-dimensional finite difference calculations, in Multiple Scattering of Waves in Random Media and Random Rough Surfaces, edited by V.V. Varadan and V.K. Varadan, pp. 795-822, Pennsylvania State University, University Park, PA.

Thurber, C.H. (1983). Earthquake locations and three-dimensional crustal structure in the Coyote Lake area, central California, J. Geophy. Res., 88, 8226-8236.
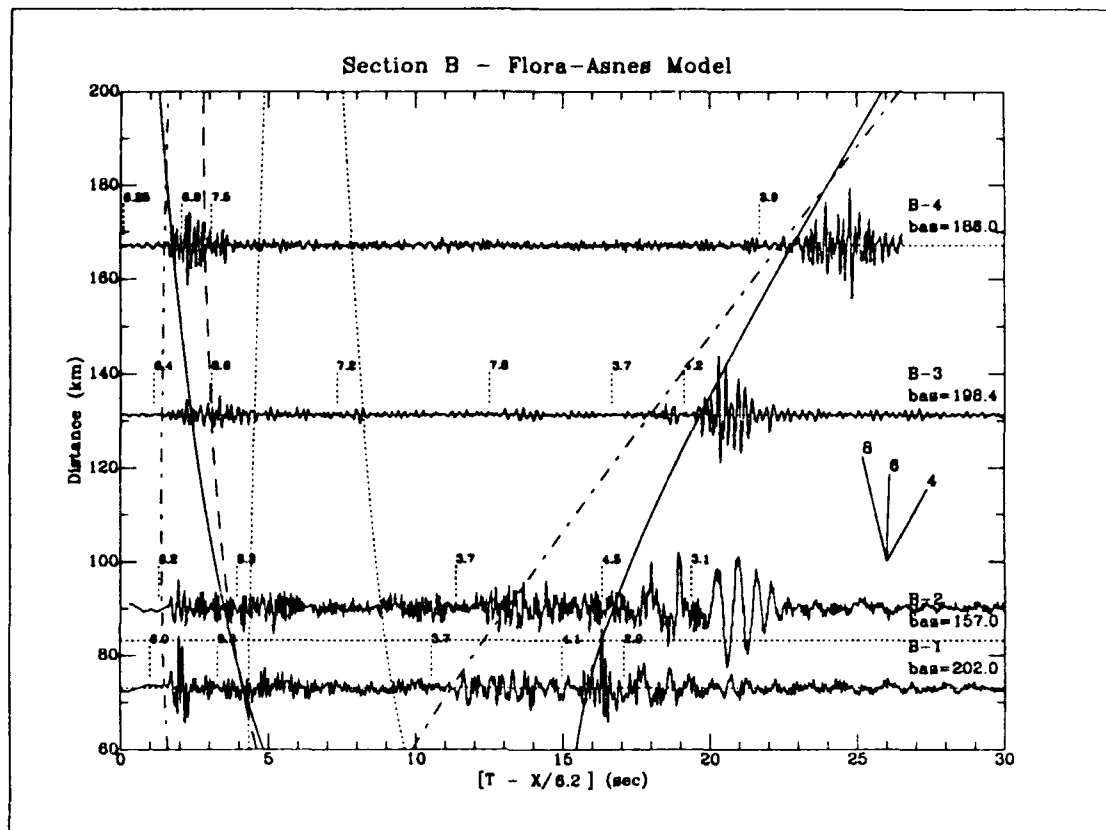
Figure 10: Composite seismogram record section from the N-S profile, with the travel time curves for the Flora-Asnes profile overlaid. Same scheme as in Figure 8 except travel time curves for the double Moho reflections, 2xPmP and 2xSmS are not shown.
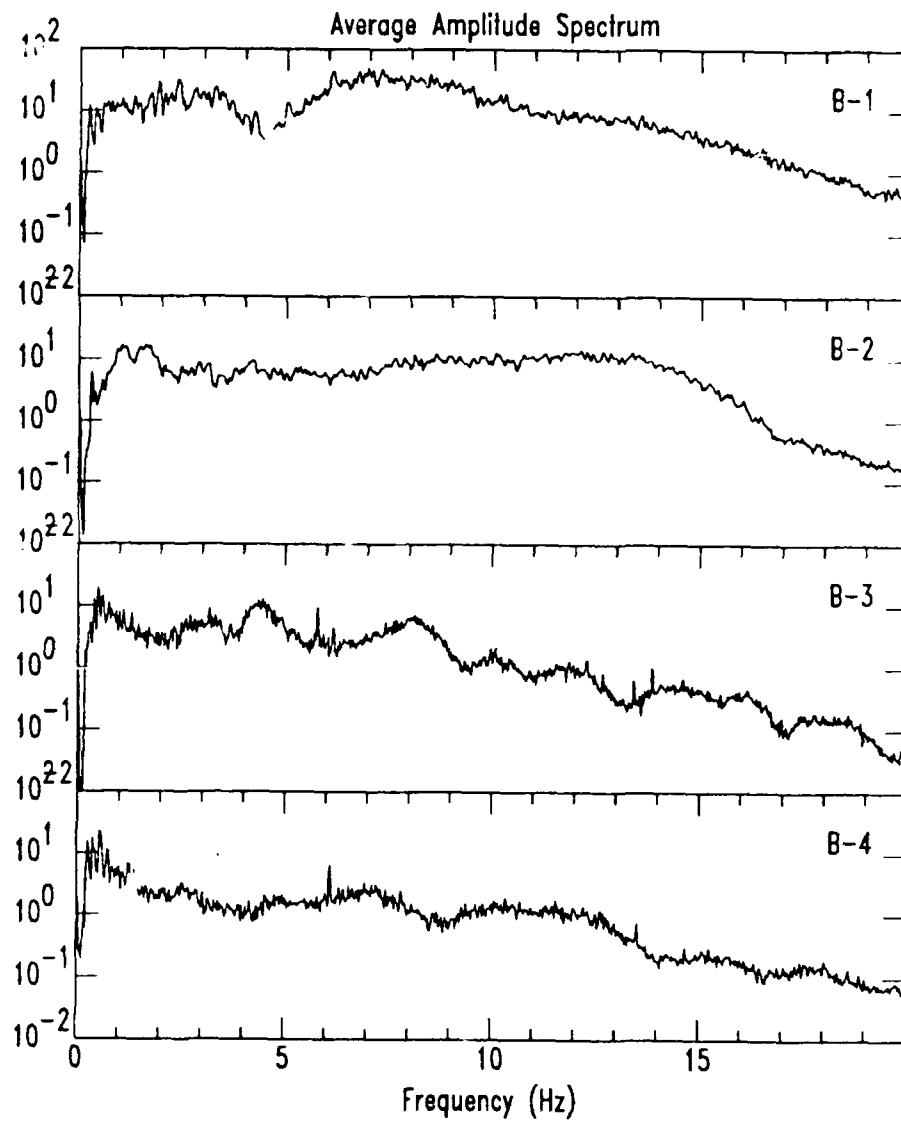
Figure 11: Average amplitude spectra of the records from the four events in the N-S record section, each calculated for a 30 sec time window containing the whole waveform.

NBFK - single window

Estimated bearing: 149.

Estimated velocity: 6.20

Analysis frequency: 10.80

Max. horiz. wavenumber: 2.5000

Scaling type: LINEAR

Max. power value: 0.65155e+07
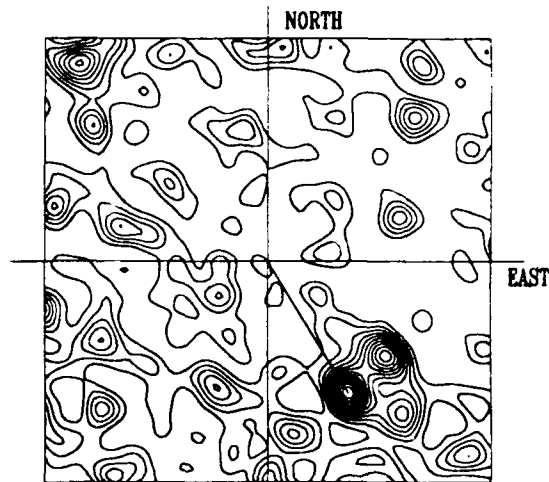
NBFK - single window

Estimated bearing: 155.

Estimated velocity: 6.41

Analysis frequency: 4.800

Max. horiz. wavenumber: 2.5000

Scaling type: LINEAR

Max. power value: 0.33054e+07
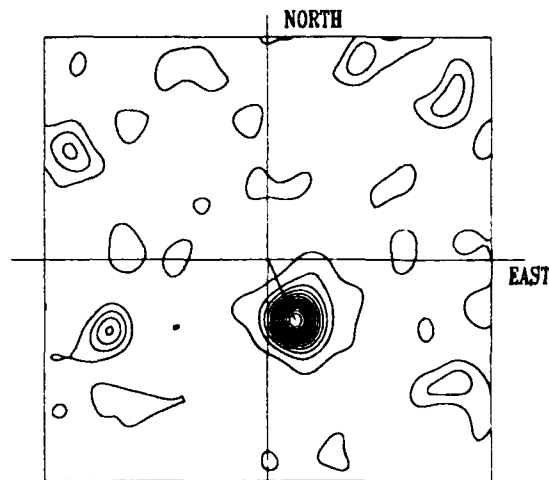
NBFK - single window

Estimated bearing: 303.

Estimated velocity: 7.24

Analysis frequency: 13.70

Max. horiz. wavenumber: 2.5000

Scaling type: LINEAR

Max. power value: 0.64869e+08
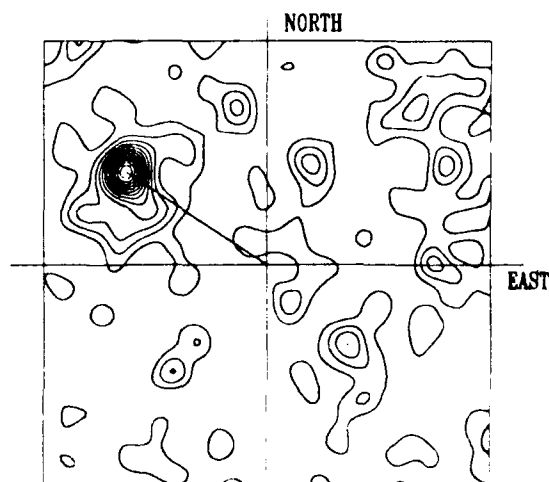
Figure 12: Power spectra at peak frequencies in Pg for events B-2 and A-2d.
a) Event B-2 at maximum peak frequency.
b) Event B-2 at secondary peak frequency.
c) Event A-2d at maximum peak frequency.
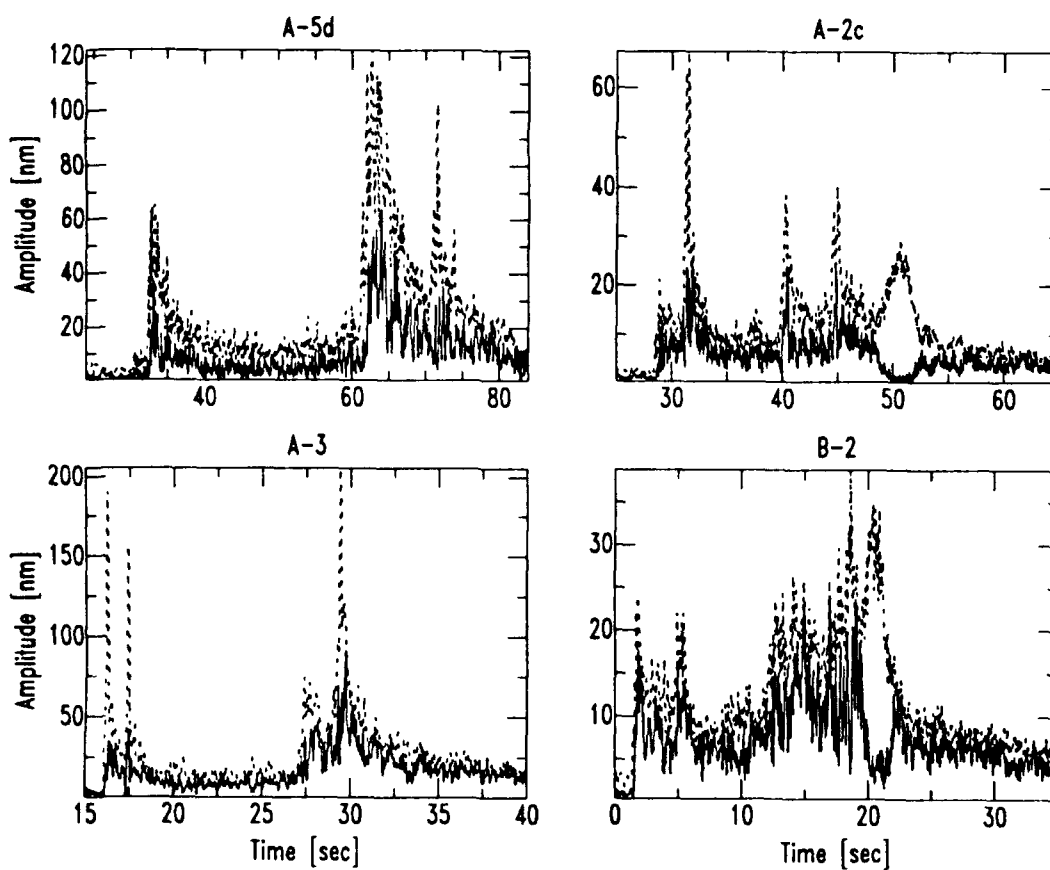
Figure 13: Estimated total amplitude (dashed) and incoherent amplitude (solid) for events A-5d, A-3, A-2c and B-2.

Scattering of Teleseismic Body Waves

Along the

Hayward-Calaveras Fault System

by

Charles A. Langston

and

Charles J. Ammon

June 5, 1990

Revised: October 12, 1990

Department of Geosciences

Pennsylvania State University

University Park, PA 16802

Abstract

Broad-band, digital, teleseismic P-wave data from the University of California, Berkeley, stations BKS, MHC, and SAO are used to study the character of teleseismic P coda. Velocity heterogeneity in structure near these stations gives rise to a variety of scattering effects which include azimuthly dependent receiver functions, large tangential component particle motions, and high levels of P coda. P codas for shallow and deep teleseisms are analyzed for three frequency bands centered at 1.5, 0.75, and 0.375 hz. Observed coda decay rate and level are fit with an energy flux theory to parameterize scattering effects near the source and at the receiver. Coda decay rate and level for deep earthquakes are seen to be stable observables between stations, implying that the scattered coda field is homogeneously distributed over the receiver network validating a major assumption in the energy flux model. Scattering Q, Q_s, is not particularly well constrained by the data and is inferred to be affected by focussing and defocussing effects of the direct P-waves. There is a pronounced difference in coda decay rate between shallow and deep earthquakes for 1.5 hz coda where coda decay rate for deep events is about a factor of two greater than for shallow events. There is no difference in coda decay rate between the two populations of events in the lower frequency bands. The observation at 1.5 hz is consistent with a simple model of P-wave coda formation where most coda forms in a scattering layer near the surface of the earth in regions near the source and near the receiver. The homogeneity of coda decay at 0.75 and 0.375 hz for deep and shallow events suggests that a large, near-receiver scattering mechanism, such as surface wave formation, dominates the coda.

Introduction

Scattering of teleseismic body waves in heterogeneous structure is a source of signal-induced noise for many broad-band wave form studies. Efforts to deterministically model the wave form rely on specific knowledge of earth structure that can be represented in reasonably simple plane layered or vertically inhomogeneous models. Most of the effort expended in detailed source mechanism studies lies in determining the tradeoffs between inferred source parameters and unknown, but bounded estimates of earth structure. Signal produced by waves scattered by lateral heterogeneity will naturally fold back into erroneous models of the source since the wave propagation will be assumed to be known through synthetic seismogram calculations for simple structure. The scattered signal may also be inadvertently modeled for simple plane layered earth structure in receiver studies, yielding misleading crustal or mantle structures.

A principal characteristic of scattering is the production of an extended coda after major arrivals. Many studies have been performed to study coda particularly for cases of local S wave propagation (see Herraiz and Espinosa, 1987, for a review). The obvious effect of scattering in teleseismic P-waves is to produce an extended coda with a characteristic exponential decay. The extended coda becomes an important contaminant if there are later arriving phases of interest such as small Ps conversions from crustal interfaces. However, the exponential decay implies that scattered waves will be largest at the P-wave arrival itself. Because these scattered waves arrive near Fermat's minimum time, they can also give rise to focussing or defocussing effects, depending on the specific structural geometry, which can severely distort the incident P wave front.

A previous study (Langston, 1989) examined scattering seen in teleseismic P wave receiver functions from deep events recorded at PAS (Pasadena, California) and SCP (State College, Pennsylvania). Scattering from heterogeneous structure at PAS was evident through observations of large, off-azimuth body wave conversions and high levels of coda over the three components of motion. Comparison of codas observed at PAS and SCP showed that high levels of coda correlate with slow coda decay rate. These observations were modeled using an energy flux model for scattered body waves in a heterogeneous layer over an isotropic halfspace. Simulations of body

wave propagation in random one-dimensional (1D) structure showed that observed codas were too large to be explained by plausible 1D structures. However, the 1D simulations did show that as the severity of scattering increased with heterogeneity, coda decay rate decreased as coda level, relative to the direct P wave, increased, in accord with the data. If interpreted with a single scattering model, the slower coda decay rate would imply a higher scattering Q or less scattering attenuation. The apparent paradox was resolved with the energy flux model where scattering Q, as usually defined, was decoupled from the process which controls coda decay. Coda decay rate is controlled by radiative diffusion of the coda field from the scattering layer into the isotropic halfspace.

Although the model allows a simple parameterization of teleseismic P coda, it primarily introduces some interesting issues in both the interpretation of coda and its mechanism of formation. Observed coda levels in the receiver function data are several times higher than expected from body wave scattering and suggest that body-to-surface wave conversion is important. Blakeslee and Malin (1990) studied small earthquakes at Parkfield, California, with a borehole array and saw that coda complexity increased near the surface. They suggested that body wave scattering dominated coda away from the free surface and that body wave-to-surface wave conversions dominated coda at the surface. This mechanism of coda production will be frequency dependent. Considering the reciprocal problem of a source in the scattering layer, it is also likely that near-source coda production follows similar mechanisms where surface wave-to-body wave interactions occur and may be source depth dependent (McLaughlin et al, 1985). An expectation of this simple view of coda formation is that shallow earthquakes, as seen teleseismically, should display higher levels of coda with slower decay rate than seen for deep earthquakes. Dainty et al (1974) suggested this kind of model as an explanation of lunar seismogram coda using an energy diffusion approach for scattering in the lunar regolith. Thus, it might be expected that the apparent coda Q for shallow events should generally be greater than that measured from deep events if scattering is confined by heterogeneity in the lithosphere.

A major assumption in the energy flux coda model, as presented by Frankel and Wennerberg (1987) for a wholespace and modified for a scattering layer over a homogeneous halfspace by Langston (1989a, 1989b) and Korn(1990), is that the scattered coda field arranges itself homogeneously behind the incident wave front. Frankel and Wennerberg (1987) developed the model by appealing to finite difference simulations of wave propagation in scattering media. Although they show that this assumption is very good in the simulations, empirical verification with the data is desirable. Aki and Chouet (1975) suggest in their study of local S wave codas that this is true since the apparent mean free path of scattered coda waves is large compared to the travel path of the direct S wave. A purpose of this study is to use data from a regional network to see if P coda displays similar characteristics of decay and level over the region, substantiating this assumption of coda homogeneity.

In this paper, we use data collected from the University of California Berkeley seismic network to examine coda from a suite of teleseismic events at several receivers. The data were collected as part of a receiver function study to determine gross crustal and upper mantle structure in Central California. This aspect of the study will be reported elsewhere. We wish to primarily investigate the stability of coda decay and level estimates by examining coda from the same events recorded at different receivers. The results will show that, like many coda determinations from local S waves, coda decay rate is a generally stable measure for individual events. However, coda decay rate also depends on source depth; being slower, in general, for shallow sources. This supports a simple model of scattering in the earth suggested by Dainty and Harris (1989) where scattering occurs primarily at the source and at the receiver with little scattering occurring along the mantle path of the seismic ray. The results will also show that inferring scattering Q from the relative coda level is generally unstable and is probably contaminated by direct wave focussing effects.

Berkeley Network Data

Ammon (1985) analyzed deep earthquake P-wave forms recorded on the analog system at BKS to recover the receiver function for structure under the station. He found that the radial component receiver functions varied substantially with azimuth and contained many large arrivals compared to direct P. Particle motions were also complex for later arrivals giving rise to tangential motions relative to the P-wave great circle path. An original purpose of the present study was to obtain high quality digital data from Berkeley's new broad-band digital system to examine these scattering effects in more detail and to extend structure studies to other receivers in the region. Figure 1 shows the location of BKS (Berkeley), MHC (Mount Hamilton) and SAO (San Andreas Observatory) stations which have broad-band, three component, digital instrumentation. Bolt et al (1988) and Collins and Uhrhammer (1988) describe the digital recording system and responses for these stations. Responses are flat to ground velocity between 0.05 and 5 hz. Earthquake events were chosen for study by examining the catalog of available waveforms at the Berkeley Seismic Station and choosing those with good signal to noise characteristics. Usually this meant finding teleseisms with body wave magnitude greater than 5.5. Table 1 contains event parameters and Table 2 the stations recording each event.

Figure 2 shows the three components of motion near the P-wave arrival for the 10/08/88 Tonga Islands event recorded at BKS. MHC and BKS have the same general receiver characteristics showing azimuthally varying radial receiver functions and a tangential component about 20% of the size of the direct P wave arrival. The arrow (Figure 2) points to an anomalously large, later-arriving receiver phase on the radial component which is substantially larger than direct radial P. This arrival is not seen in other azimuths implying that plane layered earth structure may not be a good approximation for structure in the area (e.g., Langston, 1979).

Figure 3 shows P-wave form data recorded at SAO from the 8/14/88 Sea of Okhotsk event. SAO structure is inferred to be radically heterogeneous near the surface since the tangential component of motion for first arriving P is as large as the vertical component. This effect changes with

azimuth and frequency and will be described in the companion study. Since SAO is located at the trace of the San Andreas fault, the extremely large near-surface effect on particle motions must be due to velocity structure within the fault zone (e.g., Thurber, 1983). Of interest to this study on coda is the simple observation that the direct P wave is severely affected by lateral heterogeneity and may be focussed or defocussed. The amplitude of direct P, relative to later arriving coda waves, is important when inverting for coda parameters.

Theory and Data Analysis

Details of the development of the energy flux coda model are found in Langston (1989a). Conceptially, the model is based on the assumption of a vertically incident P plane wave which propagates upward from a homogeneous halfspace into a layer containing scatterers. The P-wave is assumed to be impulsive so that its duration is much less than the traveltime through the layer. Consideration of conservation of energy scattered from the P wave into coda gives the level of coda amplitude. Ignoring the displacement of the direct P wave, coda amplitude at the free surface of the layer is given by:

$$A_c(\omega,t) = \sqrt{\frac{I_D}{t_d}} \; e^{\frac{\omega t_d}{2Q_r}} \left(1 - e^{-\frac{\omega t_d}{Q_r}}\right)^{\frac{1}{2}} e^{-\frac{\omega t}{2Q_r}} \tag{1}$$

where, ω is circular frequency, t_d is the average travel time of the direct wave through the layer, Q_s is the scattering Q of the layer and Q_r is the "radiative" Q which governs diffusion of coda waves out of the layer into the underlying halfspace. Given ground velocity, $v(t)$, of the incident P wave pulse centered around some circular frequency ω, the factor I_D is given by

$$I_D = \int_{t_1}^{t_2} v^2(t)dt \tag{2}$$

The integration bound t_1 is the P wave arrival time but t_2 must be estimated from the data and must be such that it includes all of the incident P pulse. Estimating t_2 is difficult for emergent and long duration signals.

The theory for equation (1) was developed assuming a scalar wave field, such as pressure, with scattering confined to the same wave type. Equation (1) is applied to three-component data with the understanding that the resulting parameterization results in empirical measures of coda decay and level. No assertions are made on the scattering mechanisms that go into coda formation. The three-component P-wave data for an individual earthquake are processed in the following manner since coda occurs on each component. First, each component is bandpass filtered using a zero phase Butterworth filter centered at a given frequency. The factor I_n is computed by choosing t_1 and t_2 from the vertical component of motion since the P pulse is most clear on this component. The integral is computed for the sum of the squares of the three components over the inferred time interval. This is the value of I_D. Next, the amplitude envelope of each component is found by computing the modulus of the analytic signal. The three envelopes are combined by summing the square of each amplitude sample point by point. The final coda envelope is the square root of the sum and is normalized by dividing by $\sqrt{I_D}$.

Once a coda envelope is obtained for an event, equation (1) is fit to the envelope using a least-squares algorithm on the logarithm of the coda envelope. The logarithm is used since the inversion will be linear for Q_r^{-1}. The zero intercept of the log coda envelope is related to Q_s^{-1} in a complicated way, but the least-squares inversion is performed iteratively until convergence. Synthetic tests showed that there was little starting model dependence in obtaining the Q^{-1} parameters and convergence occurred in all cases within five iterations.

Filtering was performed at three different center frequencies based on trial processing and examining noise levels in the teleseismic data. These center frequencies were at 1.5 (corner frequencies of 1 and 2 hz), 0.75 (corner frequencies of 0.5 and 1 hz) and 0.375 hz (corner frequencies at 0.25 and 0.5 hz). A three pole, phaseless, Butterworth filter was used in each case.

Zero lapse time for the coda was taken at the peak of the P wave arrival. This must be known to apply equation (1). The Q parameters were determined from the coda envelope for each event by inversion of 80 seconds of data starting 20 seconds after the P wave peak to avoid the direct P wave. Tables 3, 4 and 5 contain the values for each event and station. t_d was taken to be 10 sec using an average P wave velocity of 6 km/s for a scattering layer 60 km thick.

Discussion

The average standard deviation on inferred Q parameters was about 20%. However, it was found that coda decay rate measured by Q_r depended on source depth and coda level inferred from Q_s depended on recording station. Figure 4 shows correlograms of Q_r and Q_s for the three stations. The plots are for coda parameters taken from events which were recorded at the station pair BKS and MHC and at the pair SAO and MHC. Although values for Q_r scatter in magnitude among the event data, the correlograms show that Q_r correlates well between stations for the same event. Equation (1) shows that Q_r is proportional to the inverse slope of the log coda envelope. Thus, the good correlation for Q_r shows that coda decay rate is a stable quantity over the region for a single event.

The scattering Q, Q_s, is less well-behaved. Figure 4 shows that the correlation between stations is not very good and that Q_s determinations can easily vary by factors of two for the same event. Q_s is a measure of coda level relative to the direct wave and therefore depends directly on how well $\sqrt{I_D}$ is determined. A major assumption in the coda theory is that the direct wave only loses energy in scattering and is not affected by any other wave propagation effect. Thus, the reliance of coda level on the direct wave implicitly assumes that the direct wave is not focussed or defocussed by the scattering medium. This is probably the weakest assumption contained in any coda theory since the amplitude of the input wave to the scattering medium is never a known quantity. Figure 5 demonstrates that differential focussing of the direct wave occurs over the network. Shown are the P-wave vertical components for the 9/07/88 Honshu event. Note the factor of three difference in

amplitude between BKS and SAO for the direct P-wave yet the coda levels remain comparable. The empirical evidence of Figures 4 and 5 suggests that determination of coda level and Q_s is a noisy process in the analysis of teleseismic P codas at single receivers and that it may be better to forgo normalization by the direct wave amplitude. Constancy seen in coda levels across the network also strongly supports the assumption of general homogeneity of the scattered coda field, justifying this assumption in the energy flux model.

Figure 6 shows a compilation of all inferred Q_r values plotted versus event source depth. High Q_r values imply that slope is small and that coda decays slowly. In the single scattering model (Aki and Chouet, 1975), Q_r is interpreted in terms of scattering attenuation; high slopes mean greater attenuation. However, Langston(1989a) suggested that slow coda decay rate really implies that scattering effects are more severe than seen in teleseismic P codas which decay more quickly. Empirically, slow P-coda decay rates are associated with high coda levels relative to the direct P wave arrival.

The data (Figure 6) show that coda decay rate can be source depth dependent. Results for the 1.5 hz bandpass show that coda decay rate is about half as fast for the events above 100 km depth compared to deeper events. The data for the other two bandpasses do not show the same effect, however. It appears that coda decay rate is comparable for all events, regardless of source depth, for the 0.75 hz and 0.375 hz bandpasses. Coda data for all deep events at all stations were stacked to get the best estimate of Q_r and Q_s for the central California region. This, of course, assumes that coda associated with scattering near the source for these deep events is a minor contributor to the observed coda, an assumption that is discussed below. The coda and model fits are shown in Figure 7. Note the linearity of the coda slopes and how coda slope does not change much between the three frequency bands. Coda levels and slopes are comparable to those found for PAS station in Southern California for teleseismic deep events (Langston, 1989).

A simple model for coda formation is that most scattering occurs in the lithosphere with little or no scattering occurring along the body wave ray path throughout most of the deeper mantle.

Thus, coda is produced at the receiver from the random scattering of waves from lateral hetero-geneities and probably consist of body waves and body-to-surface wave conversions (e.g. Blakeslee and Malin, 1990; Langston, 1989a). Coda waves are also produced at the source, for sources within the lithosphere, and because of the teleseismic distances involved, travel to the receiver as P waves along paths very close to the direct P wave arrival. Although near-source scattering can involve complex effects, including for example Rayleigh wave-to-P wave conversions, the constraint on coda arrival times being comparable to the direct wave guarantees that source coda simply be a part of the effective source time function when it arrives at a teleseismic receiver.

The relative dominance of source and receiver coda can be assessed by the following simple analysis. Coda at the receiver can be thought of as the result of convolving the response of the receiver function, r(t), with the effective source function, s(t). The deep event data suggest that coda slope and approximate levels do not change much with frequency. Consider the following functional form for the source and receiver functions:

$$s(t) = \delta(t) + C_s(t)e^{-\gamma_s t} \tag{3}$$

$$r(t) = \delta(t) + C_r(t)e^{-\gamma_r t} \tag{4}$$

where $C_s(t)$ and $C_r(t)$ are random time series given by

$$C_s(t) = C_s \sum_{j=0}^{N} a_j \delta(t - j\Delta t) \tag{5}$$

$$C_r(t) = C_r \sum_{k=0}^{N} b_k \delta(t - k\Delta t) \tag{6}$$

C_s and C_r are source and receiver coda scaling factors controlling coda level and γ_s and γ_r are the source and receiver coda decay rate parameters for the source and receiver codas, respectively. The coefficients a_j and b_k of equations (5) and (6) are Gaussian distributed variates between -1 and 1, with zero mean, sampled every Δt. The Dirac delta functions, $\delta(t)$, in equations (3) and (4) represent

the "deterministic" response of the direct P wave from the source and at the receiver. The relative size of coda is controlled by the scaling factors and decay rates. Convolving (3) and (4) gives the vertical component of displacement, w(t) (see Appendix)

$$w(t) = \delta(t) + C_s(t)e^{-\gamma_s t} + C_r(t)e^{-\gamma_r t} + C_s C_r u(t)\frac{e^{-\gamma_s t} - e^{-\gamma_r t}}{\gamma_r - \gamma_s} \tag{7}$$

for different decay parameters and

$$w(t) = \delta(t) + \{C_s(t) + C_r(t)\}e^{-\gamma t} + C_s C_r u(t)t e^{-\gamma t} \tag{8}$$

if the two decay parameters are the same and equal to γ. The function u(t) is also a Gaussian-distributed random time series.

According to (7), if one of the decay constants is substantially less than the other (implying more scattering or higher levels of coda) for approximately equal initial levels, then the slope of the log coda envelope will be largely determined by this slower decay rate. If the decay constants are comparable or the same (equation (8)), then the coda will have the same amplitude decay at long lapse times but at shorter times may be dominated by the additional factor of t in the last term. In the case of the deep event data studied here (Figure 7) $\gamma_r = 0.023$ sec^{-1} on average for the three frequency bands (assuming that $C_s = 0$). If an effective source function from a shallow event has a coda decay rate comparable to this receiver coda decay rate, then the factor with t in equation (8) may be of the same order as the other exponential in the log coda. This has the effect of flattening the log coda envelope function biasing the slope to smaller decay constants.

An examination of the shallow event coda data for the 1.5 hz bandpass showed both simple linear coda decay starting at the P arrival for some events and more complex envelopes mimicking the behavior implied by equation (8) for other events. It should be stated that near-source reverberations and/or complex and lengthy source time histories for the shallow events can contribute

to increasing apparent coda levels at relatively short lapse times. It may be possible that these additional factors contribute to the difference in coda decay rates seen between the deep and shallow events.

However, there is no *a priori* reason why there should be a difference in Q_r parameters between shallow and deep events at 1.5 hz and not for the other frequency bands (Figure 6). The analysis technique of stacking coda from all three components of motion at the receiver will bias results toward the receiver since each horizontal component contributes just as much energy to the receiver coda as the vertical component and is fundamentally a result of scattering near the receiver. Thus, source-area scattering must be large to overcome or substantially add to the receiver coda signal. The data of Figure 6 suggests that scattering is very efficient near shallow sources at 1.5 hz. Perhaps the difference between frequency bands is related to a change in scattering mechanism such as increased Rayleigh-to-P wave conversion.

That some of the data show a source depth dependent coda decay rate suggests that source area scattering is important in forming teleseismic P coda. However, the ambiguity remains concerning the relative contribution of receiver and source area scattering. Several lines of evidence suggest that receiver structure heterogeneity usually dominates the formation of coda, particularly when deep event data are considered. First, particle motions are observed to be complex within the coda with very little evidence of rectilinear motions characteristic of body waves. Tangential motions almost always attain similar amplitude levels to radial motions in coda after teleseismic P. This remains true even after a source equalization operation where the vertical component is deconvolved from the horizontals in receiver function studies. When data from the same event are considered at several stations, as in Figure 5, focussing effects are confined to the early, impulsive parts of the record with the coda level being unaffected between stations. This has also been a common observation at teleseismic arrays which show large (order of magnitude) direct wave amplitude fluctuations for short-period P waves between elements of the array (e.g., Bungum et al, 1971). If significant coda were contained within the incident P wave from the source area, it would be expected that any focussing effects would identically affect both the impulsive part of the P wave

as well as the source area coda portion of the incident P. Since this is not observed for the deep events and because of obvious tangential components indicative of near-receiver scattering, we ascribe coda decay and level determined from the deep event data (Figure 7) to be due to scattering near the three receivers. The good correlation of coda decay rate and absolute coda level for the same deep event at the three receivers strongly supports the assumption of a homogeneously distributed coda field required by the energy flux model.

Conclusions

Coda induced by scattering of teleseismic body waves along the Hayward-Calaveras fault system, a structurely complex area of central California, displays characteristics similar to coda seen in receiver function data at Pasadena, California. Coda levels are relatively high compared to the direct P wave and the decay rate is slow. The use of broad band data from several receivers in the Berkeley network allow comparison of the stability of coda decay rates and levels over a frequency band of 2 to 0.25 hz. Using an energy flux model to parameterize coda decay rate by a radiative Q parameter, Q_r, and the coda level by the scattering Q, Q_s, the data in Central California show that coda decay rate is largely frequency independent and consistent between stations. Coda levels are referenced to the direct P wave and Q_s values show larger amounts of scatter between stations due to foccussing and defocussing of the direct P wave by heterogeneity under the receivers. Coda decay rate for 1.5 hz bandpass data from shallow earthquake sources is about twice as slow as coda decay rate from deep events. This effect is not seen at lower frequencies. The slower coda decay rate implies that the contribution of coda due to source area scattering increases above 1 hz and is comparable to scattering effects at the receivers.

Table 1

Event Parameters

Event	Date	Origin Time	Lat. (°)	Long.(°)	Depth (km)	mb	Region
1	02/10/87	00:59:28.5	19.49S	117.45E	395	6.2	Fiji
2	05/07/87	03:05:49.1	46.74E	139.23E	430	6.0	Sea of Okhotsk
3	07/08/87	11:50:14.7	26.97S	108.16W	10	6.1	Easter Is.
4	07/14/87	23:46:03.5	49.63N	147.83E	576	6.0	Sea of Okhotsk
5	07/16/87	05:46:29.5	33.06N	138.10E	310	5.3	Honshu
6	08/08/87	15:48:56.7	19.02S	69.99W	70	6.4	Chile
7	10/27/87	21:58:17.0	28.68S	62.93W	605	6.0	Argentina
8	03/25/88	19:36:46.4	62.15N	124.18W	10	6.1	NW Territories
9	04/12/88	23:19:55.5	17.19S	72.31W	33	6.1	Peru
10	04/25/88	10:10:33.8	7.79S	158.26E	44	6.1	Solomon Is.
11	08/10/88	04:38:26.5	10.20S	160.80E	38	6.1	Solomon Is.
12	08/14/88	10:56:57.5	54.61N	152.68E	645	5.4	Sea of Okhotsk
13	09/07/88	11:53:25.5	30.32N	137.37E	501	6.0	Honshu
14	10/08/88	04:46:27.8	18.69S	172.52W	65	6.6	Tonga Is.

Table 2

Data Coverage

Event	Distance from BKS (°)	Backazimuth from BKS (°)	BKS	MHC	SAO
1	125.5	271.9		*	
2	68.6	313.3		*	
3	66.0	166.3		*	
4	62.2	312.9		*	
5	77.2	302.1		*	
6	75.0	129.3	*	*	
7	86.5	130.9		*	
8	24.5	357.8		*	
9	72.2	129.8	*		*
10	86.6	257.4	*	*	
11	86.1	254.0	*	*	*
12	57.5	316.8		*	*
13	79.3	300.2	*	*	*
14	73.6	229.4	*	*	*

Table 3

Inversion results for Q_r and Q_s at MHC

(Q_r, Q_s)

Event	1.5 hz	0.75 hz	0.375 hz
1	118,83	117,180	66,45
2	200,297	97,88	115,43
3	-	176,126	-
4	199,89	117,54	-
5	191,329	149,106	-
6	279,149	135,129	-
7	226,120	151,116	-
8	351,274	235,73	69,19
10	417,205	185,107	150,137
11	289,307	137,121	106,52
12	207,342	117,106	104,299
13	163,289	100,83	-
14	370,366	164,124	85,96

Table 4

Inversion results for Q_r and Q_s at BKS
(Q_r, Q_s)

Event	1.5 hz	0.75 hz	0.375 hz
6	-	129,170	-
9	-	139,117	119,54
10	463,259	146,128	127,66
11	289,509	133,233	104,42
13	142,754	117,201	-
14	276,270	163,105	91,63

Table 5

Inversion results for Q_r and Q_s at SAO
(Q_r, Q_s)

Event	1.5 hz	0.75 hz	0.375 hz
9	-	150,133	119,54
11	351,267	113,154	234,66
12	209,106	143,232	75,103
13	160,236	106,144	-
14	329,311	148,157	98,114

Appendix

The convolution of s(t) with r(t) (equations 3 and 4) is straightforward except for the term

$$C_s(t)e^{-\gamma_s t} * C_r(t)e^{-\gamma_r t} \tag{A1}$$

This convolution is approached by using the discrete form of the time series, equations (5) and (6), for both the random component and the decaying exponential. Let

$$h(t) = C_s \sum_{j=0}^{N} a_j e^{-\gamma_s j \Delta t} \delta(t - j\Delta t) \tag{A2}$$

$$g(t) = C_r \sum_{k=0}^{N} b_k e^{-\gamma_r k \Delta t} \delta(t - k\Delta t) \tag{A3}$$

The Fourier transforms are

$$\hat{h}(\omega) = C_s \sum_{j=0}^{N} a_j e^{-\gamma_s j \Delta t} e^{-i\omega j \Delta t} \tag{A4}$$

$$\hat{g}(\omega) = C_r \sum_{k=0}^{N} b_k e^{-\gamma_r k \Delta t} e^{-i\omega k \Delta t} \tag{A5}$$

Performing the convolution h(t)*g(t) by spectral multiplication

$$\frac{\hat{h}(\omega)\hat{g}(\omega)}{C_s C_r} = a_0 b_0$$

$$+ \left(a_0 b_1 e^{-\gamma_r \Delta t} + a_1 e^{-\gamma_s \Delta t} b_0 \right) e^{-i\omega \Delta t}$$

$$+ \left(a_0 b_2 e^{-\gamma_r 2\Delta t} + a_1 e^{-\gamma_s \Delta t} b_1 e^{-\gamma_r \Delta t} + a_2 e^{-\gamma_s 2\Delta t} b_0 \right) e^{-i\omega 2\Delta t}$$

$$\vdots$$

$$= \sum_{n=0}^{N} \sum_{j=0}^{n} \left\{ a_j e^{-\gamma_s j \Delta t} b_{n-j} e^{-\gamma_r (n-j)\Delta t} \right\} e^{-i\omega n \Delta t} \tag{A6}$$

Since the a_j and b_{n-j} are random variates between 1 and -1 their product, c_{nj}, is also a random variate between 1 and -1 although the product distribution function is not Gaussian. A further complication is introduced by the decaying exponentials in equations (A3) and (A4) since the statistical nature of the Gaussian noise series does not remain stationary with time. Particular values of the new non-stationary random time series will depend on particular numerical realizations of a_j and b_k. However, a heuristic approach can be taken to gain some insight on the nature of the envelope function which is of primary interest to this discussion. The envelope is generally defined by those values which are maximum or minimum. Clearly, maxima and minima of the convolution occur when

$$c_{nj} \approx 1 \quad \text{or} \quad -1 \quad for \quad j = 0 \quad to \quad n \tag{A7}$$

By inspection of equation (A6), we see that at these time points

$$\frac{\hat{h}(\omega)\hat{g}(\omega)}{C_s C_r} = \sum_{n=0}^{N} \sum_{j=0}^{n} \left(e^{-\gamma_r j \Delta t} e^{-\gamma_s (n-j)\Delta t} \right) e^{-i\omega n \Delta t} \tag{A8}$$

which is just the discrete time series version of

$$e^{-\gamma_s t} * e^{-\gamma_r t}. \tag{A9}$$

In the absence of the decaying exponentials, equation (A6) can be transformed into the time domain by using the shift theorem to give

$$h(t) * g(t) = C_s C_r u(t) R(t) \tag{A10}$$

where R(t) is the linear ramp function and we define a new random function

$$u(t) = \sum_{j=1}^{N} d_j \delta(t - j\Delta t) \tag{A11}$$

For small j (short times) d_j is a statistical variate composed of the product of two Gaussian distributed variates with zero mean and chosen between the range -1 and 1. However, as j tends to large N,

the d_j increasingly become Gaussian distributed through the central limit theorem of the calculus of probabilities. The ramp function appears since the variance of the sum of the Gaussian variates contained in (A6) increases linearly with time.

Based on these arguments, an approximation to the inverse transform of (A6) can be given be finding the convolution of envolope functions (the decaying exponentials) as the new envelope function of $u(t)$. Therefore

$$h(t)*g(t) \cong C_s C_r u(t) \frac{e^{-\gamma_s t} - e^{-\gamma_r t}}{\gamma_r - \gamma_s} \qquad \text{if} \quad \gamma_r \neq \gamma_s$$

$$\cong C_s C_r u(t) t e^{-\gamma t} \qquad \text{if} \quad \gamma = \gamma_r = \gamma_s \qquad (A12)$$

Several numerical experiments were performed to investigate the behavior of the envelope of a number of realizations of (A1). It was found that (A12) was an adequate approximation for the purposes of this paper for the relatively slow coda decays observed in the data. Since C_s and C_r are always less than unity, the importance of this term is usually dominated by the other terms in the total convolution, equations (7) and (8).
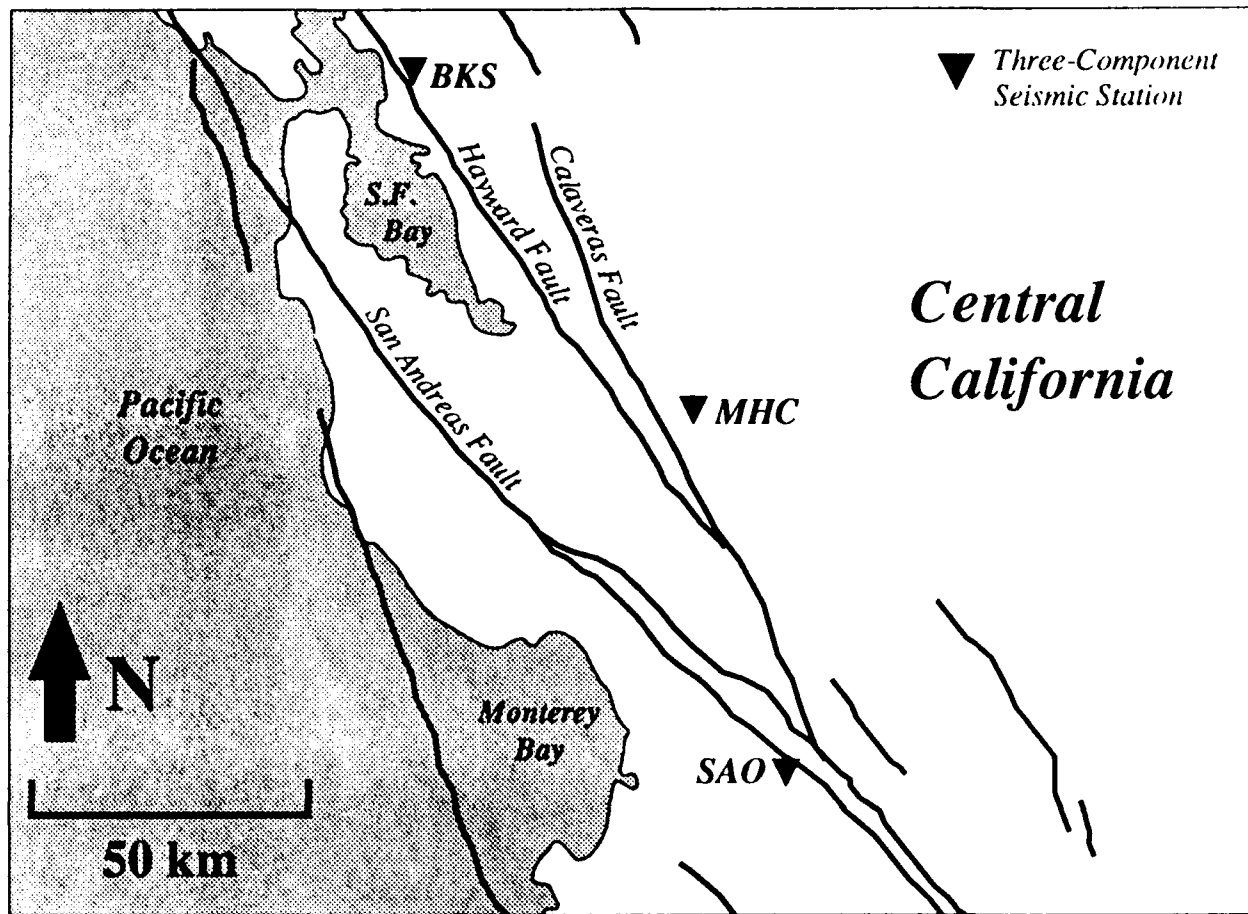
Figure 1: Sketch map of coastal Central California. Station locations for Berkeley (BKS), Mount Hamilton (MHC) and San Andreas Observatory (SAO) are shown. Major faults in the area are also shown.
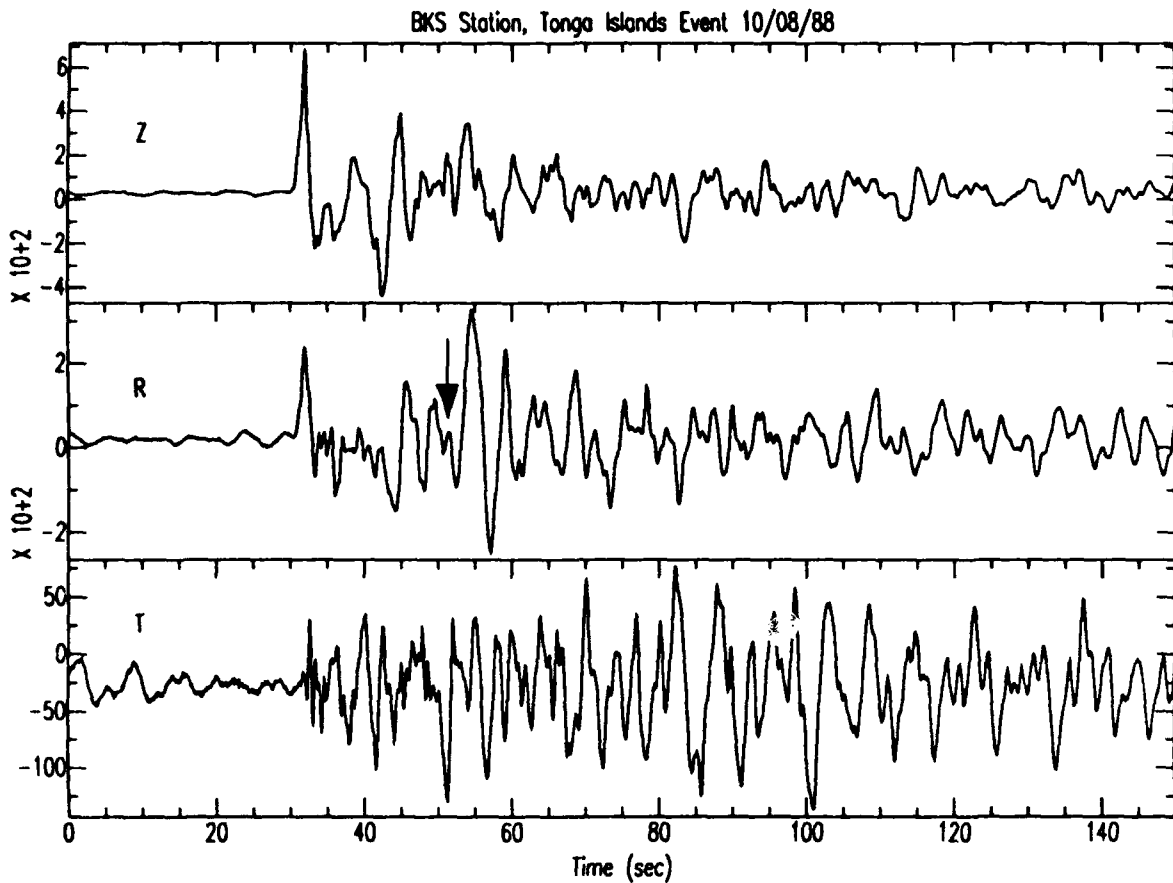
Figure 2: An example of three component data recorded at BKS for the Tonga
Islands event of 10/08/88. Z, R and T are the vertical, radial and
tangential motions for the P wave arrival, respectively. Note the
large arrival on the radial component annotated by the arrow. This
phase is azimuthally dependent and is largest for events of this
azimuth. Note also the growth of the tangential component with time,
suggesting the progressive scattering of the incident wave with local
velocity heterogeneity.
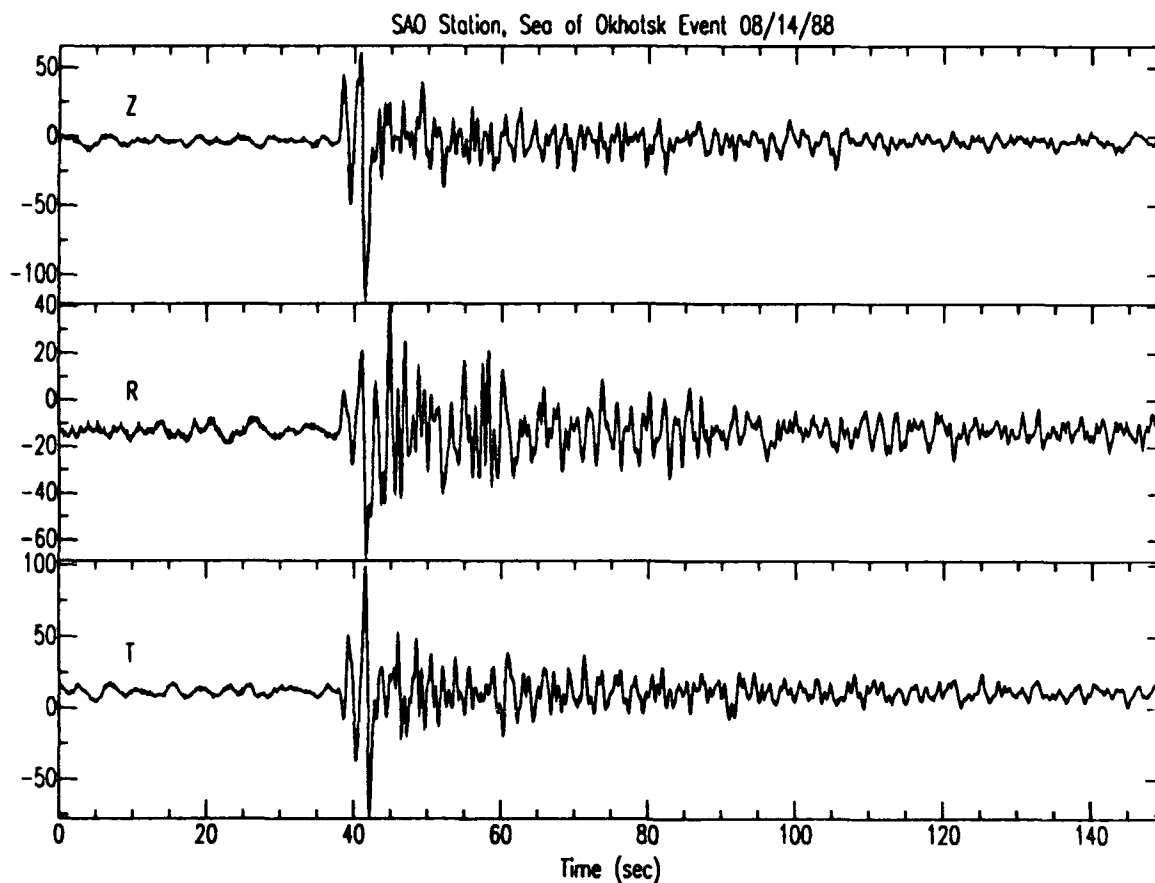
SAO Station, Sea of Okhotsk Event 08/14/88

Figure 3: An example of three component data recorded at SAO for the Sea of
Okhotsk event of 8/14/88. Same scheme as Figure 2. Note that the
tangential component is as large as the vertical component of motion
immediately at the P wave arrival time. This effect is frequency
dependent and largely disappears at lower frequencies. It is also
azimuthally dependent and is related to heterogeneous fault zone
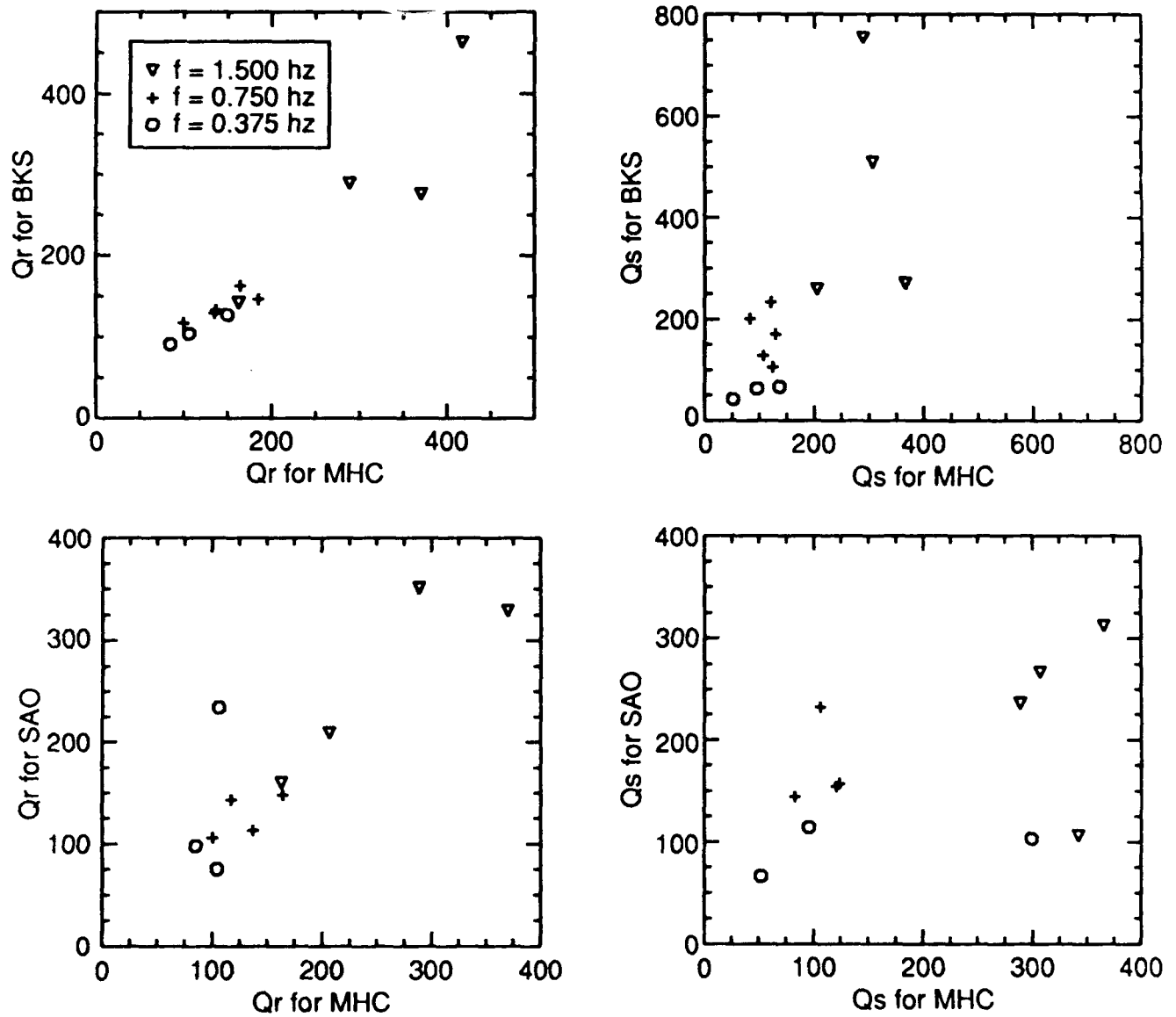structure in the upper 5 km of the crust.

Figure 4: Correlograms or scatter plots showing the correlation of Qr and Qs
measurements from the codas of events which were simultaneously
recorded at BKS and MHC (top) and SAO and MHC (bottom). The
different symbols denote Q parameters determined for three different
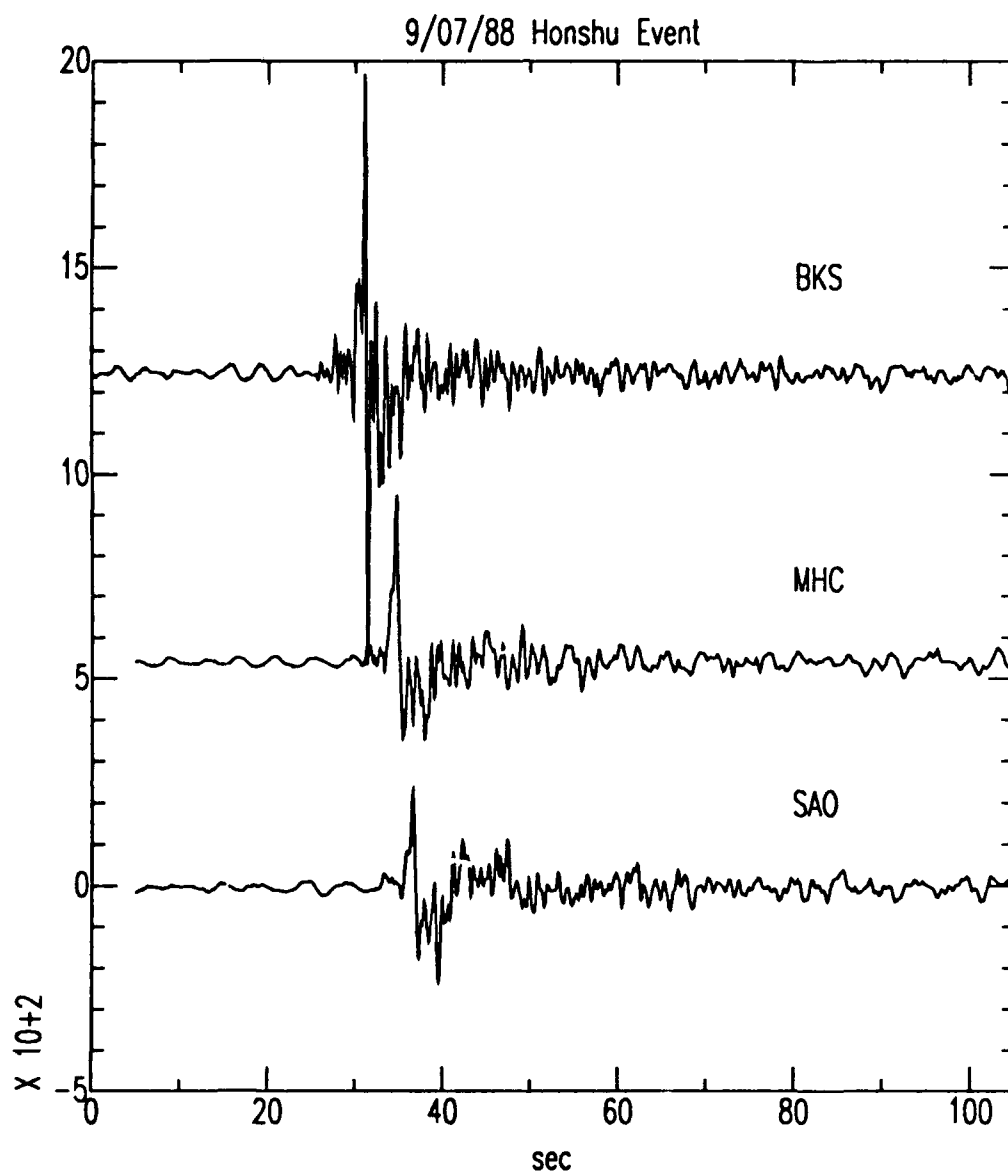bandpass filtered versions of the observed coda.

Figure 5: Vertical component of the P-wave for the 9/07/88 Honshu event
recorded at each station. Absolute amplitudes in digital counts are
displayed. The baseline of each trace has been shifted for display
purposes. Note that the BKS P-wave is about twice the amplitude of
the P-wave at MHC and three times the amplitude of the P-wave at SAO
due to focussing effects under the receivers. Coda amplitude levels,
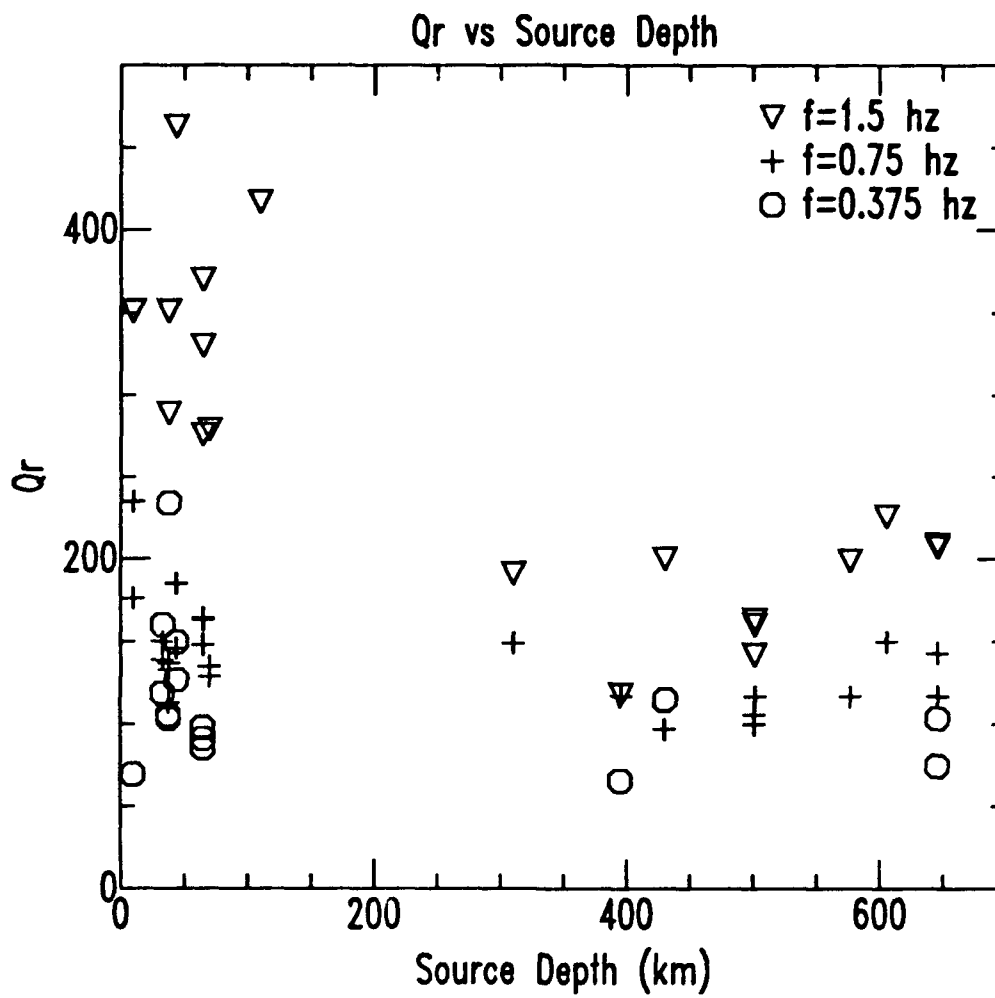however, are about the same.

Figure 6: Qr plotted versus event source depth for all stations and all events.
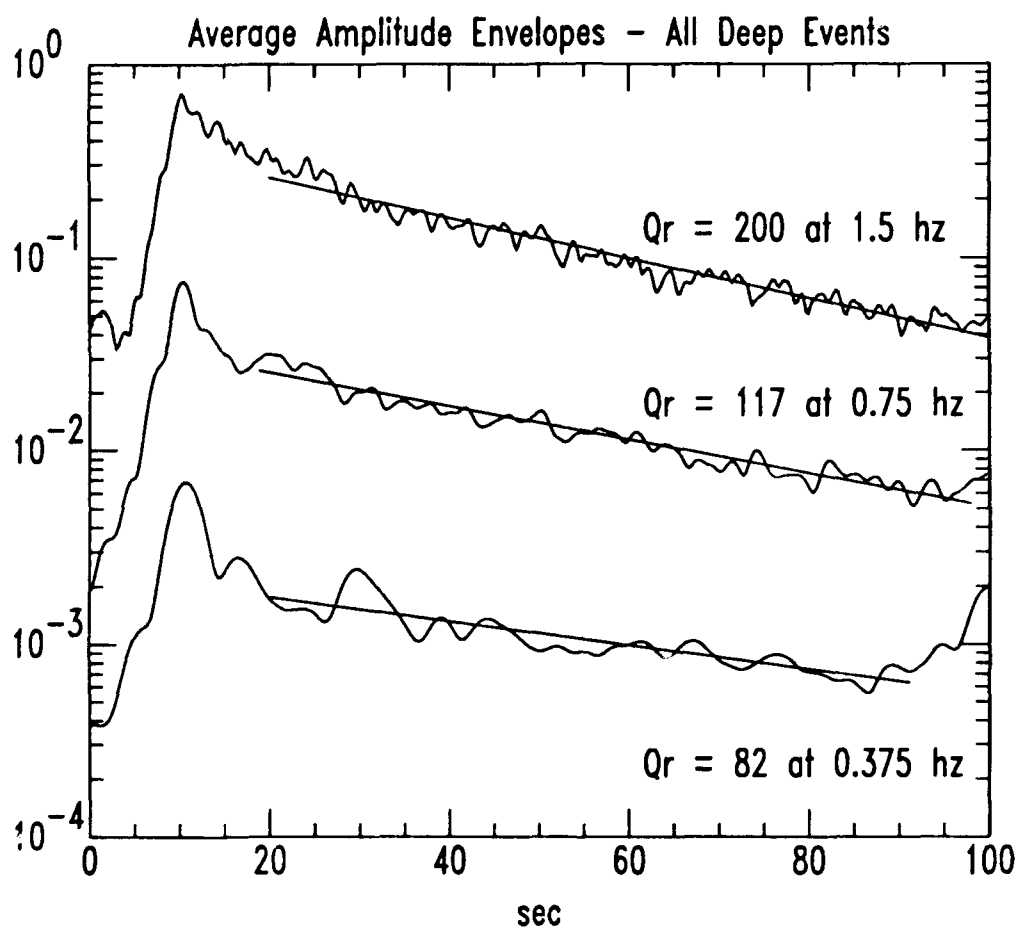
Figure 7: Stacked coda envelopes for all deep event data at all three stations.
Note the coda slope is essentially the same for all three passbands.
Inverted Qs values are, from top to bottom, 186, 101 and 115.

SCATTERING EFFECTS FOR TELESEISMIC PLANE WAVE

PROPAGATION IN A HETEROGENEOUS LAYER OVER A

HOMOGENEOUS HALF-SPACE

Gregory S. Wagner[†] & Charles A. Langston

Department of Geosciences

The Pennsylvania State University

University Park, PA 16802

[†] all correspondence should be made with

Gregory Wagner

Department of Geological Sciences

University of South Carolina

Columbia, SC 29208

Abstract

Numerical simulations of teleseismic wave propagation in a heterogeneous layer over a homogeneous half-space are conducted to further our understanding of teleseismic coda generation with the hope of shedding light on the generation of complex teleseismic particle motions. Acoustic and elastic finite difference synthetics are generated for more than 150 different layer over a half space models. The models vary in scattering layer thickness (L), heterogeneity correlation distance(s) (a, or a_x, a_z), and heterogeneity standard deviation (σ). The synthetic data are examined using relative coda intensity envelopes, to determine relationships that exist between the model parameters and the level and rate of coda decay, and frequency-wavenumber analysis to determine the wave types present in the scattered wavefield.

The level of scattered energy is found to be controlled by the ka value and the magnitude of the standard deviation (σ) of the perturbations. Coda levels increase with ka from $ka < 1$ to $ka \sim 1$, and decrease with increasing ka for $ka > 1$. Scattered energy levels are found to always increase with increasing σ. A more complex relationship is found to exist between the coda level and decay rate, and variations in the scattering layer thickness. For models that vary in scattering layer thickness alone, coda level and decay rate changes did not occur independently of the values of ka and/or σ.

The rate of coda decay is found to be controlled by the aspect ratio (a_x/a_z) of the heterogeneities (spatial anisotropy). The two extreme models are those with homogeneous plane-layers, which exhibit the most rapid coda decay rates, and those with spatially isotropic heterogeneities ($a_x/a_z = 1$), which exhibit the slowest coda decay rates.

Acoustic and elastic models exhibit similar coda intensity envelope characteristics. Apparent scattering attenuation of the direct pulse is found to be

strongest for models with spatially isotropic heterogeneities.

Frequency-wavenumber analysis of the elastic synthetics reveals the mechanism responsible for the generation of coda in the synthetic data. For models with spatially isotropic heterogeneities, the coda is composed largely of low apparent velocity [LAV] waves (scattered S and possibly body-to-surface scattered waves) while the coda for models with homogeneous plane-layers is composed solely of vertically propagating layer reverberations. Decreasing the heterogeneity aspect ratio increases the total amount of scattered LAV energy produced. The onset time of the LAV energy is also controlled by the heterogeneity aspect ratio. For models with spatially isotropic heterogeneities, the LAV energy appears immediately after the initial arrival. For models with homogeneous, plane-layers, LAV energy never appears.

(**key words:** receiver function, teleseismic coda, P-to-S scattering, Gaussian correlation, spatial anisotropy, relative intensities, f-k analysis.)

(**page heading:** scattering effects for teleseismic wave propagation)

Introduction

The use of teleseismic waveform modeling to determine the location of major discontinuities in the earth's lithosphere was introduced over a decade ago by Burdick and Langston (1977). A major advantage of this method, often referred to as **receiver function** modeling, is that teleseismic data from a single, isolated receiver can be used to determine structural features in the area of the station. For Burdick and Langston's procedure to be valid we must assume that a homogeneous, plane layered structure exists beneath the station (Burdick and Langston, 1977; Owens, 1984). Unfortunately, observed data cannot always be modeled using simple plane-layered models (Langston, 1977b;1979); this problem becomes more severe when using broad-band or high-frequency data which are more sensitive to small scale heterogeneities (Owens, 1984; Owens et al., 1984,1987). Particularly troublesome in the teleseismic waveform modeling problem are complex P-wave particle motions which sometimes contain anomalously large transverse components (Langston, 1979;1989). Slightly more complex modeling procedures that utilize dipping layers (Langston, 1977b,1979), or curved interfaces (Lee, 1983; Lee and Langston, 1983) have been used to explain some data, but a great deal of the observed complex particle motion cannot be modeled using simple techniques (Langston, 1979;1989; Owens et al., 1987).

Attempts to help better explain and understand the wave propagation phenomena responsible for the observed teleseismic particle motions and teleseismic coda began in the early 1980's. Teleseismic wave propagation and scattering for complex, plane-layered structures were investigated by Richards and Menke (1983). It was approximately at this time that the large body of work on coda generation for local earthquakes began to see widespread application to the teleseismic problem. For the local earthquake case, the in-

terest in seismic **coda**, the scattered waves arriving after the arrival of the major seismic phases, began in the late 1960* and early 1970* with the introduction of the single backscattering model (Aki, 1969; Aki and Chouet, 1975). Since that time, many studies, both theoretical and numerical, have been conducted to help determine the relationship between the degree of heterogeneity of the earth's crust and upper mantle, and the behavior of seismic coda. Theoretical models include the single backscattering model (Aki, 1969,1980,1982; Aki and Chouet, 1975; Sato, 1977), multiple scattering models (Gao et al., , 1983a,1983b; Gao and Li, 1990; Zeng et al., 1990), diffusion models (Dainty et al., 1974; Nakamura, 1976,1977; Dainty and Toksöz, 1977; Kopnichev, 1977; Toksöz et al., 1988), energy-flux models (Frankel and Wennerberg, 1987), energy-flux with radiative diffusion models (Langston, 1989; Korn, 1990), and transport theory models (Wu, 1985,1988). Numerical investigations into the mechanisms responsible for coda generation include those for complex plane-layered structures (Richards and Menke, 1983; Langston, 1989), irregular surface and subsurface layers (Hill and Levander, 1984; Levander and Hill, 1985), and 2-D inhomogeneous half and whole-spaces (Frankel and Clayton, 1984,1986; McLaughlin et al., 1985; Dougherty and Stephen, 1988; Korn, 1990).

Despite the numerous studies investigating seismic coda, many questions about its origins and relation to the heterogeneities of the earth's crust and upper mantle remain unanswered, particularly for the teleseismic case. To help better understand how various heterogeneous structures affect teleseismic coda and waveforms in general, we have carried out a detailed numerical investigation into scattering effects for teleseismic wave propagation in a 2-D, randomly heterogeneous scattering layer over a homogeneous half-space. More than 150 models are tested to determine how the scattering layer thickness (L),

the heterogeneity correlation distance(s) (a, or a_x, a_z), and the the magnitude of the heterogeneity standard deviation (σ) affect teleseismic coda generation and apparent scattering attenuation.

Scattering effects for both acoustic and elastic media are studied by computing synthetic seismograms using finite [FD] difference techniques (Alford *et al.*, 1974; Kelly *et al.*, 1976; Frankel and Clayton, 1984; Frankel and Clayton, 1986). To simulate teleseismic wave propagation, waveforms are computed using a vertically propagating, broad-band (1-second Gaussian), plane compressional wave (P-wave) as the source. This incident pulse reflects from the free-surface at the top of the model, and is absorbed at the bottom to simulate its passage back into the mantle. Receivers located every 1 km record the data at the free-surface. The main questions for this study are: (1) Can the amplitude and rate of decay of the seismic coda be used to determine the degree of heterogeneity of the models? (2) What are the sources of the scattered energy? and (3) are the acoustic approximations and currently popular theoretical models applicable to the elastic teleseismic problem?

The synthetic waveforms are analyzed using two basic methods: 1) a comparison of relative coda intensity envelopes (Aki and Chouet, 1975; Frankel and Wennerberg, 1987; Langston, 1989), and 2) frequency-wavenumber [f-k] analysis. Relative coda intensity envelopes are computed for several pass-bands for each model, and compared in an attempt to reveal any relationships that exist between the various model parameters and the coda level and/or rate of decay. Frequency-wavenumber analysis is conducted in an attempt to identify the scattering sources and wave types present in the scattered wavefield.

Numerical Modeling

Models that simulate a randomly heterogeneous layer over a homogeneous half space were examined in this study. Finite difference numerical techniques were used because they [numerical techniques] are, at present, the only techniques available to compute waveforms for wave propagation through a media that varies randomly both laterally and vertically.

A complete statistical description of a randomly varying media can be obtained by specifying (Ishimaru, 1978): 1) a correlation function, 2) a correlation distance (a)and, 3) a standard deviation of the perturbations (σ). To accurately describe wave propagation through a randomly varying medium, a wave's propagation distance through the medium must also be know. This propagation distance is often given in terms of the dimensionless **normalized propagation distance**, L/a (Chernov, 1960; Ishimaru, 1978).

With these model variables in mind, we generated a combined total of more than 150 acoustic and elastic models that varied in correlation distance(s) (a, or a_x, a_z), percent standard deviation (σ), and scattering layer thickness (L). The three basic types of models used are: 1) 1-D models with randomly varying, homogeneous plane-layers, 2) 2-D models with randomly distributed, spatially isotropic heterogeneities, and 3) 2-D models with randomly distributed, spatially anisotropic heterogeneities. Model parameters were varied in a systematic manner in order to span a large range of normalized wavenumbers, normalized propagation distances, and standard deviations. Perturbations were in velocity only; the density was 2.5 g/cm^3 for both the layer and the half-space for all models. The acoustic models had a mean layer velocity of 5 km/sec. The elastic models were for Poisson solids (Poisson's ratio=0.25) with mean layer velocities of 6 and 3.46 km/sec for the P- and S-waves, respectively. All models have half-space acoustic/P velocities of 8 km/sec (S-wave

half-space velocity=4.62 km/sec).

Each set of models was generated using every possible permutation of the following parameters:

- scattering layer thickness — L was 15, 30 or 45 km.

- standard deviation of the velocity perturbations — σ was 5, 10, 15 or sometimes 20% of the mean layer velocity.

- correlation distance(s)

  o models with spatially isotropic heterogeneities — a was 1, 2.5, 5, 7.5 or 10 km.

  o models with spatially anisotropic heterogeneities — a_z was 1, 2.5 or 5 km for an a_x of 10, 25, 40, 50, 80 or 125 km.

Spatial velocity variations were computed using a Gaussian correlation function (Frankel and Clayton, 1986)

$$e^{-(x^2+z^2)/(a_x^2+a_z^2)} \quad \Leftrightarrow \quad \frac{(a_x^2 + a_z^2)}{2} e^{-(k_x^2 a_x^2 + k_z^2 a_z^2)/4} \qquad (0.1)$$

$$\text{spatial domain}(x, z) \quad \Leftrightarrow \quad \text{wavenumber domain}(k_x, k_z).$$

The decision to use a Gaussian correlation function was motivated by the availability of theoretical and numerical results from previous studies.

Figures 1 and figure 2 show examples of models with spatially isotropic and anisotropic heterogeneities, respectively (please note the difference in the scale of the two figures). These figures show the magnitude of the perturbations only. These perturbations are scaled and superimposed on the mean layer velocities to produce the actual models used in the finite difference simulations.

Finite Difference Modeling

Finite difference modeling techniques, accuracy and stability checks, and boundary conditions have been discussed in many papers (Alterman and Karal, 1968; Boore, 1972a,b; Landers and Claerbout, 1972; Alford *et al.*, 1974; Alterman and Loewenthal, 1974; Smith, 1974; Ilan *et al.*, 1975; Ilan and Loewenthal, 1976; Kelly *et al.*, 1976; Clayton and Engquist, 1977; Reynolds, 1978; Levander, 1988; Stephen; 1988; Daudt *et al.*, 1989). We used fourth-order accurate, inhomogeneous, displacement finite difference approximations to generate our synthetics waveforms. Based on our own accuracy and stability tests, we choose to use one-sided, stress-free boundary conditions at the surface (Ilan and Loewenthal, 1976), absorbing boundary conditions at the bottom [of the model] (Clayton and Engquist, 1977), and transparent boundary conditions at the sides (Wagner, 1990). The grid-spacing and time increments were 0.25 km and 0.02 secs, respectively. These increments allowed frequency resolution to 4 Hz. No intrinsic attenuation was included in any of the modeling (*i.e.* $Q = \infty$). The source pulse used for all modeling was a Gaussian shaped (broadband), 1 second, vertically propagating compressional plane wave. Acoustic models were 512 km wide, while the [spatially] isotropic and anisotropic [heterogeneity] elastic models were 256 and 430 km wide, respectively. Each model had a 15 km thick homogeneous half-space, which consisted of a homogeneous layer with an absorbing boundary (Clayton and Engquist, 1977). The computer time required to complete the models used in this study (using individually, but simultaneously, a SUN 3/280, 4/280, and TAAC-1 application accelerator board) can be measured in months. The elastic models took, at a minimum, an hour to compute 1 sec of surface recorded data.

Part I: Intensity Envelope Analysis

The main goal of the relative coda intensity envelope analysis is to look for relationships between the size, shape, extent and magnitude of the heterogeneities, and the level and rate of coda decay. The energy in the scattered wavefield is compared to that in the incident pulse by generating averaged intensity envelopes computed by stacking the relative intensity envelopes from 10 receivers located at 10 km intervals. We used a method introduced by Frankel and Wennerberg (1987) to compute these power spectral densities with respect to time.

Power spectral densities, $P(\omega, t)$, are calculated using the following procedure (Figure 3):

1) Filter raw data using two passes of a two pole Butterworth filter — noncausal, zero phase, 3 db down at the corners (center frequency ±0.25 Hz). The acoustic and elastic data were examined using 0.5, 1 and 2 Hz passbands.

2) Each band-passed trace is normalized to the intensity of its initial arrival. The normalization constant is the area of the squared amplitude of the incident pulse ($\sim$ intensity)

$$\int_{t_1}^{t_1 + \Delta t} \left| \phi(t) \right|^2 dt , \qquad (0.2)$$

where Δt is the duration of the initial pulse. These intensity envelopes, therefore, show the intensity of the coda **relative** to the intensity of the initial pulse. Absolute differences between models were not examined.

3) The envelope of each band-passed, normalized trace is calculated using its analytic time signal.

4) For each model and each pass-band, 10 envelopes, from stations spanning 100 km of the model, are calculated and stacked to give the final plots of log intensity *vs* time.

To avoid a deluge of figures, only a few selected results are shown. These figures used to illustrate these results are, of course, selected to clearly illustrate various points and may exhibit certain characteristics more clearly than results from the analysis of similar models, but attributes of a single model will not be used as evidence for phenomena that do not appear consistently. Because the acoustic and elastic envelopes exhibit similar characteristics for most cases, sometimes only one figure [acoustic or elastic] is shown to make a point.

Plane-Layered Models

Results obtained using 1-D models will not be discussed because they were unable to produce realistic coda decay rates, particularly for the elastic case where no horizontal [displacement] coda can be generated without introducing lateral media perturbations (for a vertically propagating pulse).

Models with Isotropic Heterogeneities

The following three sections discuss the results obtained from 2-D models with isotropically shaped heterogeneities. Again, the three model parameters that vary are the magnitude of the heterogeneity variance, the heterogeneity correlation distance, and the thickness of the heterogeneous layer. Most of these results are rather simple and agree with results from previous theoretical and numerical studies.

Changes in Correlation Distance

The heterogeneity correlation distance is directly proportional to the size of the heterogeneities, and inversely proportional to their number density per unit area. To determine the ka value it is important to remember that the mean layer velocities are 5 km/sec, 6 km/sec and 3.64 km/sec for the acoustic, and P and S velocities, respectively. The pass-bands examined are 0.5, 1 and 2 Hz.

A simple relationship exists between the scattered energy level and the ka value. The level of scattered energy increases with ka for $ka<1$, reaches a maximum near $ka \sim 1$ (where the wavelength is equal to the size of the heterogeneity), and begins to decrease with increasing ka for $ka>1$. This simple relationship holds regardless of the layer thickness and/or the standard deviation of the perturbations. Figure 4 shows the relative coda intensity [envelopes] for $ka \leq 1$ and $ka>1$. Figure 5 shows the vertical and horizontal displacement envelopes for elastic models that varied in correlation distance alone; $k_P a \leq 1$, where k_P is the P-wave wavenumber, for all envelopes in this figure.

While the effects of changing the correlation distance are clear, equally clear and just as important are coda intensity envelope characteristics that are not effected by changes in the correlation distance; namely, the rate of coda decay. Changes in correlation distance affect the level of scattered energy according to a simple ka relation, but have no noticeable affect on the rate of coda decay. This is evident in all of the figures and was true for all of the models we tested.

Changes in Standard Deviation

Changing the standard deviation of the perturbations had a very simple effect; increasing the standard deviation increases the level of scattered energy. This

effect holds regardless of the layer thickness and/or ka value. Figure 6 shows relative vertical and horizontal displacement intensity envelopes for elastic models that varied in percent standard deviation.

As with the models where only the correlation distance was varied, changes in the percent standard deviation effect the coda level but have no discernible effect on the rate of coda decay.

Changes in Scattering Layer Thickness

Effects caused by changes in the scattering layer thickness did not follow any simple relationships. The effect of scattering layer thickness has not, (to the authors' knowledge) been addressed in previous numerical simulations, but has been postulated to plav a role in coda levels and decay rates in energy-flux models (Langston, 1989; Korn, 1990).

The scattering layer thickness has no simple, unambiguous relationships to either the coda level or rate of decay. For models with varying scattering layer thicknesses, the coda level and rate of decay seem to to be related to both the ka value and the standard deviation. For some models changing the scattering layer thickness produced no marked difference in either the relative coda level or rate of decay (Figure 7, part a), but for other models, there are obvious changes in the both the level and rate of coda decay (Figure 7, part b). A majority of the data generated using models that varied in scattering layer thickness alone showed no consistent, systematic differences in either the coda level or rate of decay.

In some cases the scattering layer thickness does eflect the coda level and/or rate of decay, but these effects do not appear to occur independently of the value of ka and/or the standard deviation. Because of this apparently complex interrelationship, scattering layer thickness changes are not an appealing

mechanism for explaining coda characteristics because there is no simple, unambiguous cause and effect relationship between the scattering layer thickness and either the [relative] coda level or rate of decay.

Varying Pass-bands

The examination of different pass-bands of the same data set yielded coda level/ka relationships similar to those observed for the examination of data generated using models with different correlation distances. These ka relationships were most evident for $ka < 1$, and deteriorated for larger ka. For $ka < 1$, coda levels are directly proportional to ka, but for $ka > 1$, there are no clear trends (within the ka limits of this study). These ka relations held regardless of the scattering layer thickness and/or the standard deviation. Figures 8 and 9 show the vertical and horizontal intensity envelopes for elastic simulations where $ka < 1$ and $ka \geq 1$, respectively.

And again, as is the cases for changes in correlation distance and percent standard deviation, the band-passed data exhibited no noticeable differences in the rate of coda decay.

Models with Anisotropic Heterogeneities

To this point we have found several ways change the level of scattered energy, but have found no simple, systematic, unambiguous ways to control the rate of coda decay. This inability to easily and systematically control the coda decay rate [using models with isotropically shaped heterogeneities] motivated a modification of our model parameterization/generation procedure. The following section discusses the relative intensity envelope relationships revealed from the analysis of data generated using models with anisotropically shaped heterogeneities.

Approximately 45 acoustic models with anisotropically shaped heterogeneities were tested. The acoustic results allowed us to select four elastic models that would [best] characterize heterogeneity [spatial] anisotropy space. The most interesting results were those for models with a fixed a_z and varying a_x. The two extreme models are homogeneous, plane-layered structures ($a_x = \infty$), and models with spatially isotropic heterogeneities ($a_x = a_z$), both of which have been discussed in previous sections. The more [spatially] anisotropic models mimic plane-layered structures with layers of varying lateral extent. This type of model is intuitively appealing because it agrees with geological models that contain layers that do not have infinite lateral extent, but are truncated by faulting, folding or simple pinch outs.

Figures 10 and 11 show, respectively, the acoustic and elastic intensity envelopes for models with spatially anisotropic heterogeneities with a 30-km-thick heterogeneous layer and a 10% standard deviation. These envelopes clearly illustrate how the heterogeneity aspect ratio (spatial anisotropy) controls the rate of coda decay. The decay rates, like the models themselves, are bound by the spatially isotopic heterogeneity case ($a_x = a_z$), which exhibits the slowest decay rate, and the homogeneous, plane-layer case ($a_x = \infty$), which exhibits the most rapid decay rate.

The results using models with anisotropic heterogeneities provide one of the most significant results of this study. A simple cause and effect relationship exists between heterogeneity anisotropy and the rate of coda decay. The more spatially isotropic the heterogeneities (lower aspect ratio) the slower the rate of coda decay. Anisotropic heterogeneities simulate more plane-layered structures and produce less scattered energy. These are intuitively appealing explanations and have analogies to very heterogeneous, highly fractured, tectonically active areas which produce high levels of scattered energy, and more stable cratons

which are presumably more plane-layered and produce less scattering.

Discussion

The results from the relative coda intensity analysis can be best summarized in two figures. Figures 12 and 13 are composite plots showing relative coda levels and decay rates, respectively, for several different models. Figure 12 shows that coda levels are related to the ka value and the magnitude of the standard deviation of the perturbations. Scattered energy levels increase with ka for $ka < 1$ until $ka \sim 1$, and then begin to decrease with increasing ka for $ka > 1$. Increasing the standard deviation of the perturbations always increases the scattered energy levels. These effects have been observed in previous numerical studies (Frankel and Clayton, 1984,1986; Dougherty and Stephen, 1988). It is interesting to note the similarity between the levels of the vertical and horizontal components of the elastic synthetics (Figure 12). This similarity shows that the scattered energy is partitioned equally between the vertical and horizontal components.

Coda decay rates can be changed using different scattering layer thickness for only some models, but a less ambiguous and more physically appealing way to control the rate of coda decay is to vary the heterogeneity aspect ratio. Figure 13 shows that the main factor controlling decay rate is the heterogeneity aspect ratio. The end members of model space are models with spatially isotropic heterogeneities, which exhibit the slowest decay rates, and the homogeneous, plane-layered models (extreme spatially anisotropic heterogeneities) which exhibit the most rapid decay rates.

Although not shown in any of the figures, initial pulse amplitude attenuation is greatest for models with spatially isotropic heterogeneities. And the initial pulses for synthetics generated using models with spatially isotropic

heterogeneities had significantly lower high frequency content.

Part II: Frequency-Wavenumber Analysis

Frequency-wavenumber [f-k] analysis was used to help identify scattering source and the wave types present in the scattered wavefield. The graphical display of f-k results show, directly, the propagation directions and apparent velocities of any coherent [plan wave] energy traversing an array of receivers (Robinson, 1967; Gold and Rader, 1969; Beauchamp, 1973,1975; Claerbout, 1975; Ingate *et al.*, 1985; Kvaerna and Ringdal, 1986). We used one-dimensional [1-D] f-k analysis on the elastic synthetic data (vertical component only) to help identify the scattered waves crossing the array. The results were somewhat surprising and represent an aspect of scattering that has been neglected in deterministic and phenomenological coda decay models, as well as many previous numerical simulations that rely on an acoustic wave propagation assumption.

To avoid any contamination of the f-k results with model edge effects, the f-k analysis is conducted on data that should be void of edge effect arrivals. For models with spatially isotropic heterogeneities (256 km wide), the earliest arrival time for any S-wave edge effects at the center receiver is $\sim$37 secs. Our 11 stations array should, therefore, be free of S-wave edge effects for $\sim$35 secs. For models with spatially anisotropic heterogeneities (430 km wide), the earliest arrival time for S-wave edge effects is $\sim$60 secs; none of the analysis windows for the models with anisotropic heterogeneities go beyond 45 secs. The reason for the concern with only S-wave edge effects will become obvious shortly.

Spatially Isotropic Heterogeneities

The scattered wavefield produced by the models with [spatially] isotropic heterogeneities contains a great deal of low apparent velocity [LAV] energy that

is in the form of S-waves and/or body-to-surface-wave scattered energy. This LAV scattered energy is present in all of the [elastic] data generated using models with spatially isotropic heterogeneities. The heterogeneity correlation distance appears to play the major role in the production of this LAV energy.

Figure 14 shows 35 secs of the synthetic waveforms generated using models with spatially isotropic heterogeneities with correlation distances of 1 and 10 km — the two extreme models used in this study. The correlation distance is the only parameter that differs in these two models; the standard deviation and scattering layer thickness for both models are 10% and 30 km, respectively.

Frequency-wavenumber analysis was used to examine several different windows: (1) a window that included all of the data from 0-35 secs, (2) a 5 sec window containing the data between the initial arrival and the first multiple, and (3) two 5-sec windows containing data arriving after the first multiple but prior to any S-wave edge effects. The f-k spectra for these windows are shown in Figure 15. Several important features are shown in this figure, some that are common to both models ($a = 1$ km and $a = 10$ km), and several that differ.

The most noticeable and significant feature common to both data sets is t · presence of LAV energy immediately after the passage of the initial pulse. This LAV energy continues for the rest of the record and decays slowly with time.

There are also several differences between the two data sets. First, for the 0-35 sec window, it is obvious that the amount of LAV energy produced in the model with $a = 10$ km is much greater than that produced in the model with $a = 1$ km. This fact is further demonstrated by the later 5-sec windows. For all of the 5-sec windows, the $a = 10$ km synthetics contain more energy (see **max power** on the figures) than the $a = 1$ km synthetics. Secondly, the dominant frequencies and wavenumbers of the scattered waves is, in general,

much higher for the small heterogeneity model. This shows that the size of the scatterer is directly related to the wavenumber and frequency content of the scattered waves.

Spatially Anisotropic Heterogeneities

The f-k results for data produced using models with spatially anisotropic heterogeneities agree with those from the spatially isotropic heterogeneity models in some aspects, but differ in another important aspect. Models with anisotropic heterogeneities are capable of producing LAV scattered energy, but the onset time of this energy is delayed; the more anisotropic the heterogeneities, the longer the delay. The two [spatially] anisotropic heterogeneity models discussed here differ in horizontal correlation distance only; a_z is 5 km for both models, while a_x is 25 or 125 km. The data generated using these two models are shown in Figure 16. The f-k analysis of this data further emphasizes the importance of the P-to-S scattering mechanisms in the teleseismic coda problem.

Frequency-wavenumber analysis was performed on several windows, some identical and some from similar sections of the data. Figure 17 shows the f-k spectra for the data generated using the models with [spatially] anisotropic heterogeneities. It is important to remember that the low apparent velocity scattered energy generated by the spatially isotropic heterogeneity models began to arrive immediately after the incident pulse (Figures 14). Figure 17 (10-15 and 8-13 sec windows) shows the f-k spectra for the data recorded between the initial arrival and the first reverberation for the two spatially anisotropic heterogeneity models. Unlike the data from the spatially isotropic heterogeneity models, the scattered energy arriving immediately after the initial arrival consists mainly of vertically propagating waves (layer reverbera-

tions) with only a slight amount of LAV energy for the $a_x=25$ km model, and none for the $a_x=125$ km model. This trend continues further into the data with still no or very little LAV energy up to 25 secs. It is not until after 25 secs that the LAV energy energy begins to appear for the $a_x=25$ km model. For an identical window in the $a_x=125$ km data, there are still only vertically propagating waves, and the energy carried by these waves is decaying very rapidly. Windows further into each data set show that, for the $a_x=25$ km model, the familiar LAV energy has appeared, while for the $a_x=125$ km model, the now almost negligible energy is still mostly in the form of vertically propagating layer reverberations with only a minuscule amount of LAV energy.

Discussion

The f-k analysis of the synthetic data provides several significant results. First is the importance of P-to-S and possibly body-to-surface-wave scattering in the elastic problem, and second is the importance of heterogeneity aspect ratio in determining the magnitude of coda generation. For a model with spatially isotropic heterogeneities, LAV energy, in the form of P-to-S and/or body-to-surface-wave scattered energy, dominates the scattered wavefield and arrives immediately after the initial pulse. As the the aspect (a_x/a_z) ratio of the heterogeneities increases, LAV scattered energy is less evident and may not appear till much later in the data.

Heterogeneity aspect ratio is an intuitively appealing way to account for coda decay rate differences, in addition to complex particle motions observed in teleseismic coda. Models with spatially isotropic heterogeneities are void of any plane-layered structure and could be used to model highly-fractured, tectonically active regions which are often associated with higher levels of scattered energy. The spatially isotropic heterogeneity models are also capable

of producing significant amounts of horizontal displacement, a characteristic observed in some teleseismic data. Models with spatially anisotropic heterogeneities could be used to model stable, plane-layered regions.

The presence of P-to-S and possibly body-to-surface-wave scattered energy is also important in that these phenomena cannot be modeled with an acoustic approximation. The intensity envelope analysis suggested that acoustic simulations may be a good approximation to the elastic problem; the f-k analysis ahs shown that this is definitely not the case. The presence of coverted energy also suggests that most phenomenological scattering models must be further refined to include phase conversions.

Summary

Coda Levels and Decay Rates

This study has shown that coda levels are controlled by both the ka value and standard deviation of the perturbations, while coda decay rates are controlled by the aspect ratio of the heterogeneities. Scattered energy levels were found to increase for increasing ka from $ka \ll 1$ to $ka \sim 1$ at which point scattering levels began to slowly decrease with increasing ka. Scattered energy levels were also directly proportional to the magnitude of the standard deviation of the velocity perturbations. Both of these phenomenon occurred regardless of the scattering layer thickness, or the standard deviation of the perturbations. These ka and σ effects occurred for both elastic and acoustic media, and to an equal extent in the vertical and horizontal components of the elastic data.

Variations in scattering layer thickness had no simple, unambiguous effects on the coda. Level and decay rate variations caused by changes in the scattering layer thickness were also related to the value of ka and σ. While the exact effect of layer thickness is not clear, it does have an effect in some cases and should be investigated in more detail.

The inability to systematically control the rate of coda decay motivated use of models with anisotropically shaped heterogeneities. This reparameterization allowed us to easily control coda decay rates and provides an intuitively appealing mechanism to explain coda generation. The [two] extreme/end member models are those with spatially isotropic heterogeneities, and those with homogeneous, plane-layers. The homogeneous plane-layered models exhibited the most rapid decay rates, while those with spatially isotropic heterogeneities exhibited the slowest. Decay rates anywhere between the two extremes can be obtained by altering the aspect ratio of the heterogeneities. Physically,

these changes correspond to totally random structures with no layering (aspect ratio=1, spatially isotropic heterogeneities), and those with homogeneous, plane-layers (aspect ratio=∞; extreme spatially anisotropic heterogeneities). Tectonically, these models can be thought of as representations of highly fractured, tectonically active areas, and stable, more homogeneously plane layered cratonic regions.

Frequency-Wavenumber Analysis

The f-k analysis of the synthetic data showed that wide-angle (low apparent velocity) P-to-S scattering, and possibly body-to-surface-wave scattering, play a major role in teleseismic coda generation. In addition to the importance of surface and/or P-to-S-wave scattering are effects associated with the heterogeneity aspect ratio. Models with spatially isotropic heterogeneities generate LAV energy that immediately follows the incident pulse. The higher the heterogeneity aspect ratio (a_x/a_z) becomes, the longer is the delay between the passage of the initial pulse and the onset of LAV scattered energy. For the most extreme [spatially] anisotropic case (homogeneous plane-layers), LAV energy never appears and the coda is composed solely of layer reverberations. In short, the heterogeneity aspect ratio controls the rate of coda decay by controlling the rate at which vertically propagating teleseismic energy is scattered into the horizontal direction.

The f-k analysis also showed that there is a direct correlation between the frequency-wavenumber content of the scattered waves and the size of the heterogeneities. For models with spatially isotropic heterogeneities, the larger heterogeneities produce longer-wavelength (lower-frequency) scattered energy, and the smaller heterogeneities producing shorter-wavelength (higher-frequency) scattered energy.

Acknowledgments

References

Abramowitz, M. and I.A. Stegun (eds) (1972) *Handbook of Mathematical Functions*, Dover, New York.

Achenbach, J.D. (1984) *Wave Propagation in Elastic Solids*, Elsevier, New York.

Aki, K. (1969) Analysis of the seismic coda of local earthquakes as scattered waves, *J. Geophys. Res.*, **74**(2), 615-631.

Aki, K. (1973) Scattering of P waves under the Montana LASA, *J. Geophys. Res.*, **78**(8), 1334-1346.

Aki, K. and B. Chouet (1975) Origin of coda waves: source, attenuation, and scattering effects, *J. Geophys. Res.*, **80**(23), 3322-3342.

Aki, K. and P.G. Richards (1980) *Quantitative Seismology: Theory and Methods*, W.H. Freeman and Co., San Francisco.

Aki, K. (1980) Scattering and attenuation of shear waves in the lithosphere, *J. Geophys. Res.*, **85**(B11), 6496-6504.

Aki, K. (1982) Scattering and attenuation, *Bull. Seis. Soc. Am.*, **72**(6), S319-S330.

Alford, R.M., K.R. Kelly and D.M. Boore (1974) Accuracy of finite-difference modeling of the acoustic wave equation, *Geophysics*, **39**(6), 834-842.

Alterman, Z.S. and F.C. Karal Jr (1968) Propagation of elastic waves in layered media by finite difference methods, *Bull. Seis. Soc. Am.*, **58**(1), 367-398.

Alterman, Z.S. and D. Loewenthal (1970) Seismic waves in a quarter and three-quarter plane, *Geophys. J. R. astr. Soc.*, **20**, 101-126.

Beauchamp, K.G. (1973) *Signal Processing Using Analog and Digital Techniques*, George Allen and Unwin Ltd., London.

Beauchamp, K.G. (1975) *Exploitation of Seismograph Networks*, Nordhoff International Publishing, Leiden.

Ben-Menahem, Ari (1988) Vector-scattering of elastic waves by directional structural space gradients, *Pure and Appl. Geophys.*, 128(1/2), 133–146.

Blair, D.P. (1990) A direct comparison between vibrational resonance and pulse transmission data for assessment of seismic attenuation in rock, *Geophysics*, 55(1), 51–60.

Blakeslee, S.N. and P.E. Malin (1990) A comparison of earthquake coda waves at surface versus subsurface seismometers, in press: *J. Geophys. Res.*, 95(B1), 309–326.

Boore, D.M. (1972a) Finite difference methods for seismic wave propagation in heterogeneous materials. *In* B.A. Bolt (editor), *Seismology: Seismic Waves and Earth Oscillations* (Methods in Computational Physics, Vol. 11). Academic Press, New York.

Boore, D.M. (1972b) Finite difference methods for seismic wave propagation in heterogeneous materials. *in* Methods in computational physics: B. Alder, S. Fernbach, and M. Rotenberg (editors), Vol. 2, Academic Press, New York.

Burdick, L.J. and C.A. Langston (1977) Modeling crustal structure through the use of converted phases in teleseismic body waveforms, *Bull. Seis. Soc. Am.*, 67, 677–692.

Chandrasekhar, S (1960) *Radiative Transfer*, Dover, New York.

Chernov, L.A. (1960) *Wave Propagation in a Random Medium*, McGraw-Hill, New York.

Claerbout, J.F. (1976) *Fundamentals of Geophysical Data Processing With Applications to Petroleum Prospecting*, McGraw-Hill, New York.

Clayton, R. and B. Engquist (1977) Absorbing boundary conditions for acoustic and elastic wave equations, *Bull. Seis. Soc. Am.*, 67(6), 1529–1540.

Clayton, R.W. and B. Engquist (1980) Absorbing boundary conditions for wave-equation migration, *Geophysics*, 45(5), 895–904.

Dainty, A.M., M.N. Toksöz, K.R. Anderson, P.J. Pines, Y. Nakamura and G. Latham (1974) Seismic scattering and shallow structure of the moon in Oceanus Procellarum, *The Moon*, **9**, 11–29.

Dainty, A.M. and M.N. Toksöz (1977) Elastic wave propagation in a highly scattering medium — a diffusion approach, *J. Geophys.*, **43**, 375–388.

Daudt, C.R., L.W. Braile, R.L. Nowack and C.S. Chang (1989) A comparison of finite-difference and Fourier method calculations of synthetic seismograms, *Bull. Seis. Soc. Am.*, **79**(4), 1210–1230.

Dougherty, M.E. and R.A. Stephen (1988) Seismic energy partitioning and scattering in laterally heterogeneous ocean crust, *Pure and Appl. Geophys.*, **128**(1/2), 195–229.

Frankel, A. and R.W. Clayton (1984) A finite-difference simulation of wave propagation in two-dimensional random media, *Bull. Seis. Soc. Am.*, **74**(6), 2167–2186.

Frankel, A. and R.W. Clayton (1986) Finite difference simulations of seismic scattering: implications for the propagation of short-period seismic waves in the crust and models of crustal heterogeneity, *J. Geophys. Res.*, **91**(B6), 6465–6489.

Frankel, A. and L. Wennerberg (1987) Energy-flux model of seismic coda: separation of scattering and intrinsic attenuation, *Bull. Seis. Soc. Am.*, **77**(4), 1223–1251.

Frankel, A. (1989) A review of numerical experiments on seismic wave scattering, *Pure and Appl. Geophys.*, **131**, 639–685.

Gao, L.S., L.C. Lee, N.N. Biswas and K. Aki (1983a) Comparison of the effects between single and multiple scattering on coda waves for local earthquakes, *Bull. Seis. Soc. Am.*, **73**(2), 377–389.

Gao, L.S., N.N. Biswas, L.C. Lee and K. Aki (1983b) Effects of multiple scattering on coda waves in three-dimensional medium, *Pure and Appl. Geophys.*, **121**(1), 3–15.

Gao, L.S., S.L. Li (1990) Time domain solution for multiple scattering and the

coda envelopes, *Pure and Appl. Geophys.*, **132**, 123–150.

Gilbert, F. and G. Backus (1966) Propagator matrices in elastic wave and vibration problems, *Geophysics*, **31**, 7326–7332.

Gold, B. and C.M. Rader (1969) *Digital Processing of Signals*, McGraw-Hill, New York.

Greenfield, R.J. (1971) Short-period *P*-Wave generation by Rayleigh-wave scattering at Novaya Zemyla, *J. Geophys. Res.*, **76**(32), 7988–8001.

Harkrider, D.G. (1964) Surface waves in multilayered elastic media: I. Rayleigh and Love wave from buried sources in a multilayered elastic half-space, *Bull. Seis. Soc. Am.*, **54**, 627–679.

Haskell, N.A. (1953) The dispersion of surface waves on multilayered media, *Bull. Seis. Soc. Am.*, **43**, 17–34.

Herraiz, M. and A.F. Espinosa (1987) Coda waves: a review, *Pure and Appl. Geophys.*, **125**(4), 499–577.

Hill, N.R. and A.L. Levander (1984) Resonances of low-velocity layers with lateral variations, *Bull. Seis. Soc. Am.*, **74**(2), 521–537.

Hudson, J.A. (1977) Scattered waves in the coda of *P*, *J. Geophys.*, **43**, 359–374.

Hudson, J.A. (1980) *The Excitation and Propagation of Elastic Waves*, Cambridge Univ Press, New York.

Hudson, J.A. and J.R. Heritage (1981) The use of the Born approximation in seismic scattering problems, *Geophys. J. R. astr. Soc.*, **66**, 221–240.

Hudson, J.A. (1982) Use of stochastic models in seismology, *Geophys. J. R. astr. Soc.*, **69**, 649–657.

Ilan, A., A. Ungar and Z. Alterman (1975) An improved representation of boundary conditions in finite difference schemes for seismological problems, *Geophys. J. R. astr. Soc.*, **43**, 727–745.

Ilan, A. and D. Loewenthal (1976) Instability of finite difference schemes due

to boundary conditions in elastic media, *Geophys. Prosp.*, **24**, 431–453.

Ingate, S.F., E.S. Husebye and A. Christoffersson (1985) Regional arrays an optimum data processing schemes, *Bull. Seis. Soc. Am.*, **75**, 1155–1177.

Ishimaru, A (1978) *Wave Propagation and Scattering in Random Media*: vols I and II, Academic Press, New York.

Kanasewich, E.R. (1981) *Time Sequence Analysis in Geophysics*, University of Alberta Press, Winnipeg, Canada.

Kelly, K.R., R.W. Ward, S. Treitel and R.M. Alford (1976) Synthetic seismograms: a finite-difference approach, *Geophysics*, **41**(1), 2–27.

Kelly, K.R. and K.J. Marfurt (editors) (1990) *Numerical Modeling of Seismic Wave Propagation* Society of Exploration Geophysicists, Tulsa.

Knopoff, L. and J.A. Hudson (1964) Scattering of elastic waves by small inhomogeneities, *J. Acou. Soc. Am.*, **36**(2), 338–343.

Knopoff, L. and J.A. Hudson (1967) Frequency dependence of amplitudes of scattered elastic waves, *J. Acou. Soc. Am.*, **42**(1), 18–20.

Kopnichev, Yu. F. (1977) The role of multiple scattering in the formation of a seismogram's tail, *Izvestiya (Earth Physics)*, **13**(6), 394–398.

Korn, M. (1990) A modified energy flux model for lithospheric scattering of teleseismic body waves, *Geophys. J. Int.*, **102**(1), 165-175.

Kvaerna, T. and F. Ringdal (1986) Stability of various f-k estimation techniques. *NORSAR Scientific Rep. 1-86/87*, 29-40, Kjeller, Norway.

Landers, T. and J.F. Claerbout (1972) Numerical calculations of elastic waves in laterally inhomogeneous media, *J. Geophys. Res.*, **77**, 1476-1482.

Langston, C.A. (1977a) Corvallis, Oregon, crustal and upper mantle receiver structure from teleseismic P and S waves, *Bull. Seis. Soc. Am.*, **67**, 713-724.

Langston, C.A. (1977b) The effect of planar dipping structure on source and receiver responses for a constant ray parameter, *Bull. Seis. Soc. Am.*, **67**,

1029-1050.

Langston, C.A. (1979) Structure under Mount Rainier, Washington, inferred from teleseismic body waves, *J. Geophys. Res.*, **84**(9), 4749–4762.

Langston, C.A. (1989) Scattering of teleseismic body waves under Pasadena, California, *J. Geophys. Res.*, **94**, 1935–1951.

Lee, J.-J. (1983) A three-dimensional ray method and its application to the study of wave propagation in crustal structure with curved layers, Ph.D. thesis, Pa. State Univ., University Park.

Lee, J.-J. and C.A. Langston (1983) Wave propagation in a three-dimensional circular basin, *Bull. Seis. Soc. Am.*, **73**, 1637–1653.

Levander, A.R. and N.R. Hill (1985) *P-S* resonances in irregular low-velocity surface layers, *Bull. Seis. Soc. Am.*, **75**(3), 847–864.

Levander, A.R. (1988) Fourth-order finite-difference *P-SV* seismograms, *Geophysics*, **53**(11), 1425–1436.

Lysmer, J. and R.L. Kuhlemeyer (1969) Finite dynamic model for infinite media, *J. Eng. Mech. Div.*, *ASCE* **95** EM4, 859–877.

Malin, P.E. and R.A. Phinney (1985) On the relative scattering of *P*- and *S*-waves, *Geophys. J. R. astr. Soc.*, **80**, 603–618.

McLaughlin, K.L., L.M. Anderson and Z.A. Der (1985) Investigation of scattering and attenuation of seismic waves using 2-dimensional finite difference calculations, in *Multiple scattering of waves in random media and random rough surfaces*, V.V. Varadan and V.K. Varadan (editors), pp. 795–822, The Pennsylvania State University, University Park, Pa.

Mitchell, A.R. (1969) *Computational Methods in Partical Differential Equations*, John Wiley and Sons, New York.

Mitchell, A.R. and D.F. Griffiths (1980) *The Finite Difference Method in Partial Differential Equations*, John Wiley and Sons, New York.

Morse, P. E. and H. Feshbach (1953) *Methods of Theoretical Physics*: Parts I and II, McGraw-Hill, New York.

Nakamura, Y. (1976) Seismic energy transmission in the lunar surface zone determined from signals generated by movement of lunar rovers, *Bull. Seis. Soc. Am.*, **66**(2), 593–606.

Nakamura, Y. (1977) Seismic energy transmission in an intensively scattering environment, *J. Geophys.*, **43**, 389–399.

Owens, T.J. (1984a) Determination of crustal and upper mantle structure from analysis of broadband teleseismic *P* waveforms, Ph.D. thesis, Univ. of Utah, Salt Lake City.

Owens, T.J., G. Zandt, and S.R. Taylor (1984b) Seismic evidence for an ancient rift beneath the Cumberland Plateau, TN: A detailed analysis of broadband teleseismic *P* wave forms, *J. Geophys. Res.*, **89**, 7783–7795.

Owens, T.J., S.R. Taylor and G. Zandt (1987) Crustal structure at regional seismic test network stations determined from inversion of broadband teleseismic *P* waveforms, *Bull. Seis. Soc. Am.*, **77**, 631–662.

Press, W.H., B.P. Flannery, S.A. Teukolsky and W.T. Vetterling (1988) *Numerical Recipes in C*, Cambridge University Press, New York.

Rayleigh, J.W.S. (1894) *The Theory of Sound*: vols I & II, MacMillan Co., reprinted by Dover Publications Inc. (1945), New York.

Reynolds, A.C. (1978) Boundary conditions for the numerical solution of wave propagation problems, *Geophysics*, **43**(6), 1099–1104.

Richards, P.G. and W. Menke (1983) The apparent attenuation of a scattering medium, *Bull. Seis. Soc. Am.*, **73**(4), 1005–1021.

Robinson, E.R. (1967) *Statistical Communications and Detection*, Charles Griffin and Co., London.

Sato, H. (1977) Energy propagation including scattering effects: single isotropic scattering approximation, *J. Phys. Earth*, **25**, 27–51.

Sato, H. (1982a) Attenuation of *S* waves in the lithosphere due to scattering by its random velocity structure, *J. Geophys. Res.*, **87**(B9), 7779–7785.

Sato, H. (1982b) Amplitude attenuation of impulsive waves in random media

based on travel time corrected mean wave formalism, *J. Acou. Soc. Am.*, **71**(3), 559–564.

Sato, H. (1984) Attenuation and envelope formation of three-component seismograms of small local earthquakes in randomly inhomogeneous lithosphere, *J. Geophys. Res.*, **89**(B2), 1221–1241.

Sato, H. (1988) Is the single scattering model invalid for the coda excitation at long lapse time ?, *Pure and Appl. Geophys.*, **128**(1/2), 43–47.

Smith, W.D. (1974) A nonreflecting plane boundary for wave propagation problems, *J. Comp. Phys.*, **15**, 492–503.

Stephen, R.A. (1988) A review of finite difference methods for seismo-acoustics problems at the seafloor, *Reviews of Geophysics*, **26**(3), 445–458.

Toksöz, M.N., A.M. Dainty, E. Reiter and R. Wu. (1988) A model for attenuation and scattering in the earth's crust, *Pure and Appl. Geophys.*, **128**(1/2), 81–100.

Virieux, J. (1986) *P-SV* wave propagation in heterogeneous media: velocity-stress finite-difference method, *Geophysics*, **51**(4), 889–901.

Wagner, G.S. (1990) Scattering effects for teleseismic plane wave propagation in a heterogeneous layer over a homogenous half-space, Ph.D. thesis, The Pennsylvania. State University., University Park, 285 pp.

Wennerberg, L. and A. Frankel (1989) On the similarity of theories of anelastic and scattering attenuation, *Bull. Seis. Soc. Am.*, **79**(4), 1287–1293.

Wu, R. (1982) Attenuation of short period seismic waves due to scattering, *Geophys. Res. Letters*, **9**(1), 9–12.

Wu, R. and K. Aki (1985a) Elastic wave scattering by a random medium and the small-scale inhomogeneities in the lithosphere, *J. Geophys. Res.*, **90**(B12), 10261–10273.

Wu, R. and K. Aki (1985b) Scattering characteristics of elastic waves by an elastic heterogeneity, *Geophysics*, **50**(4), 582–595.

Wu, R. (1985) Multiple scattering and energy transfer of seismic waves — sepa-

ration of scattering effect from intrinsic attenuation: I theoretical modeling, *Geophys. J. R. astr. Soc.*, **82**, 57-80.

Wu, R. and K Aki (1985c) The fractal nature of the homogeneities in the lithosphere evidenced from seismic wave scattering, *Pure and Appl. Geophys.*, **123**, 805-818.

Wu, R. (1988) Multiple scattering and energy transfer of seismic waves — separation of scattering effect from intrinsic attenuation: II application of the theory to Hindu Kush region, *Pure and Appl. Geophys.*, **128**(1/2), 49-80.

Wu, R. and K. Aki (1988) Introduction: seismic wave scattering in three-dimensionally heterogeneous earth, *Pure and Appl. Geophys.*, **128**(1/2), 1-6.

Zeng, Y., F. Su, and K. Aki (1990) Scattering wave energy propagation in a random isotropic scattering medium: Part I. theory, submitted to *J. Geophys. Res.*
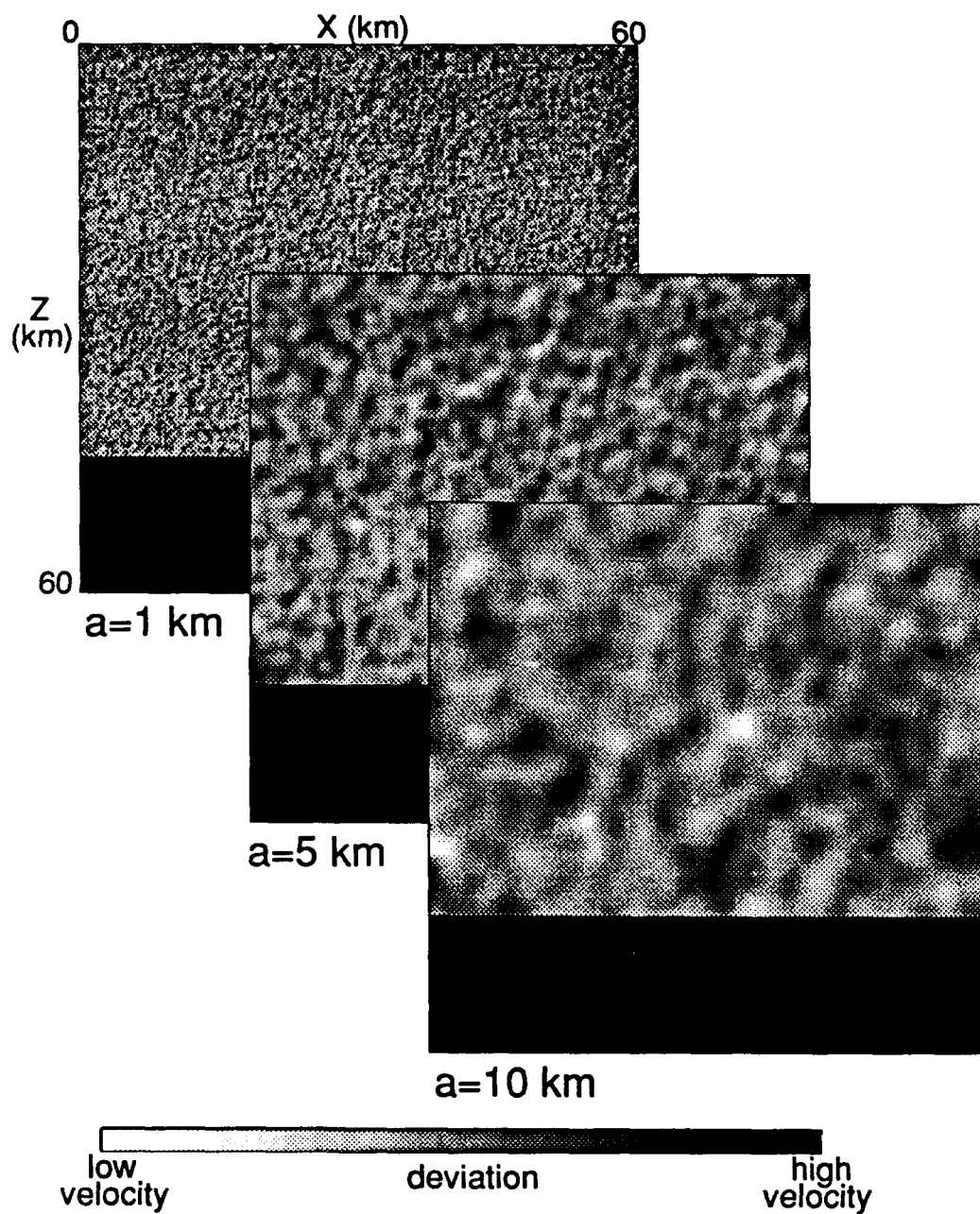
Figure 1: Spatially isotropic velocity perturbations generated using an isotropic Gaussian correlation function with correlation distance of 1, 5 and 10 km.
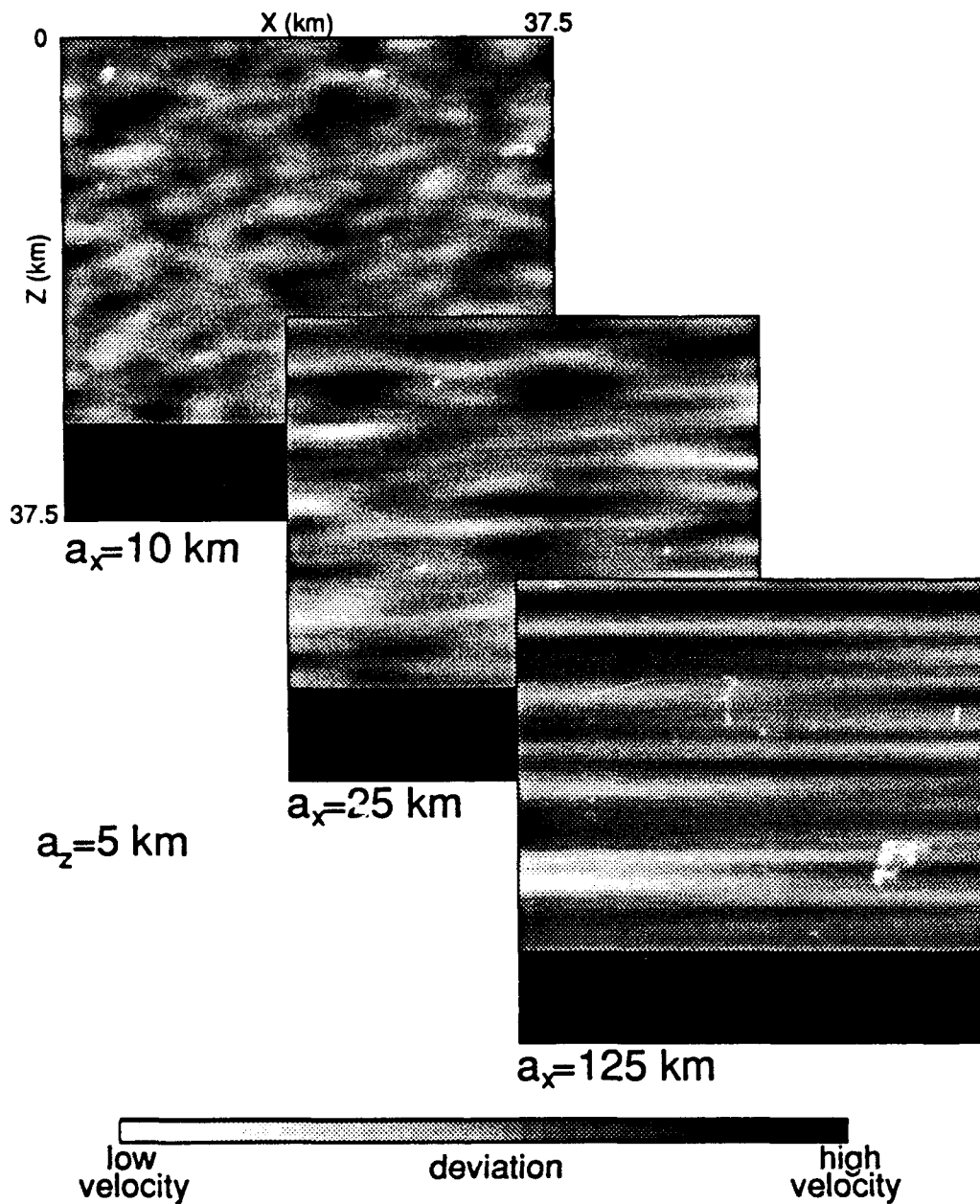
Figure 2: Spatially anisotropic velocity perturbations generated using an anisotropic Gaussian correlation function. All three models use $a_z=5$ km and $a_x=10$, 25 and 125 km.

Relative Coda Intensity Computation
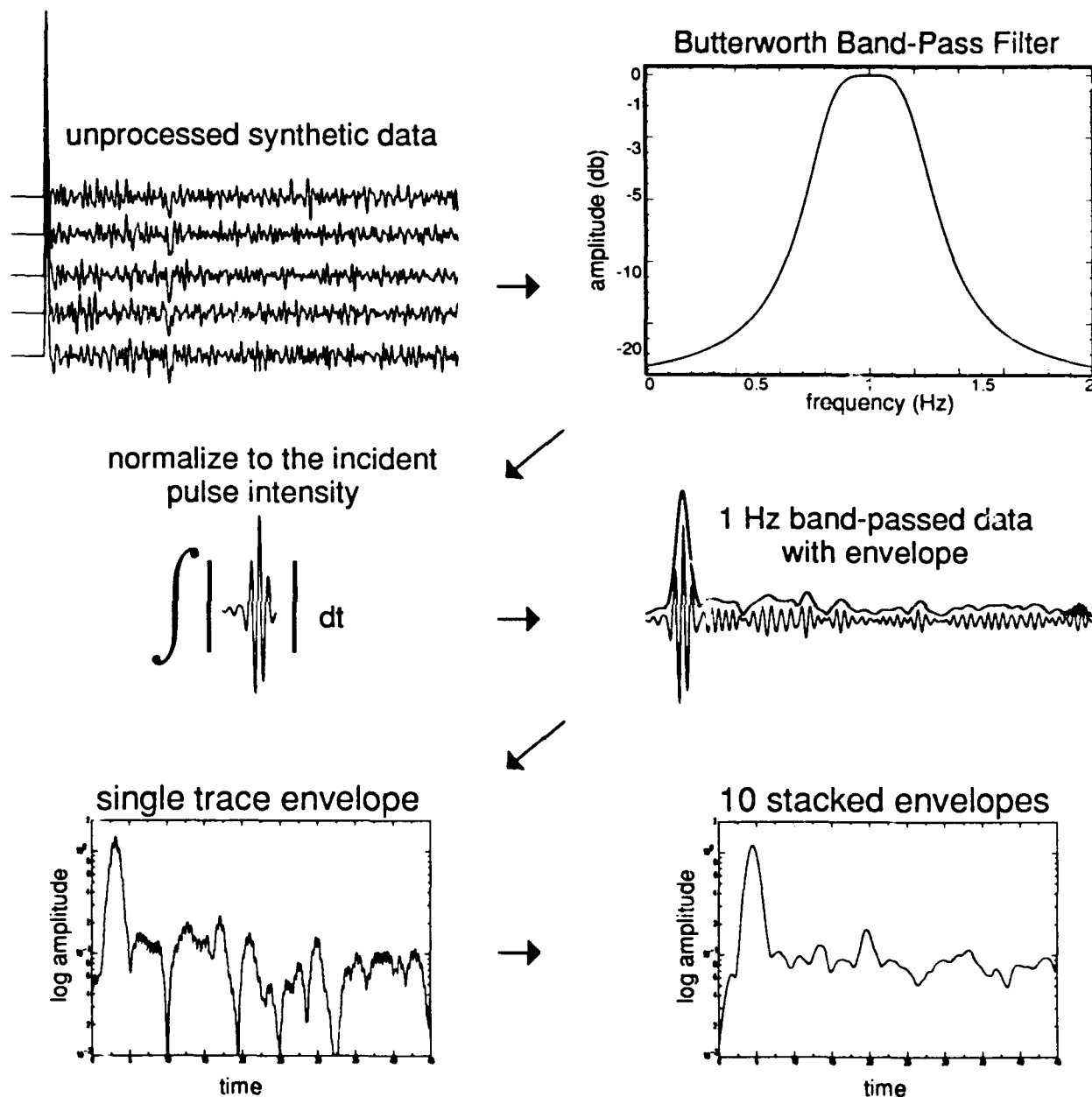
Figure 3: Procedure used to calculate relative coda intensity envelopes. The envelope above the band-pass filtered trace has been offset slightly for this figure.

Changes in Correlation Distance
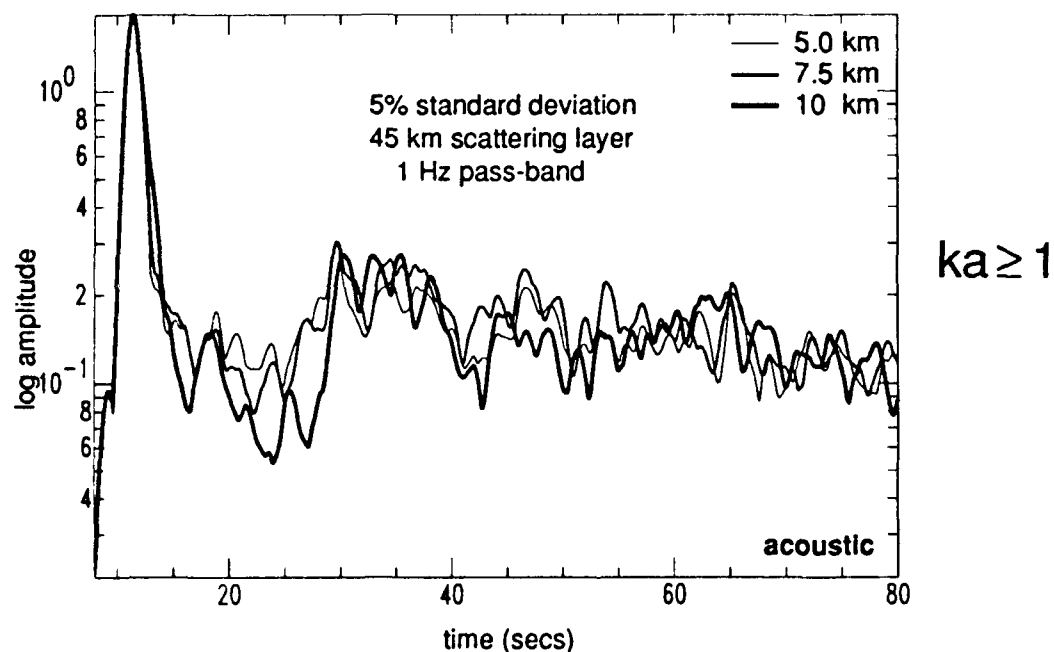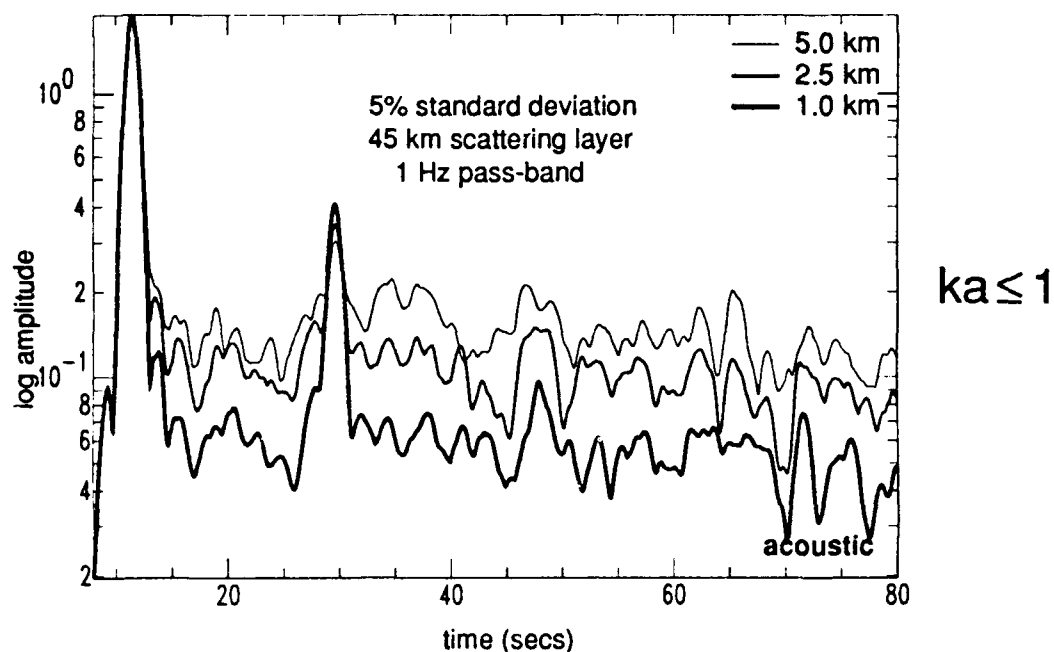
Figure 4: Relative acoustic coda intensity envelopes for models with spatially
  isotropic heterogeneities that vary in correlation distance.
  Correlation distances and the corresponding line weights are shown
  in the upper-right corner of the figure. The pass-band, scattering
  layer thickness and standard deviation are also listed on the figure.

Changes in Correlation Distance
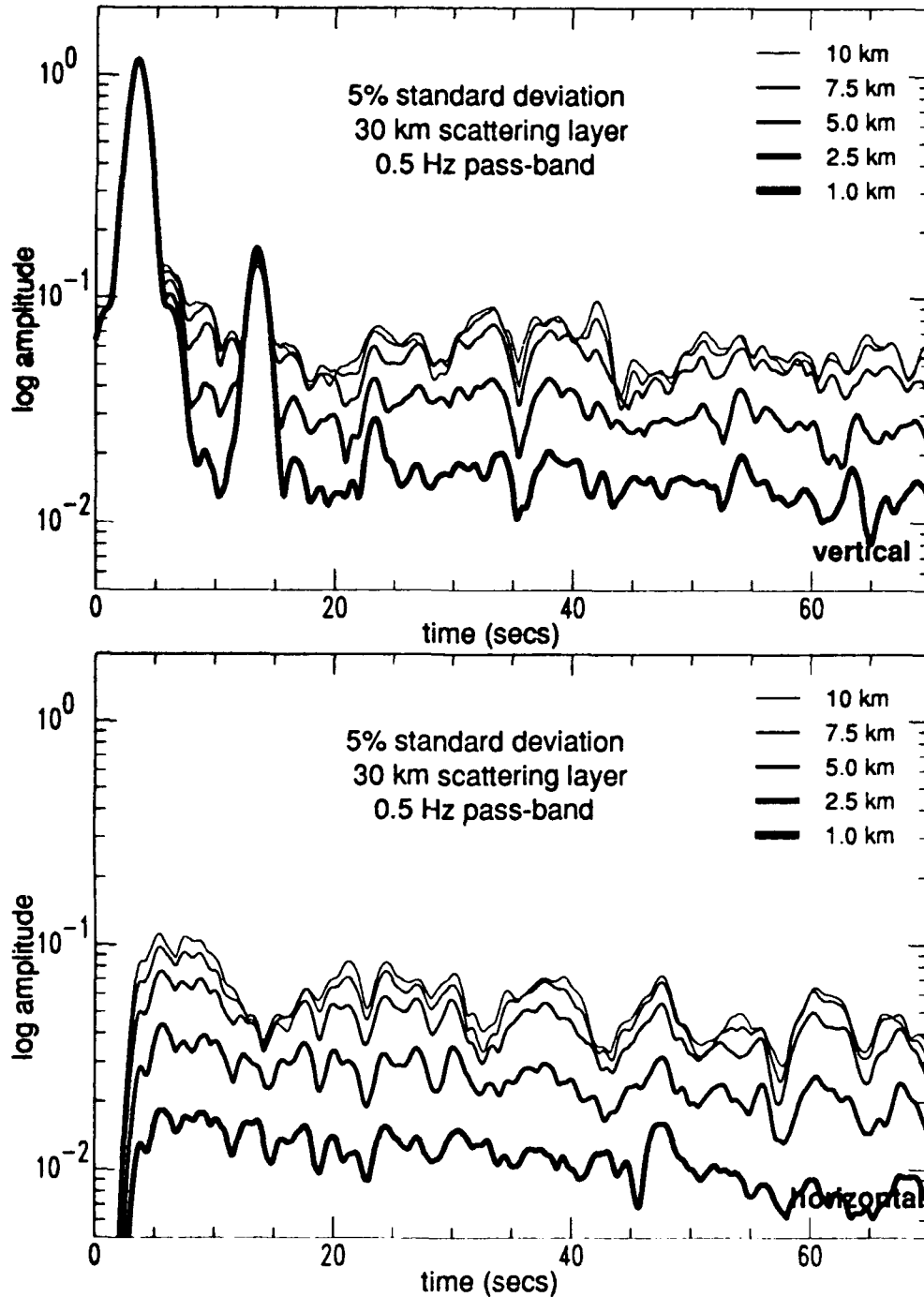
Figure 5: Relative elastic (vertical and horizontal displacement) coda intensity envelopes for models with spatially isotropic heterogeneities that vary in correlation distance. Correlation distances and the corresponding line weights are shown in the upper-right corner of the figure. The pass-band, scattering layer thickness and standard deviation and displacement component are also listed on the figure.

Changes in % Standard Deviation
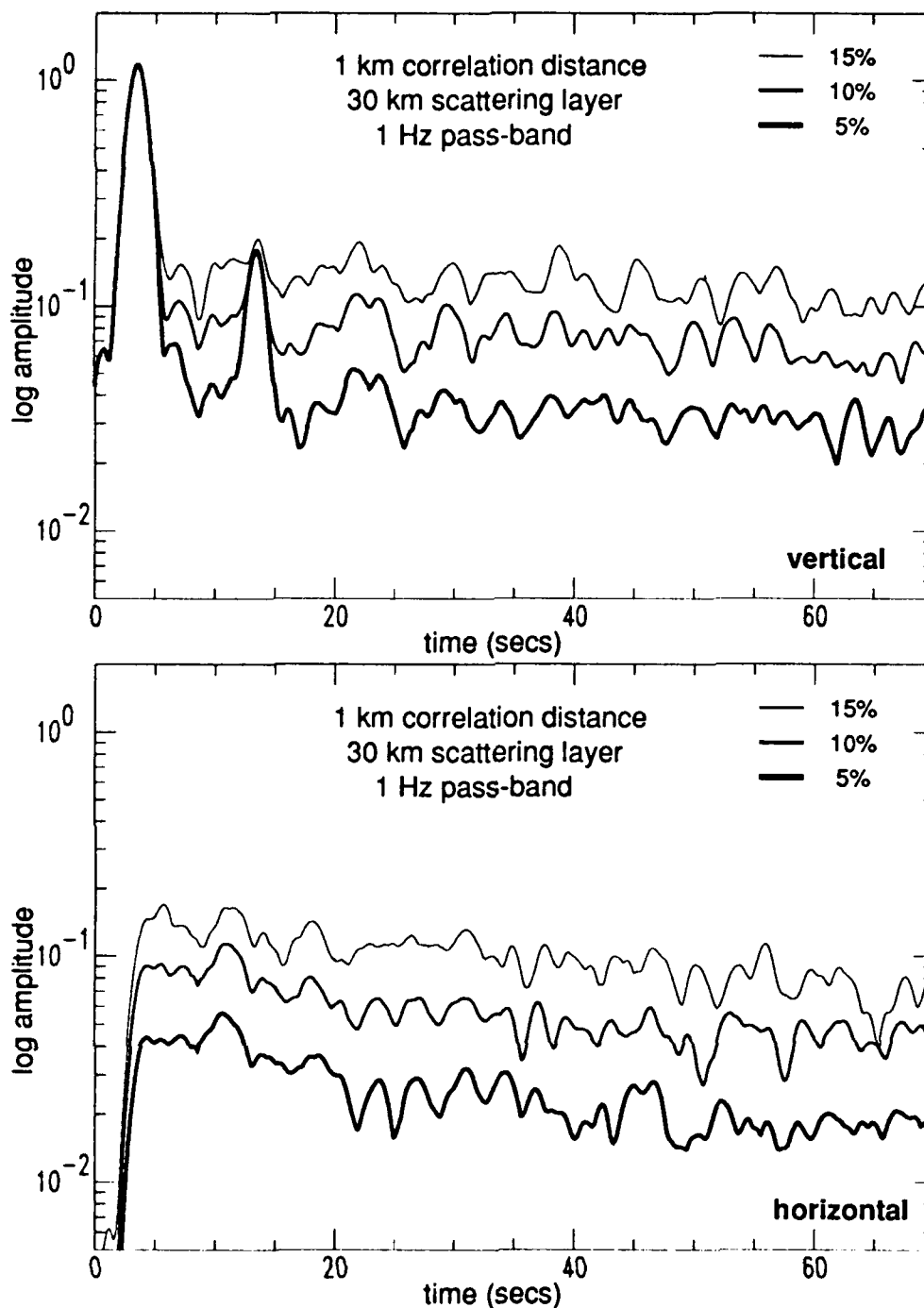
Figure 6: Relative elastic (vertical and horizontal displacement) coda intensities for models with spatially isotropic heterogeneities with different percent standard deviations. Percent standard deviation and the corresponding line weights are shown in the upper-right corner of the figure. The pass-band, scattering layer thickness, correlation distance and displacement component are also listed on the figure.

Changes in Scattering Layer Thickness
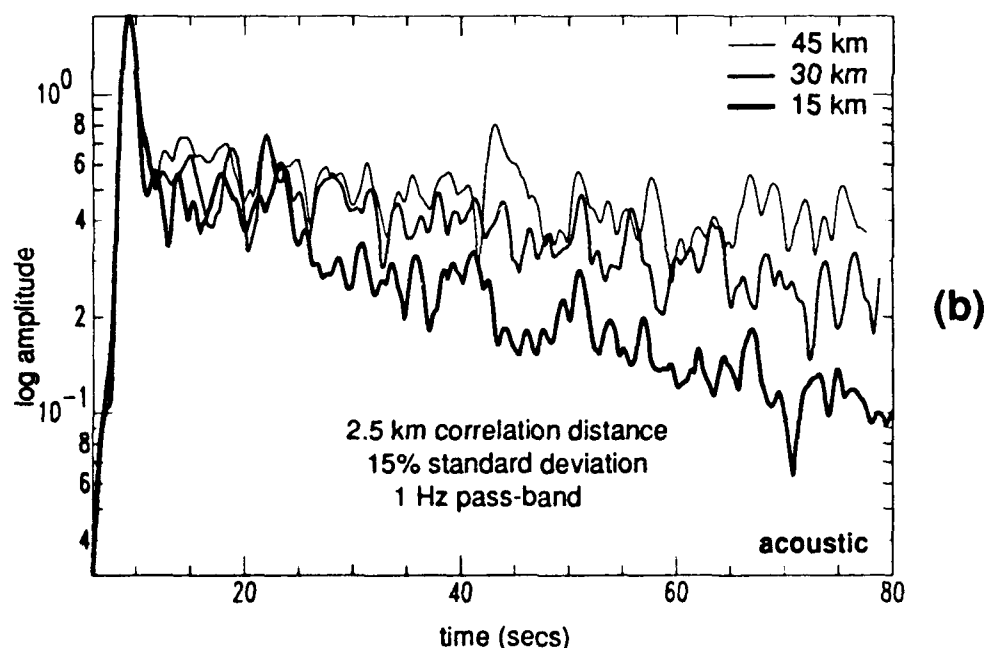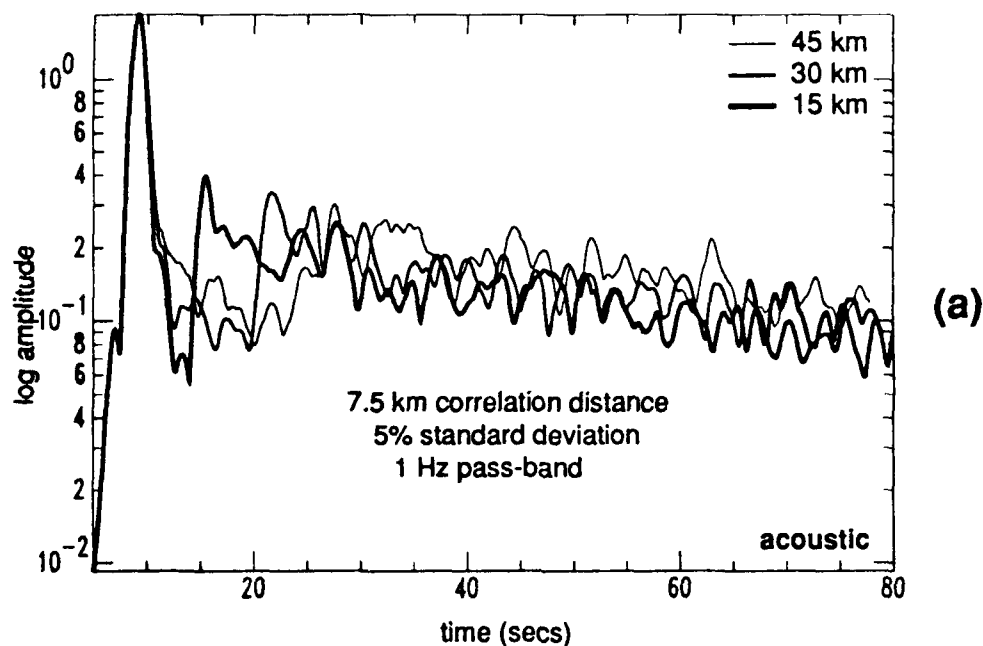
Figure 7: Relative acoustic coda intensity envelopes for spatially isotropic heterogeneity models that vary in scattering layer thickness. Scattering layer thicknesses and the corresponding line weights are shown in the upper-right corner of the figure. The passband, correlation distance and standard deviation are also listed on the figure. Part (a) exhibits no marked differences, while part (b) exhibits very different decay rates.
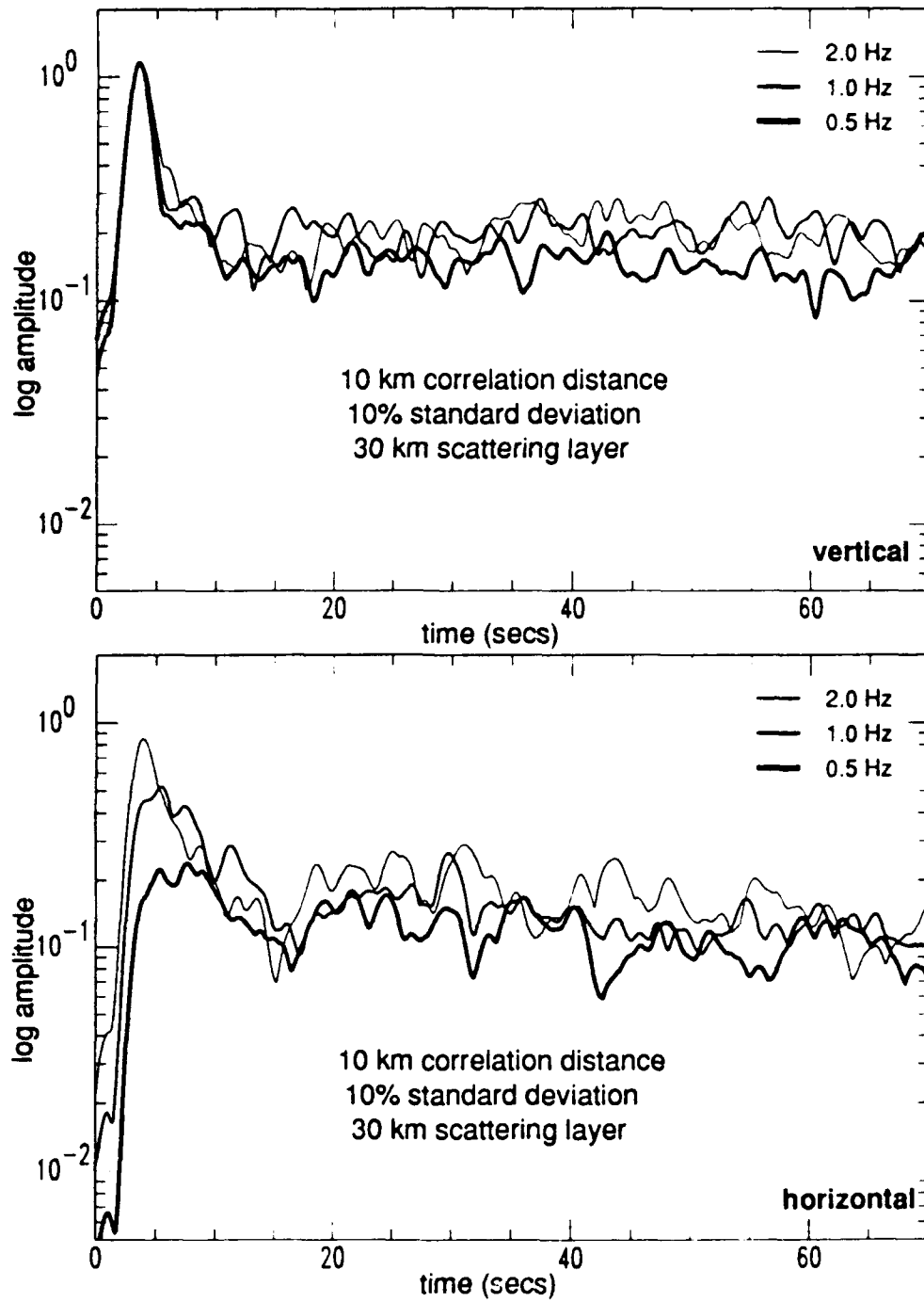
Changes in Frequency Pass-Band
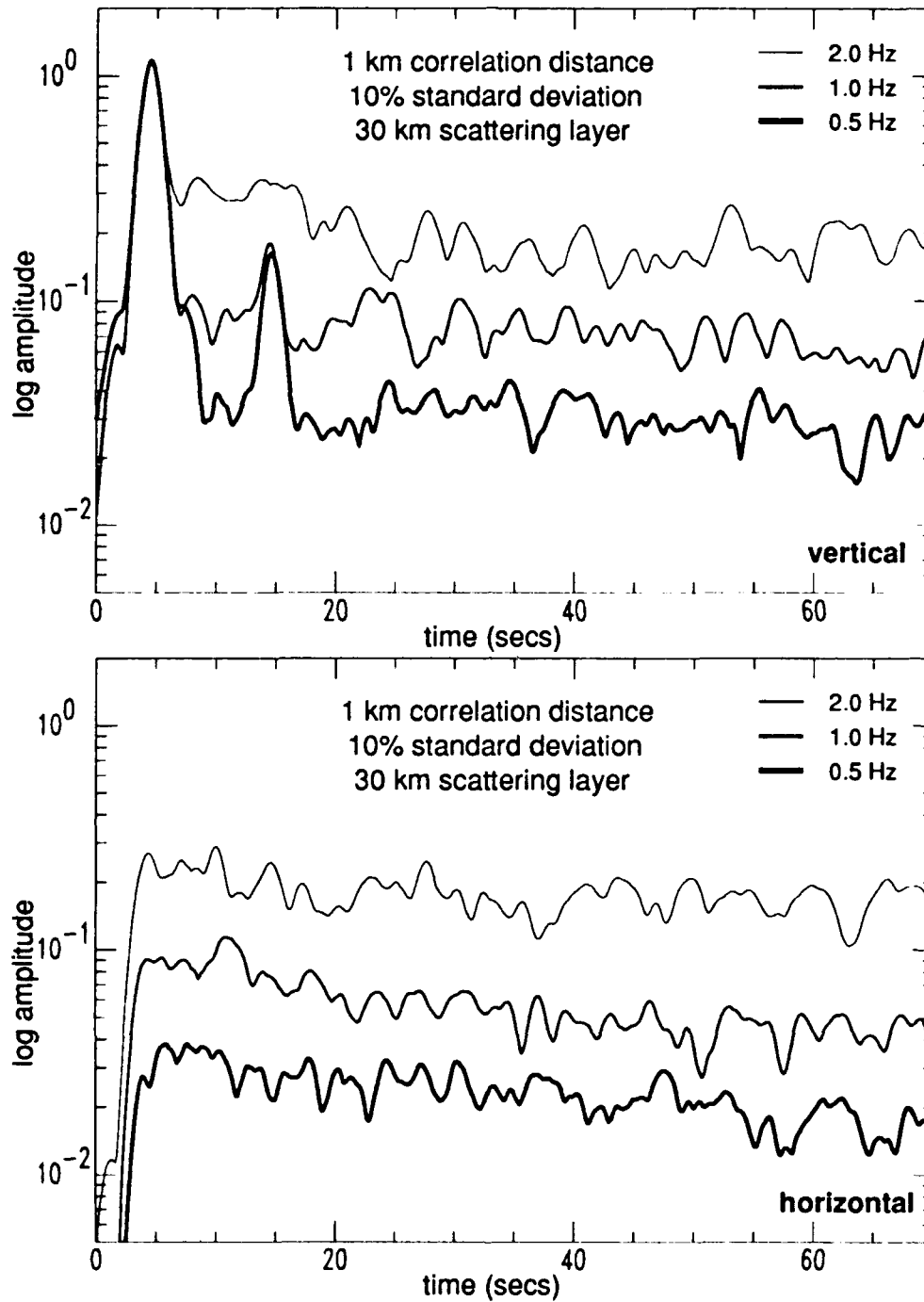
Figure 8: Relative coda intensity envelopes for different pass-bands of elastic data generated using models with spatially isotropic heterogeneities. The pass-band and the corresponding line weights are shown in the upper-right corner of the figures. The correlation distance, standard deviation, scattering layer thickness and displacement component are also listed on the figures.

Changes in Frequency Pass-Band

Figure 9: Relative coda intensity envelopes for different pass-bands of elastic data generated using models with spatially isotropic heterogeneities. The pass-band and the corresponding line weights are shown in the upper-right corner of the figures. The correlation distance, standard deviation, scattering layer thickness and displacement component are also listed on the figures.
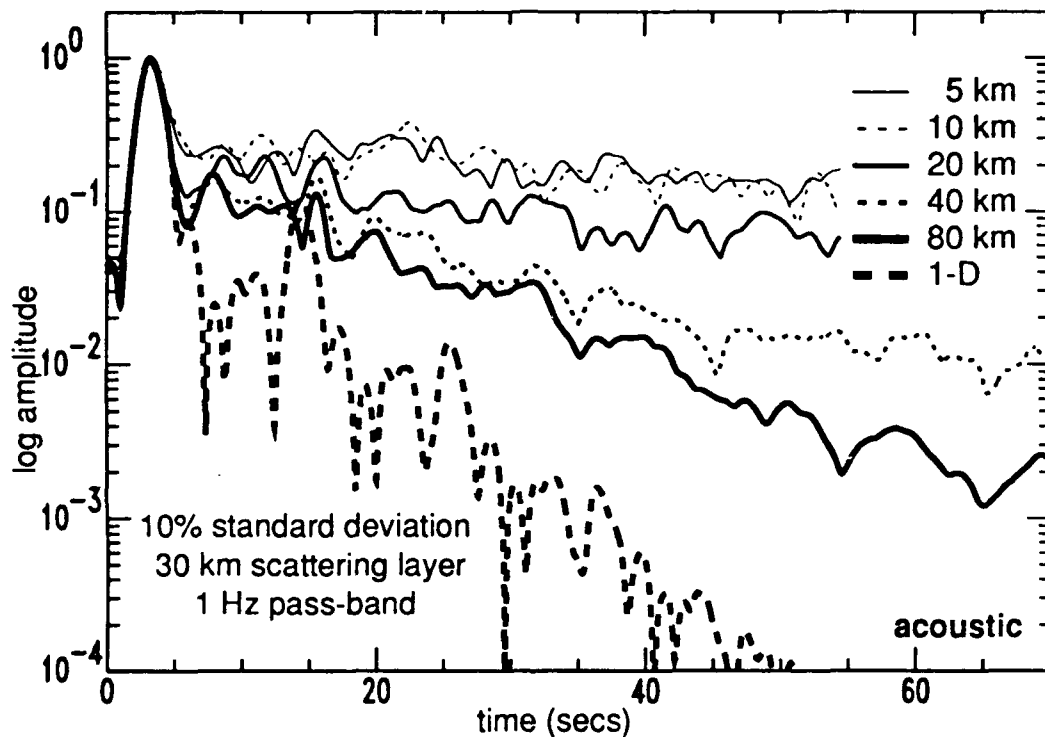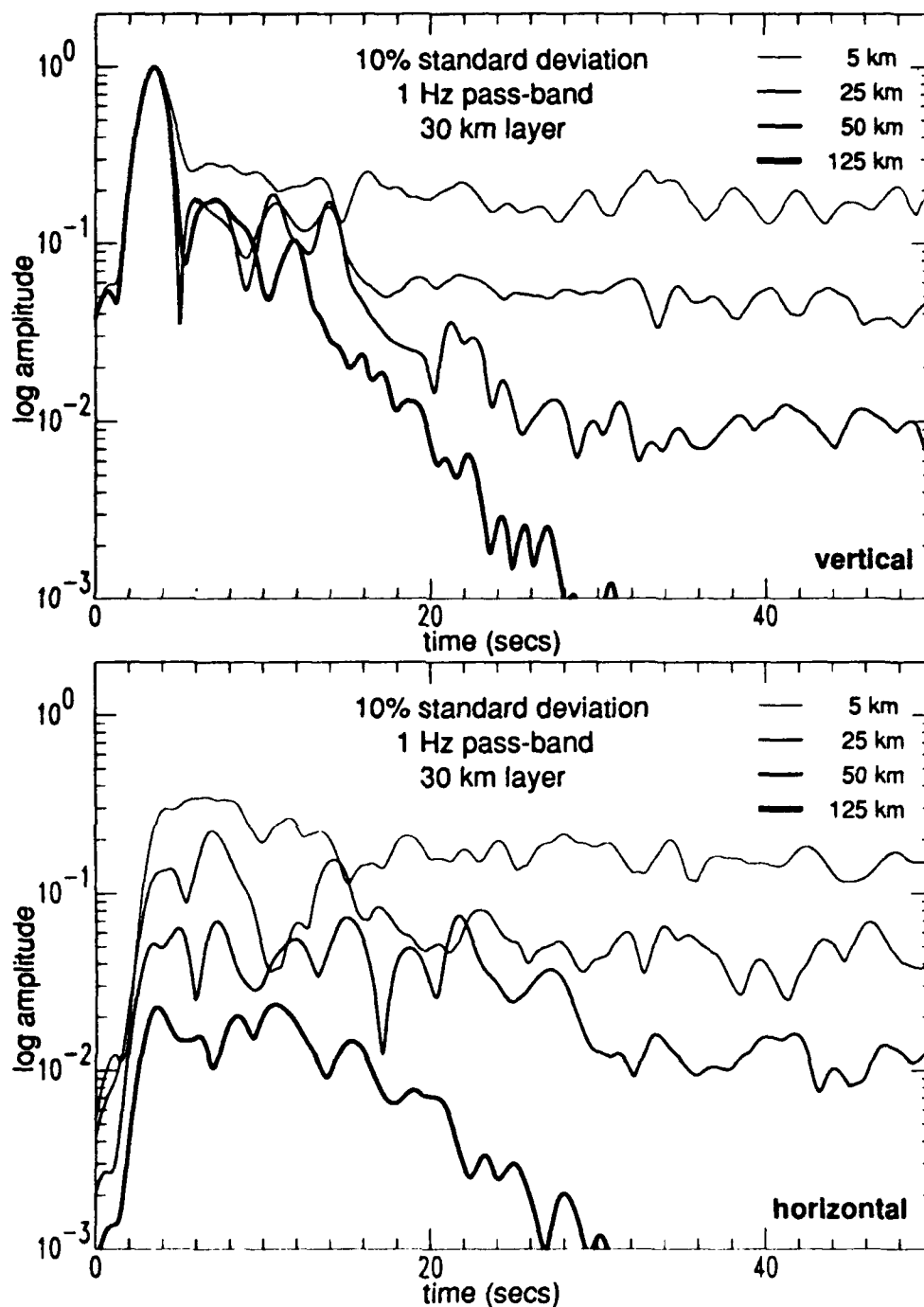
Changes in a_x with a Fixed a_z (5km)

Figure 10: Relative acoustic coda intensity envelopes for models with spatially
anisotropic heterogeneities varying in horizontal correlation
distance. Horizontal correlation distances and corresponding line
weights are shown in the upper-right corner of the figure. The
pass-band, scattering layer thickness and standard deviation are also
listed on the figure.

Changes in a_x with a Fixed a_z (5km)

Figure 11: Relative elastic coda intensity envelopes for models with spatially anisotropic heterogeneities varying in horizontal correlation distance. Horizontal correlation distances and corresponding line weights are shown in the upper-right corner of the figure. The pass-band, scattering layer thickness, standard deviation and displacement component are also listed on the figure.

Coda Levels

anisotropic acoustic
models

isotropic acoustic
models

isotropic elastic models
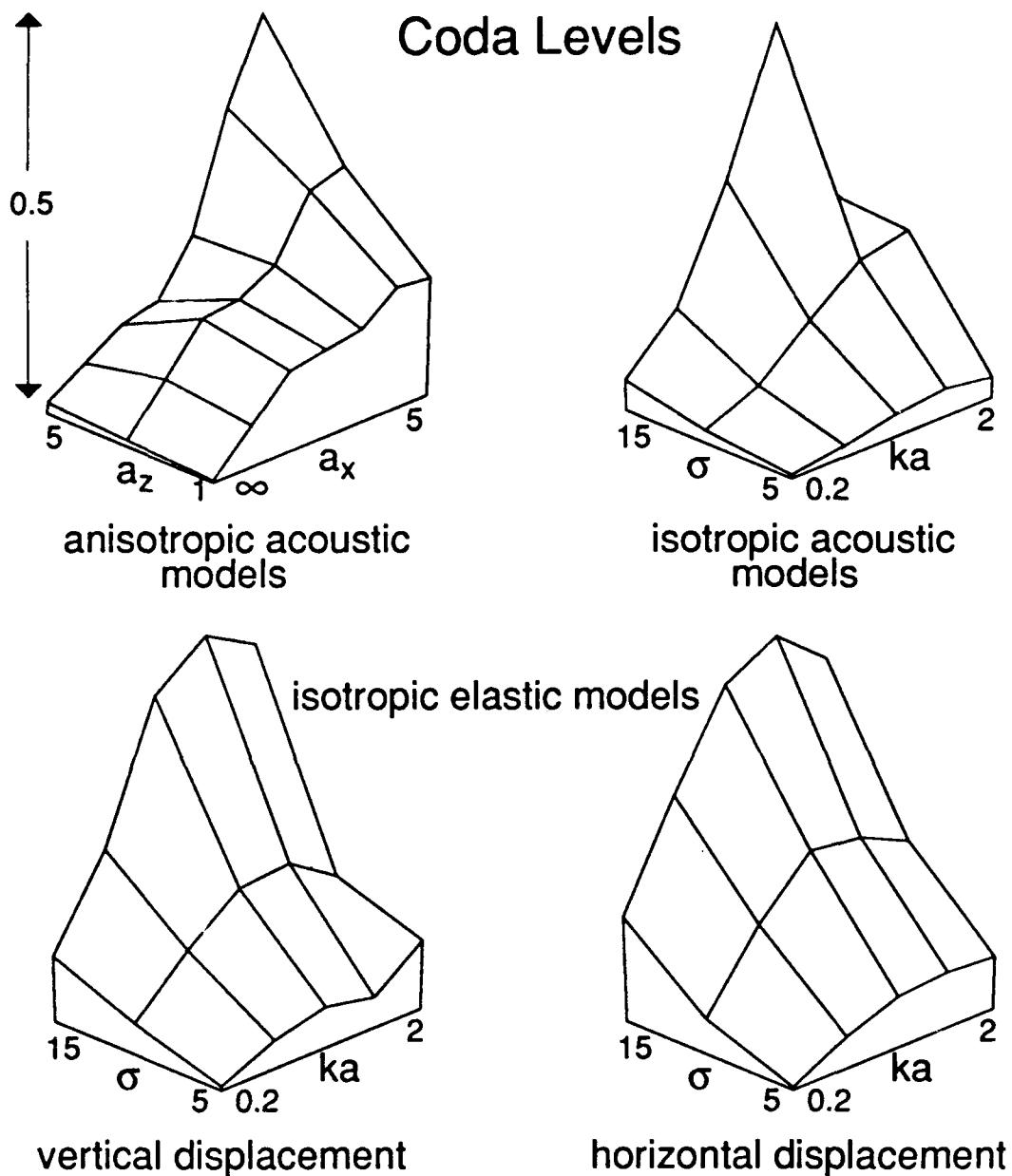
vertical displacement

horizontal displacement

Figure 12: Relative coda levels for a large range of models. The spatially
isotropic heterogeneity plots are for 1 Hz data for a 30 km thick
scattering layer. The anisotropic data are 1 Hz pass-band data for
a model with 10% standard deviation and a 30 km thick scattering
layer; ka is the normalized wavenumber, a_x and a_z are the
correlation distances in x and z, respectively (in km), and   is
the standard deviation in percent of the mean.

Coda Decay Rates

anisotropic acoustic
models

isotropic acoustic
models

isotropic elastic models

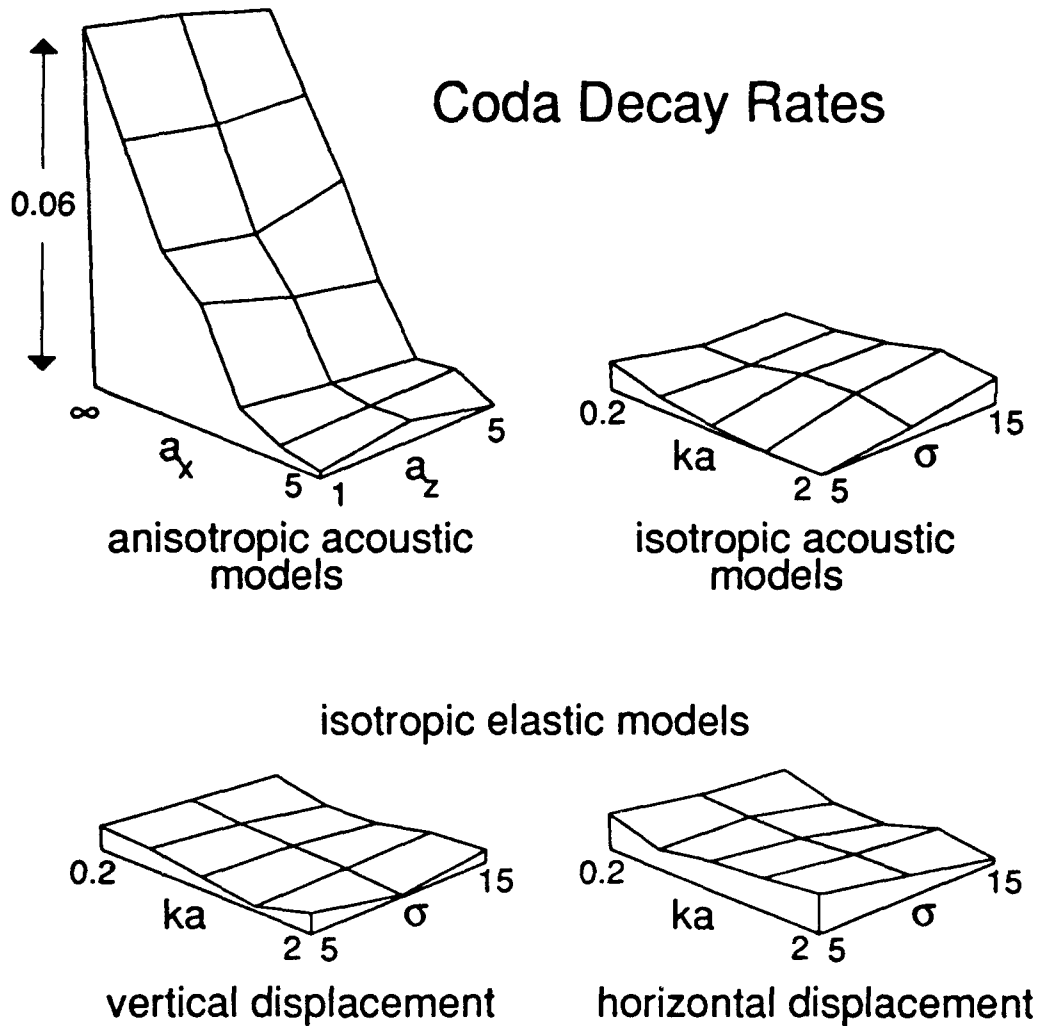vertical displacement

horizontal displacement

Figure 13: Relative coda decay rates for a large range of models. The
spatially isotropic heterogeneity plots are for 1 Hz data for a 30
km thick scattering layer. The anisotropic data are 1 Hz pass-band
data for a model with 10% standard deviation and a 30 km thick
scattering layer; ka is the normalized wavenumber, a_x and a_z are the
correlation distances in x and z, respectively (in km), and   is
the standard deviation in percent of the mean.
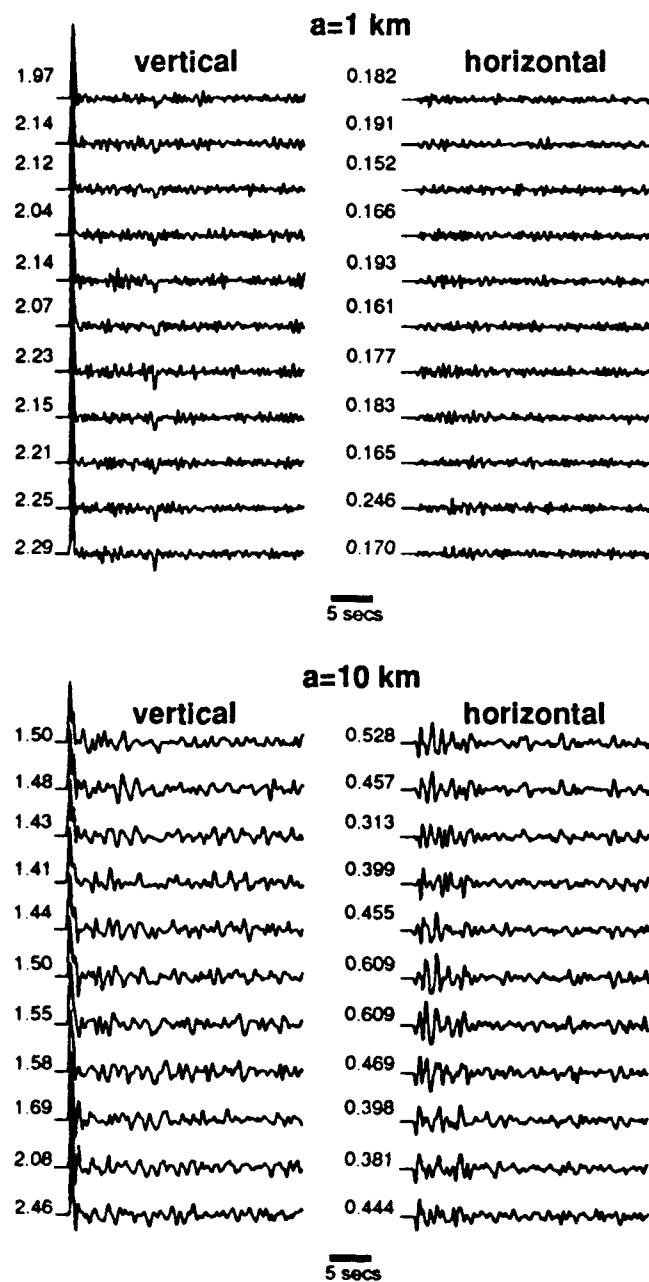
models with isotropic heterogeneities

a=1 km

vertical   horizontal

vertical	horizontal
1.97	0.182
2.14	0.191
2.12	0.152
2.04	0.166
2.14	0.193
2.07	0.161
2.23	0.177
2.15	0.183
2.21	0.165
2.25	0.246
2.29	0.170

5 secs

a=10 km

vertical   horizontal

vertical	horizontal
1.50	0.528
1.48	0.457
1.43	0.313
1.41	0.399
1.44	0.455
1.50	0.609
1.55	0.609
1.58	0.469
1.69	0.398
2.08	0.381
2.46	0.444

5 secs

Figure 14: Vertical and horizontal displacements generated using models with spatially isotropic heterogeneities with correlation distances of 1 km (top) and 10 km (bottom).
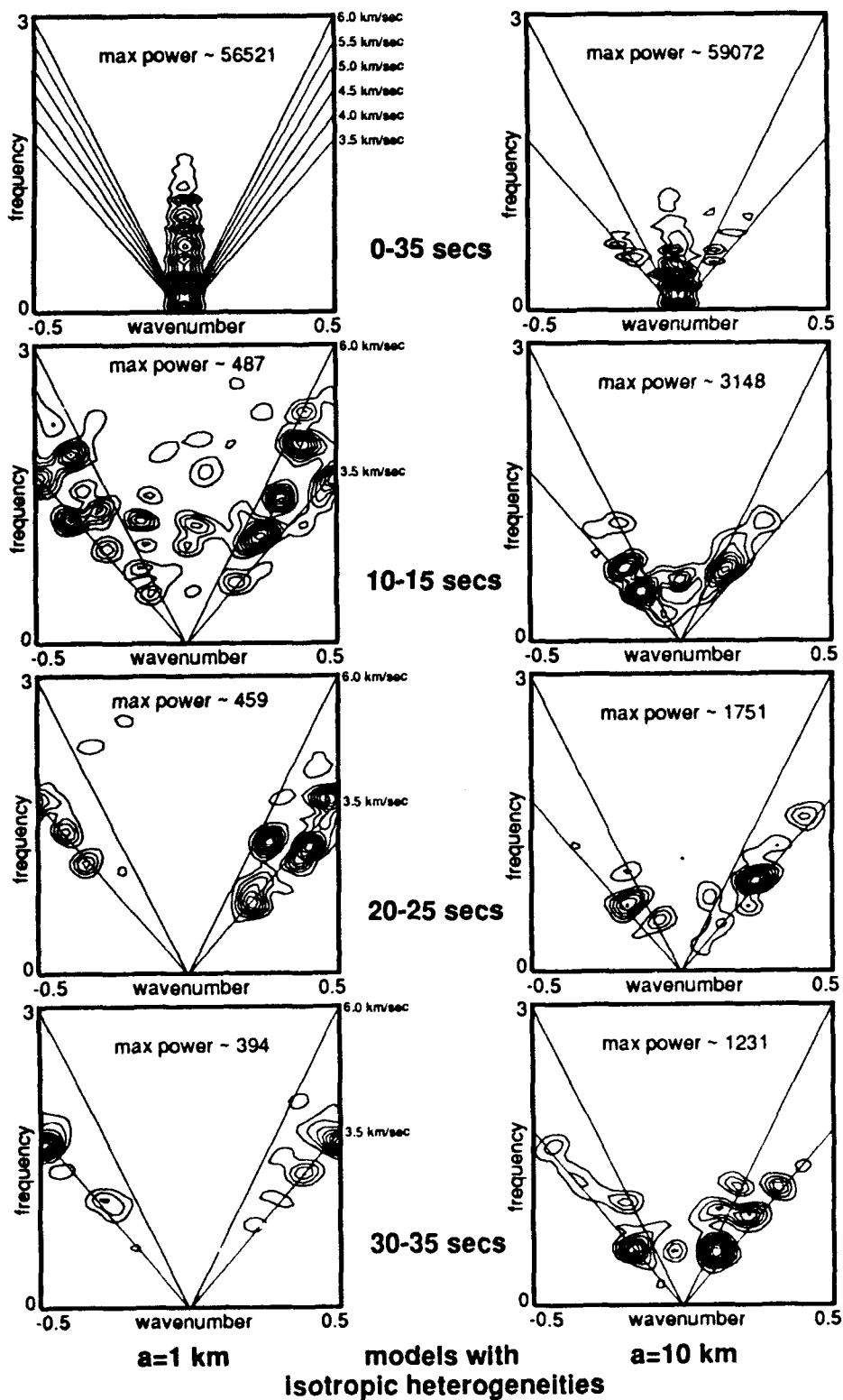
Figure 15: Frequency-wavenumber spectra for the data generated using models with spatially isotropic heterogeneities (Figure 14). Window durations, apparent velocities and estimated maximum power contents are shown with each spectra.

models with
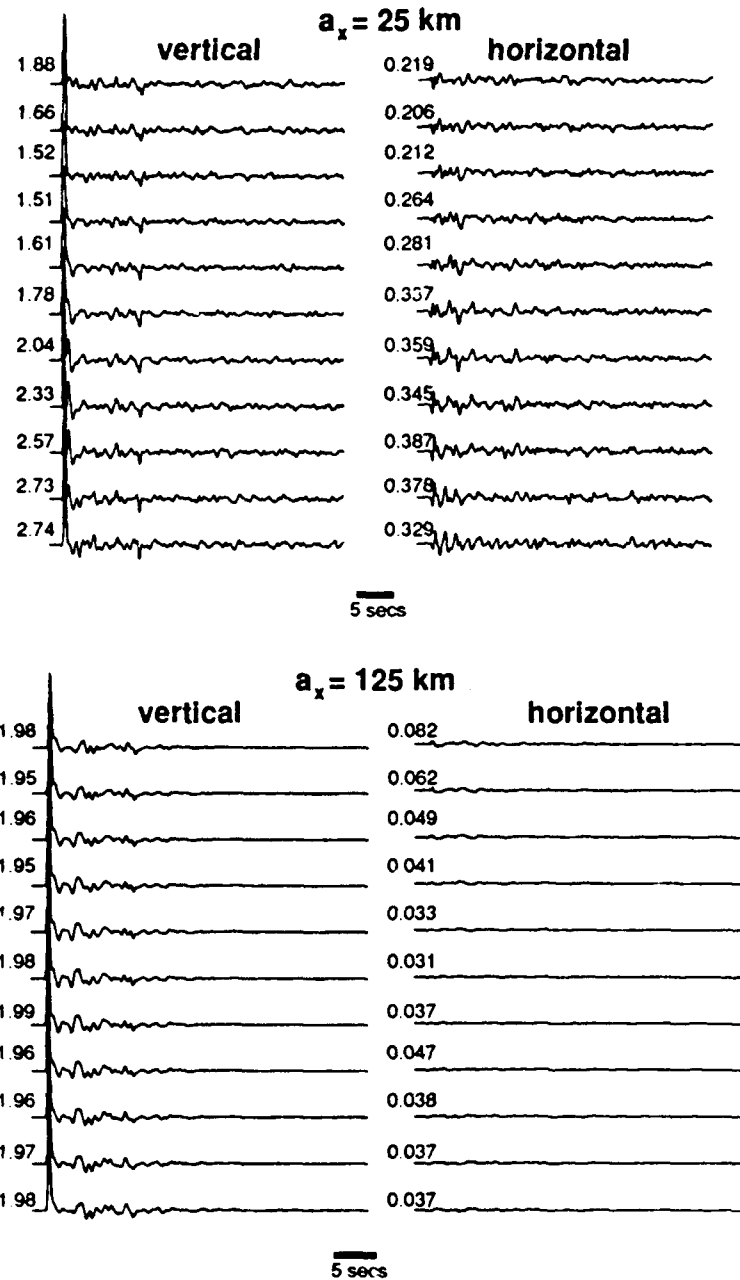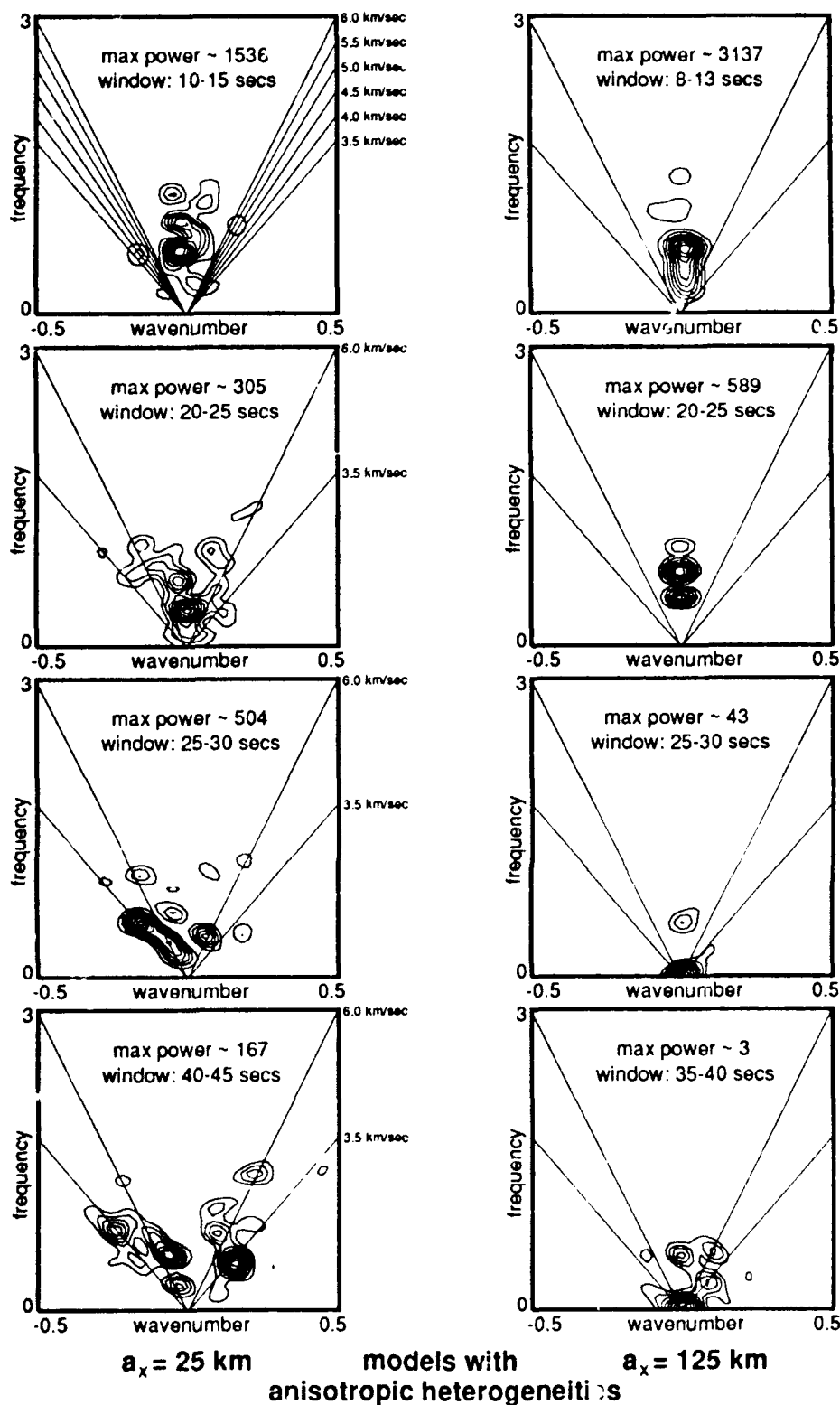# anisotropic heterogeneities

(a$_z$= 5 km for both)

a$_x$= 25 km

vertical   **horizontal**

1.88		0.219
1.66		0.206
1.52		0.212
1.51		0.264
1.61		0.281
1.78		0.337
2.04		0.359
2.33		0.345
2.57		0.387
2.73		0.378
2.74		0.329

5 secs

a$_x$= 125 km

vertical   **horizontal**

1.98		0.082
1.95		0.062
1.96		0.049
1.95		0.041
1.97		0.033
1.98		0.031
1.99		0.037
1.96		0.047
1.96		0.038
1.97		0.037
1.98		0.037

5 secs

Figure 16: Vertical and horizontal displacements generated using models with spatially anisotropic heterogeneities; a$_x$ =25 km for the top set and 125 km for the bottom set. a$_z$ =5 km for both sets.

Figure 17: Frequency-wavenumber spectra for the data generated using models with spatially anisotropic heterogeneities (Figure 16). Window durations, apparent velocities and estimated maximum power contents are shown with each spectra.

BODY-TO-SURFACE-WAVE SCATTERED ENERGY IN

TELESEISMIC CODA OBSERVED AT THE

NORESS SEISMIC ARRAY

Gregory S. Wagner[†] & Charles A. Langston
Department of Geosciences
The Pennsylvania State University
University Park, PA 16802

[†] all correspondence should be made with

Gregory Wagner
Department of Geological Sciences
University of South Carolina
Columbia, SC 29208

Abstract

Teleseismic data recorded at the NORESS seismic array are examined to determine the degree and scale of lithospheric heterogeneities beneath the array, and to locate local scattering sources. The data are examined using relative coda intensity envelopes, frequency-wavenumber spectra, and particle motion polarizations. The coda intensity envelopes do not exhibit any clear ka trends; the 0.5 Hz pass-band data does, however, contain higher energy levels and a high energy packet $\sim$15 seconds after the first arrival. Frequency-wavenumber analysis shows that most of the teleseismic coda is vertically propagating. The window centered near 15 seconds, however, contains energy traveling to the north-east at a low apparent velocity. Particle motions in this window follow a retrograde elliptical pattern characteristic of Rayleigh surface waves. The scattering source presumed to be responsible for the observed body-to-surface wave scattered energy is Lake Mjosa located approximately 50 km west-south-west of the array.

Introduction

Teleseismic data recorded at the NORESS array are examined to determine the degree of heterogeneity of the lithosphere beneath the array and to locate local scattering sources. The data examined in this study are from deep focus events (>350 km) located at angular distances between 135° and 140°. These events were selected for several reasons: (1) to ensure a nearly vertical angle of incidence at the array, (2) to ensure that the analysis window is as free as possible of major reflected, refracted and converted phases that would [immediately] follow the initial arrival from a shallow event, and (3) because deep focus events are thought to have [relatively] simple source functions. The goal was to obtain teleseismic coda that was generated by a single, vertically incident source pulse. We analyzed the data by comparing relative coda intensity envelopes (Frankel and Wennerberg, 1987; Langston, 1989; Wagner, 1991; Wagner and Langston, 1991), frequency-wavenumber spectra (Robinson, 1967; Gold and Rader, 1969; Capon, 1969; Beauchamp, 1973,1975; Claerbout, 1975; Ingate *et al.*, 1985; Nawab *et al.*, 1985; Kvaerna and Ringdal, 1986; Gupta *et al.*, 1990a,b), and particle motion polarizations (Harkrider, 1964).

Relative coda intensity envelopes for various pass-bands are compared in an attempt to reveal ka relationships that can be used to determine the correlation distance of the heterogeneities in the lithosphere beneath the array

(k is the wavenumber and a is the correlation distance used to parameterize lithospheric heterogeneities). For a medium whose perturbations can be characterized by a Gaussian correlation function, relative [teleseismic] coda levels are directly proportional to ka when $ka<1$, reach a maximum when $ka\sim1$, and are inversely proportional to ka when $ka>1$ (Frankel and Wennerberg, 1987; Langston, 1989; Wagner, 1991; Wagner and Langston, 1991). In addition, the relative [teleseismic] coda decay rates and the station to station signal coherence increase with the aspect ratio of the heterogeneities (a_x/a_z) (Wagner, 1991; Wagner and Langston, 1991).

Array data is used because wave propagation directions and apparent velocities can be easily determined using f-k analysis. In a study similar to this one, Gupta *et al.* (1990a,b) used f-k analysis on data generated by underground nuclear explosions in both the US and Soviet Union and identified a low apparent velocity arrival approaching form the south-west as body-to-surface wave scattered energy produced by the topographic perturbation associated with Lake Mjosa and the adjacent mountains. In addition to using f-k analysis to delineate wave types, we have used particle motion polarizations to further discriminate between body and surface waves.

The NORESS Array

The NORESS seismic array is a 25 component array located in southern Norway approximately 78 km NNE of Oslo (60.74° N, 11.54° E). Data used in this study are from the 25 vertical, short-period stations, and the 4 short-period 3-component stations. The stations are arranged in concentric rings with a maximum array diameter of 3 km. Figure 1 shows the location of the NORESS array and the array geometry.

Structurally, the NORESS array is located outside the Oslo graben in a region where the Moho dips slightly to the southeast (Kanestrom and Haugland, 1969; Sellevoll and Warrick, 1971). Of particular interest for this study is the presence of Lake Mjosa and the adjacent mountains. Together they account for about 1,000 meters of topographic relief. The lake is located approximately 50 km south-west of the array.

Event Descriptions

Data for 10 events recorded at the NORESS array were obtained from the Center for Seismic Studies [CSS]. All events had source depths greater than 300 km and were located at ranges beyond 135°. Deep focus events were selected to avoid complexities added by earth structure near the source, and because deep focus events are thought to have [relatively] simple, impulsive

mechanisms. Events at great distances were selected to insure that first arrivals had nearly vertical angles of incidence at the array. Deep focus, distant sources were also selected to, as best as possible, provide a fairly large window that contained only teleseismic coda. To insure that the coda do not contain other major phases, the hypocenter locations and corresponding travel-time-table-predicted arrivals were carefully examined for each event.

Of the 10 events examined, only 3 were analyzed in great detail Other events were rejected based on low signal to noise ratios; missing stations; complicated, non-impulsive initial arrivals; or because of the presence of several large-amplitude arrivals within the analysis window. All three events occurred in the Fiji Island/Tonga Trench region and are presumed to be associated with subduction of the Pacific plate under the Australia-India plate.

Table 1 shows the dates, source depths, source latitude and longitude, body wave magnitudes, and the first and second travel-time-table-predicted arrivals for the three events analyzed in detail. For brevity only the results from the 2/10/87 event will be presented in detail. Analysis of the other two events yielded nearly identical results.

February 10, 1987 Event

The observed arrivals for this event do not coincide with travel-time-table predictions for an event with a range of 138.3° and a depth of 395 km, the USGS

Preliminary Determination of Epicenters [PDE] location. In fact, fairly significant hypocenter relocation is required to match the observed arrivals with those predicted by travel-time-tables. If the USGS source depth is correct (395 km), the epicenter would have to be moved more than 150 km to produce arrival time separations observed in the data. The similarity of the data from this and the 4/1/86 event suggests that the mislocation may be mostly in depth. The observed arrivals can be matched with a depth change and very little or no change in the event's epicenter. Regardless of the mislocation problem, no travel-time-table predicted phases arrive within the analysis window. The first arrival is proceeded by low-amplitude energy which is only slightly above the noise level; this precursory energy was not included in the analysis window. Figure 2 shows data from the four 3-component stations.

Coda Envelope Analysis

Analysis of the coda envelopes in hopes of being able to determine the scale and degree of heterogeneity beneath the array was not as fruitful as hoped. The data were examined by comparing relative coda intensity envelopes for several frequency pass-bands in an attempt to reveal simple ka relationships (k is the wavenumber and a is the correlation distance used to parameterize the lithospheric heterogeneities). A Butterworth filter was used for 0.5, 1, 1.5 and

2 Hz pass-bands. The filter is 3 db down at the corner frequencies which were at ± 0.25 Hz of the frequency of interest. Unfortunately, ka relations revealed by comparing various pass-bands showed a limited range of applicability in synthetic data (Wagner, 1991; Wagner and Langston, 1991). Synthetics for teleseismic wave propagation through a randomly heterogeneous media (Gaussian correlation function) with a correlation distance a, the level of scattered energy was found to be proportional to ka when $ka<1$, but trends were not well defined for $ka>1$ (for the frequencies examined).

The data used to analyze the coda envelopes are from the four short-period, 3-component stations. The vertical and two horizontal intensity envelopes are shown in Figure 3. The coda level and decay rates for the 1, 1.5 and 2 Hz pass-bands are fairly similar, while the 0.5 Hz pass-band has a noticeably higher level and a lower decay rate. The 0.5 Hz pass-band is also anomalous in that it contains a second energy packet whose magnitude is equal to that of the initial arrival. This second, large-amplitude packet of energy suggests that there may be a separate scattering source responsible for some of the energy at 0.5 Hz. The horizontal 0.5 Hz pass-band data also contain this anomalously high energy packet which is greatest on the east-west component.

Frequency-Wavenumber Analysis

Frequency-wavenumber analysis was performed on the NORESS data to iden-
tify the wave types crossing the array, and to locate local scattering sources.
Of particular interest was the large energy packet in the 0.5 Hz pass-band
data arriving approximately 15 seconds after the initial arrival. Frequency-
wavenumber analysis was conducted on the vertical component only.

Several different f-k analyses methods are used: broad-band wavenumber,
narrow-band wavenumber, and frequency-wavenumber (see Figures 4, 5, and
6). Each of these methods provides slightly different information. The broad-
band wavenumber spectra show power as a function of k_r ($k_r^2 = k_x^2 + k_y^2$)
and θ (plan view angle of incidence) for no specific frequency. The narrow-
band wavenumber spectra show power at a specific frequency as a function of
k_x and k_y. The frequency-wavenumber spectra show power as a function of
frequency and one wavenumber/spatial dimension. For this 1-D [frequency-
wavenumber] analysis, the 2-D NORESS array must be collapsed into a linear
array. The broad- and narrow-band wavenumber spectra are used to determine
the azimuth of the line used in this projection.

Figure 4 shows the frequency-wavenumber signature of the incident pulse
(event 2/10/87) using the three different f-k analysis methods (broad-band
wavenumber, narrow-band wavenumber, and frequency-wavenumber). All three

spectra show that the incident pulse is traveling vertically (*i.e.* infinite apparent horizontal phase velocity). This figure also illustrates some of the differences in the signatures of the three different analysis methods.

Figure 5 shows spectra for three windows taken further back in the coda. Almost all of the coda had a nearly infinite apparent velocity [vertical angle of incidence] as is shown in Figure 5. This suggests, for the scale lengths examined in this study, that a plane layered or extremely high aspect ratio (a_x/a_z) model is a reasonable approximation for earth structure deep into the mantle beneath the array.

Analysis of the 5 second window starting 15 seconds after the first arrival revealed the presence of a significant amount of energy traveling to the northeast at a low apparent velocity. Figure 6 shows the three different frequency-wavenumber analysis methods for all three events listed in Table 1. Each of these spectra clearly show a significant amount of energy traveling to the northeast. The narrow-band wavenumber and frequency-wavenumber spectra show that this energy is traveling at approximately 3 km/sec. The three narrow-band wavenumber spectra in Figure 6 are for different frequencies to show that the energy was not limited to a narrow frequency band.

Figure 7 shows an additional [1-D] frequency-wavenumber spectra for a 60 second window that contains only coda; this figure shows that the this low phase velocity energy carries a majority of the coda's total energy.

The particle motion polarization for the data in the window containing the low phase velocity energy was examined to determine if the energy was propagating as a body or surface wave. Figure 8 shows the particle motion recorded at station C7 for the 2/10/87 event. This figure shows the unprocessed vertical component, and a horizontal component obtained by rotating the observed north-south and east-west components to a 225° back-azimuth. While the data in this window does not exhibit perfect retrograde elliptical motion associated with a fundamental mode Rayleigh wave, it is remarkably close considering no processing has been done to enhance the waveform.

The measured apparent velocity of ~ 3.0 km/sec and a travel time of approximately 15 seconds puts the scattering source responsible for the Rayleigh wave approximately 45 km away. Lake Mjosa and the adjacent mountains represent approximately 1,000 meters of topographic relief and are located approximately 50 km to the west-south-west (see Figure 1). The structural/topographic perturbation associated with the lake and mountains is presumed to be the source of the body-to-surface-wave scattered energy observed in all three events examined in this study. This conclusion is identical to that reached in several previous studies (Gupta *et al.*, 1990a,b; Banister *et al.*, 1990), all of which used markedly different types of sources.

Conclusions

Teleseismic coda from three deep focus earthquakes were examined to determine the degree and scale length of the heterogeneities in the lithosphere beneath the NORESS seismic array, and to search for local scattering sources. Relative coda decay rates were similar for the 1, 1.5 and 2 Hz pass-bands, but levels were higher and decay rates lower for the 0.5 Hz pass-b .... This suggests that heterogeneities in the NORESS region are on the order of 12 kilometers or greater. In addition to higher levels and lower decay rates, the 0.5 Hz pass-band data contains a packet of energy that arrives approximately 15 seconds after the first arrival. The energy contained in this packet is equivalent to that in the initial pulse.

Frequency-wavenumber analysis yielded two results. First, most of the observed coda had a nearly vertical angle of incidence suggesting that, for the scales examined in this study, a plane layered structure is a reasonable approximation deep into the mantle below the array. Secondly, the high energy packet of energy most readily observable on the 0.5 Hz pass-band coda envelopes corresponds to a low phase velocity (~ 3 km/sec) arrival coming from the south-west. All three events examined for this report produced this low phase velocity energy, despite marked differences in their spectral content. Particle motion polarizations showed that this low velocity energy exhibited retrograde

elliptical particle motion characteristic of a fundamental mode Rayleigh wave. The apparent velocity and arrival time of the Rayleigh wave put the scattering source responsible for its generation about 45 km to the south-west, the approximate location of Lake Mjosa. Lake Mjosa and the adjacent mountains represent a, approximately, 1,000 meter topographic perturbation that is presumed to be responsible for the body-to-surface wave scattering. These results concur with those of Gupta *et al.* (199a,b) who reached the same conclusion using a markedly different type of source.

Acknowledgments

References

Achenbach, J.D. (1984) *Wave Propagation in Elastic Solids*, Elsevier, New York.

Bannister, S.C., E.S. Husebye and B.O. Ruud (1990) Teleseismic *P* coda analyzed by three-component and array techniques: deterministic location of topographic *P*-to-R_g scattering near the NORESS array, *Bull. Seis. Soc. Am.*, 80(6), 1969–1986.

Beauchamp, K.G. (1973) *Signal Processing Using Analog and Digital Techniques*, George Allen and Unwin Ltd., London.

Beauchamp, K.G. (1975) *Exploitation of Seismograph Networks*, Nordhoff International Publishing, Leiden.

Blakeslee, S.N. and P.E. Malin (1990) A comparison of earthquake coda waves at surface versus subsurface seismometers, in press: *J. Geophys. Res.*, 95(B1), 309–326.

Boore, D.M., S.C. Harmsen and S.T. Harding (1981) Wave scattering from a step change in surface topography, *Bull. Seis. Soc. Am.*, 71(1), 117–125.

Capon, J. (1969) High-resolution frequency-wavenumber spectrum analysis, *Proceedings of the IEEE*, **57**(8), 1408–1418.

Claerbout, J.F. (1976) *Fundamentals of Geophysical Data Processing With Applications to Petroleum Prospecting*, McGraw-Hill, New York.

Frankel, A. and L. Wennerberg (1987) Energy-flux model of seismic coda: separation of scattering and intrinsic attenuation, *Bull. Seis. Soc. Am.*, **77**(4), 1223–1251.

Gilbert, F. and L. Knopoff (1960) Seismic scattering from topographic irregularities, *J. Geophy. Res.*, **65**, 3437–3444.

Gold, B. and C.M. Rader (1969) *Digital Processing of Signals*, McGraw-Hill, New York.

Greenfield, R.J. (1971) Short-period *P*-Wave generation by Rayleigh-wave scattering at Novaya Zemyla, *J. Geophys. Res.*, **76**(32), 7988–8001.

Gupta, I.N., C.S. Lynn and R.A. Wagner (1990a) Broadband *f-k* analysis of array data to identify sources of local scattering, *Geophys. Res. Ltrs.*, **17**(2), 183–186.

Gupta, I.N., C.S. Lynn, T.W.McElfresh and R.A. Wagner (1990b) F-K analysis of NORESS array and single station data to identify sources of near-receiver

and near-source scattering, *Bull. Seis. Soc. Am.*, **80**(6), 2227-2241.

Harkrider, D.G. (1964) Surface waves in multilayered elastic media: I. Rayleigh and Love wave from buried sources in a multilayered elastic half-space, *Bull. Seis. Soc. Am.*, **54**, 627-679.

Hill, N.R. and A.L. Levander (1984) Resonances of low-velocity layers with lateral variations, *Bull. Seis. Soc. Am.*, **74**(2), 521-537.

Hudson, J.A. (1967) Scattered surface waves from a surface obstacle, *Geophys. J. R. astr. Soc.*, **13**, 441-458.

Hudson, J.A. and D.M. Boore (1980) Comments on "scattered surface waves from a surface obstacle" by J.A. Hudson, *Geophys. J. R. astr. Soc.*, **60**, 123-127.

Ingate, S.F., E.S. Husebye and A. Christoffersson (1985) Regional arrays an optimum data processing schemes, *Bull. Seis. Soc. Am.*, **75**, 1155-1177.

Kanasewich, E.R. (1981) *Time Sequence Analysis in Geophysics*, University of Alberta Press, Winnipeg, Canada.

Kanestrom, R. and K. Haugland (1971) Profile section 3-4, in: *Proceedings of the colloquium on deep seismic soundings in northern Europe* (A. Vogel, ed.), Swedish Natural Research Council, Stockholm.

Key, F.A. (1967) Signal-generated noise recorded at the Eskdalemuir seismometer array station, *Bull. Seis. Soc. Am.*, **57**, 27-37.

Kvaerna, T. and F. Ringdal (1986) Stability of various *f-k* estimation techniques, *NORSAR Scientific Rep. 1-86/87*, 29-40, Kjeller, Norway.

Langston, C.A. (1989) Scattering of teleseismic body waves under Pasadena, California, *J. Geophys. Res.*, **94**, 1935-1951.

Levander, A.R. and N.R. Hill (1985) *P-S* resonances in irregular low-velocity surface layers, *Bull. Seis. Soc. Am.*, **75**(3), 847-864.

Nawab, S.H., F.U. Dowla and R.T. Lacoss (1985) Direction determination of wideband signals *IEEE Trans on Acoustics, Speech and Signal Processing*, **ASSP-33**(4), 1114-1122.

Rayleigh, J.W.S. (1894) *The Theory of Sound:* vols I & II, MacMillan Co., reprinted by Dover Publications Inc. (1945), New York.

Robinson, E.R. (1967) *Statistical Communications and Detection*, Charles Griffin and Co., London.

Sellevoll, M.A. and R.E. Warrick (1971) Refraction study of the crustal structure in southern Norway, *Bull. Seis. Soc. Am.*, **61**(2), 457-471.

Wagner, G.S. (1991) Scattering effects for teleseismic plane wave propagation

in a heterogeneous layer over a homogeneous half-space, *Ph.D. thesis*, The Pennsylvania State University, University Park, Pennsylvania, 285 pp.

Wagner, G. and C. Langston (1991) Scattering effects for teleseismic plane wave propagation in a heterogeneous layer over a homogeneous half-space, submitted: *Geophysical Journal International.*

Table 1

Dates source depths, source latitude and longitude, body wave magnitudes, and the first and second travel-time-table-predicted arrivals for the three events analyzed in this study

Event	$z\ (km)$	$\Delta°$	Lat°.	Long°.	M_b	1st and 2nd arrivals	
4/1/86	541	136.6	17.9 s	178.6 w	5.8	P''	pP'' @124 secs
2/10/87	395^+	138.3	19.5 s	177.5 w	6.2	P''	pP'' @122 secs
3/10/88	617	139.5	20.9 s	178.7 w	6.0	P''	pP'' @140 secs
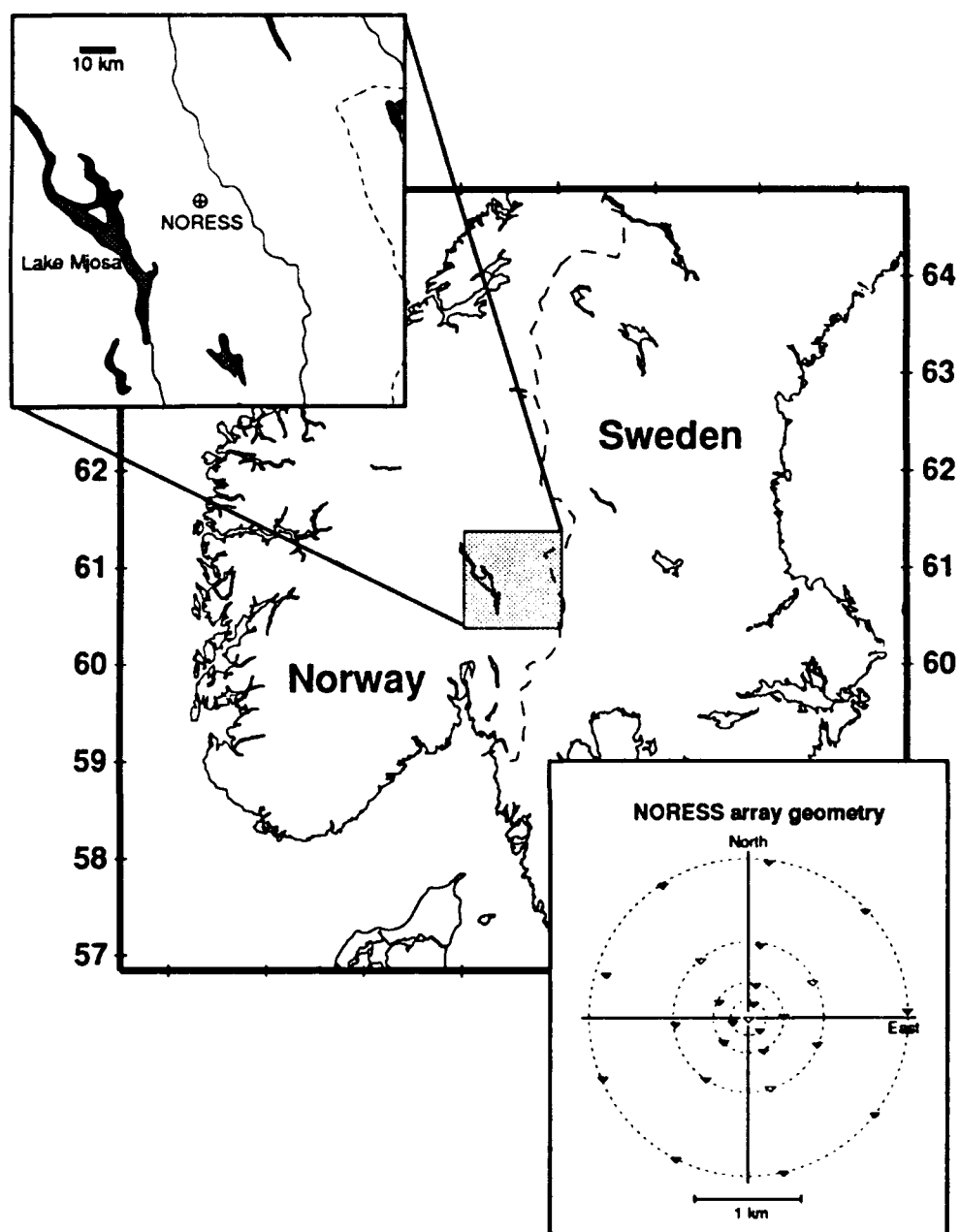
Figure 1: Location of the NORESS array and the array geometry. The solid
triangles represent vertical component, short-period instrument
locations. The empty tiangles denote the location of three-
component sensors.

3-Component Short-Period NORESS Data
(2/10/87 event)
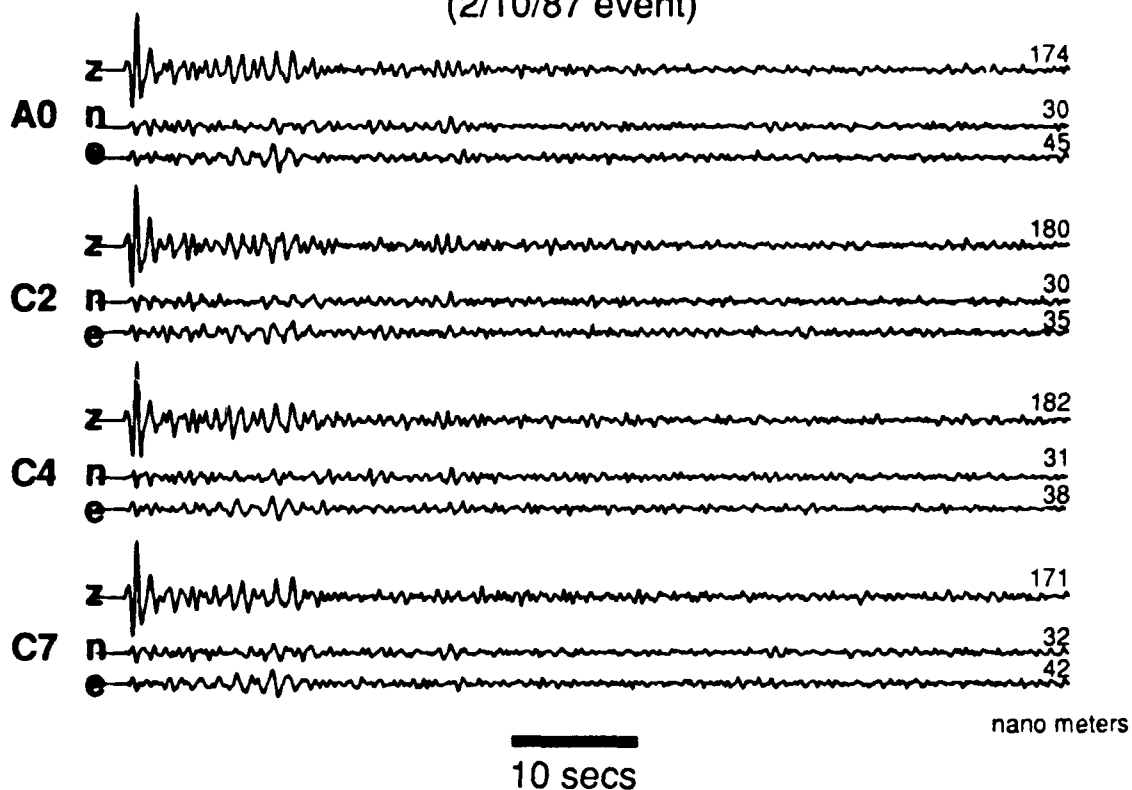
Figure 2: Vertical and horizontal short-period NORESS data for the 2/10/87
event. The station and maximum amplitude (nanometers) are shown
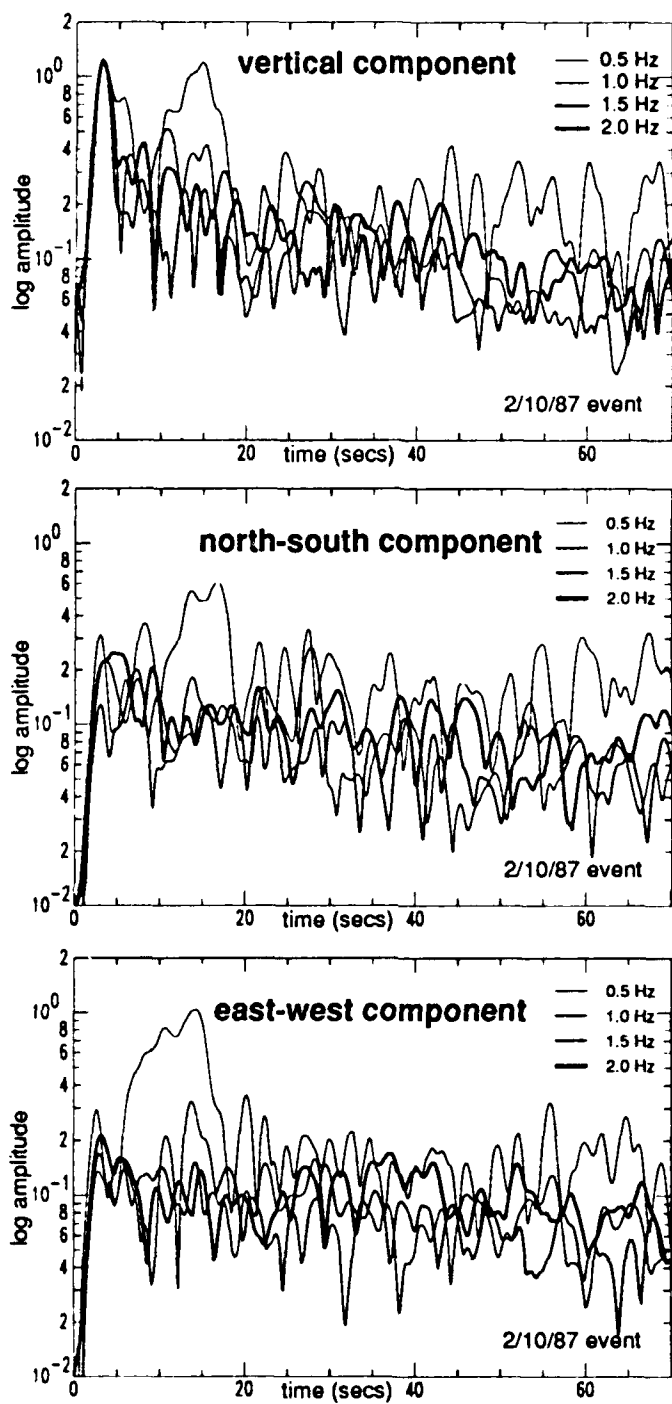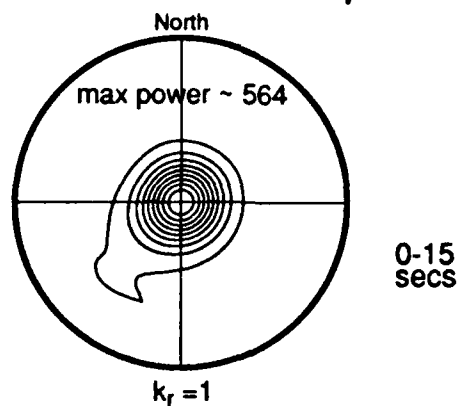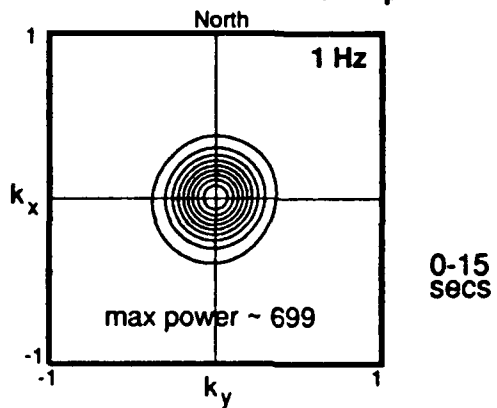above each trace. Vertical, north and east components are denoted
by z, n and e, respectively.

Figure 3: Stacked intensity envelopes for various pass-bands for the vertical and two horizontal components for the 2/10/87 event. The components, various pass-bands and corresponding line weights are shown in each panel.

Broad-Band Wavenumber Spectrum

North

max power ~ 564

0-15
secs

$k_r = 1$

Narrow-Band Wavenumber Spectrum

North

1 Hz

k_x

0-15
secs

max power ~ 699

-1

-1 k_y 1

Frequency-Wavenumber Spectrum

5   5 km/sec

max power ~ 174

4 km/sec
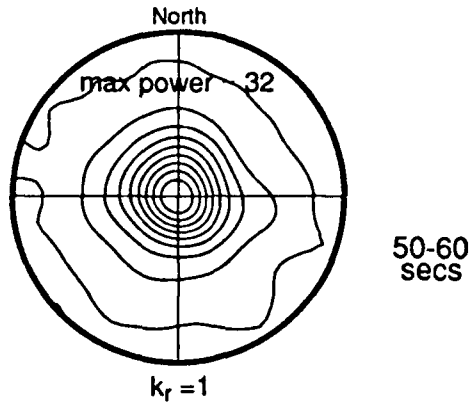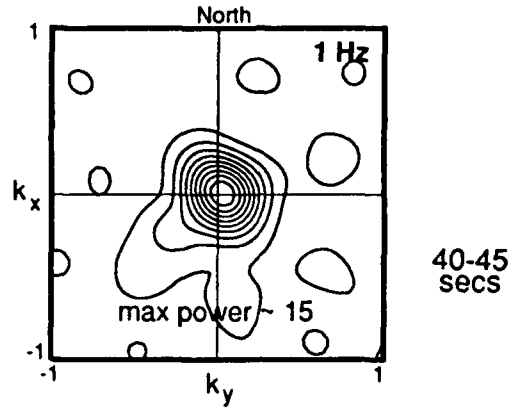
3 km/sec

frequency

0-15
secs

0
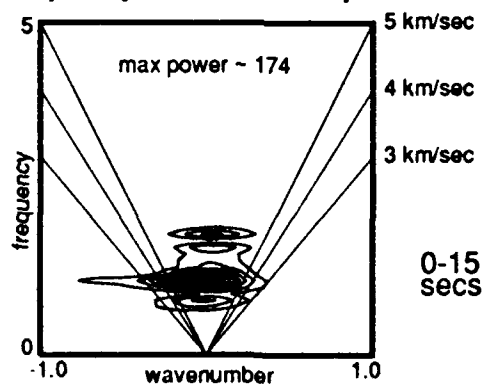
-1.0   wavenumber   1.0

Figure 4: Wavenumber spectra for the 0-15 second window of the vertical
component for the 2/10/87 event.

Broad-Band Wavenumber Spectrum

North

max power ~ 32

50-60
secs

$k_f = 1$

Narrow-Band Wavenumber Spectrum

North

1 Hz

k_x

max power ~ 15

40-45
secs

k_y

Frequency-Wavenumber Spectrum

5 km/sec

max power ~ 5

4 km/sec

3 km/sec
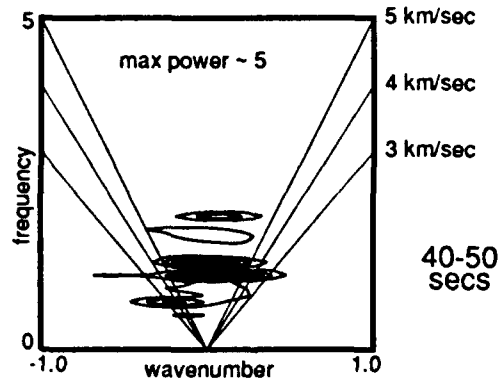
frequency
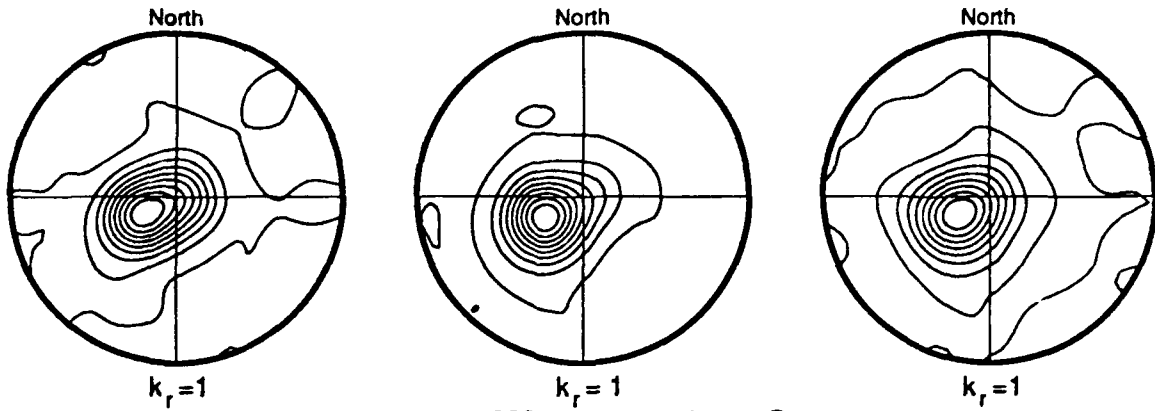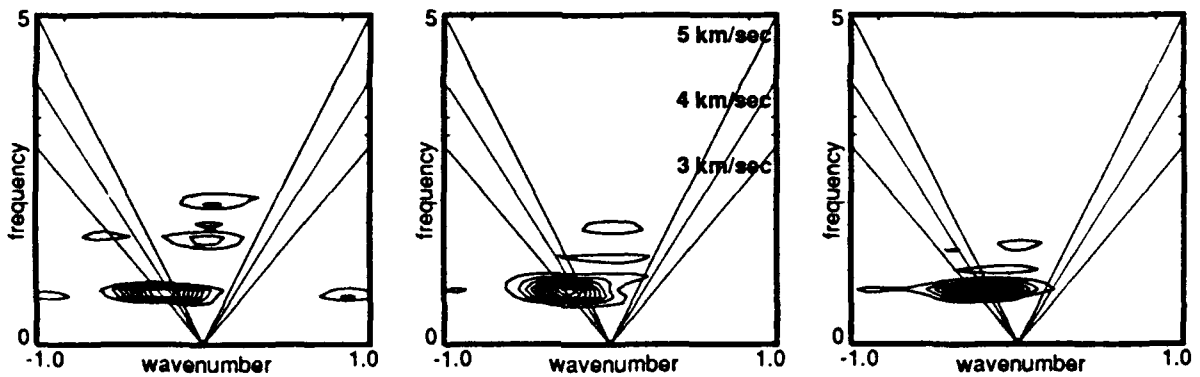
40-50
secs

-1.0   wavenumber   1.0

Figure 5: Wavenumber spectra for randomly selected windows of the vertical
component for the 2/10/87 event.

Broad-Band Wavenumber Spectra

Frequency-Wavenumber Spectra
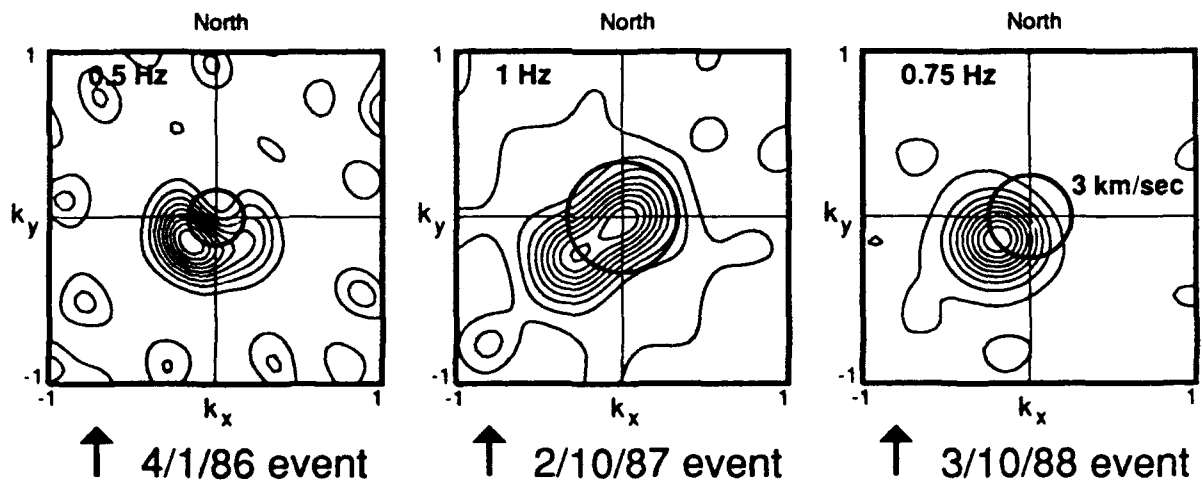

Narrow-Band Wavenumber Spectra

Figure 6: Frequency-wavenumber spectra for the 15-20 second window for three events.

Frequency-Wavenumber Spectrum
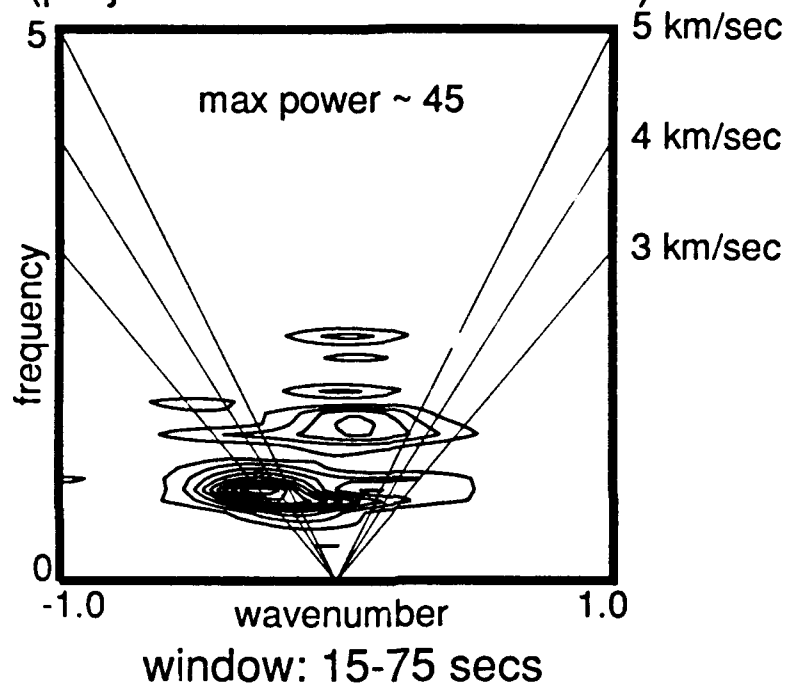(projection: 225° back azimuth)

Figure 7: One-dimensional f-k spectrum for the 15-75 second window of the vertical component for the 2/10/87 event.
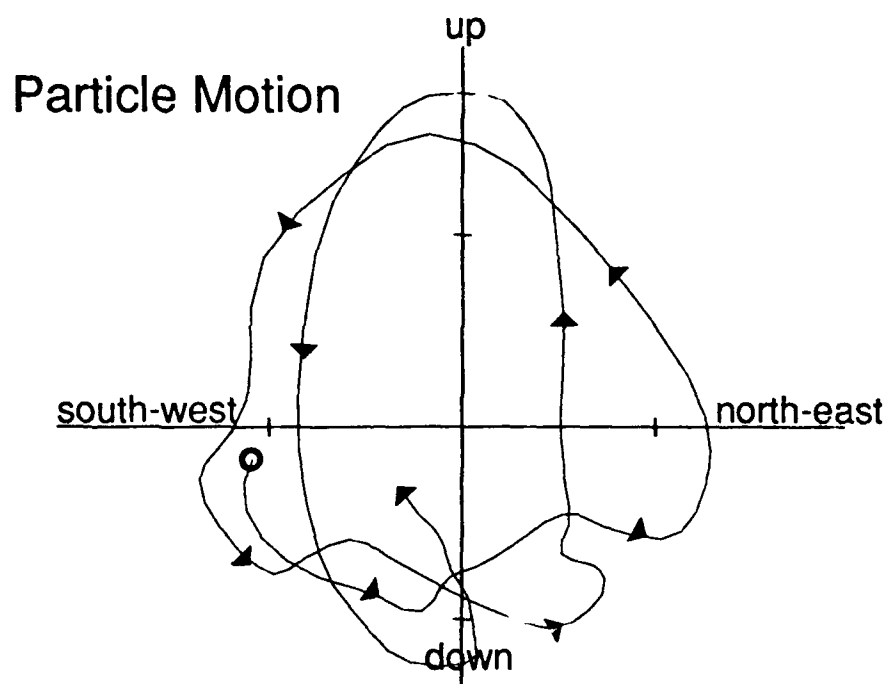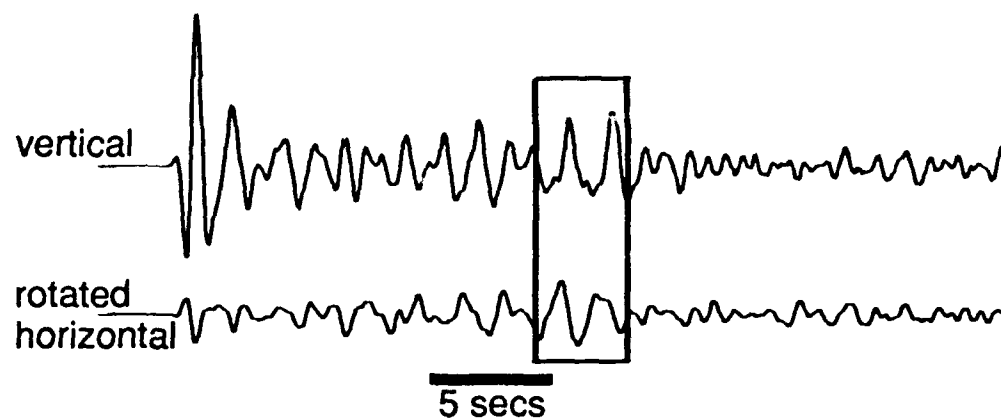
Figure 8: Particle motion for the unprocessed vertical, and rotated (to 45 degrees) horizontal components of motion at station C7 for the 2/10/87 event The circle on the particle motion diagram marks the window start, and arrow-heads point in the direction of increasing time. The exact analysis window is shown with the data.

Prof. Thomas Ahrens
Seismological Lab, 252-21
Division of Geological & Planetary Sciences
California Institute of Technology
Pasadena, CA 91125

Prof. Keiiti Aki
Center for Earth Sciences
University of Southern California
University Park
Los Angeles, CA 90089-0741

Prof. Shelton Alexander
Geosciences Department
403 Deike Building
The Pennsylvania State University
University Park, PA 16802

Dr. Ralph Alewine, III
DARPA/NMRO
3701 North Fairfax Drive
Arlington, VA 22203-1714

Prof. Charles B. Archambeau
CIRES
University of Colorado
Boulder, CO 80309

Dr. Thomas C. Bache, Jr.
Science Applications Int'l Corp.
10260 Campus Point Drive
San Diego, CA 92121 (2 copies)

Prof. Muawia Barazangi
Institute for the Study of the Continent
Cornell University
Ithaca, NY 14853

Dr. Jeff Barker
Department of Geological Sciences
State University of New York
 at Binghamton
Vestal, NY 13901

Dr. Douglas R. Baumgardt
ENSCO, Inc
5400 Port Royal Road
Springfield, VA 22151-2388

Dr. Susan Beck
Department of Geosciences
Building #77
University of Arizona
Tuscon, AZ 85721

Dr. T.J. Bennett
S-CUBED
A Division of Maxwell Laboratories
11800 Sunrise Valley Drive, Suite 1450
Reston, VA 22091

Dr. Robert Blandford
AFTAC/TT, Center for Seismic Studies
1330 North 17th Street
Suite 1450
Arlington, VA 22209-2308

Dr. G.A. Bollinger
Department of Geological Sciences
Virginia Polytechnical Institute
21044 Derring Hall
Blacksburg, VA 24061

Dr. Stephen Bratt
Center for Seismic Studies
1300 North 17th Street
Suite 1450
Arlington, VA 22209-2308

Dr. Lawrence Burdick
Woodward-Clyde Consultants
566 El Dorado Street
Pasadena, CA 91109-3245

Dr. Robert Burridge
Schlumberger-Doll Research Center
Old Quarry Road
Ridgefield, CT 06877

Dr. Jerry Carter
Center for Seismic Studies
1300 North 17th Street
Suite 1450
Arlington, VA 22209-2308

Eric Chael
Division 9241
Sandia Laboratory
Albuquerque, NM 87185

Prof. Vernon F. Cormier
Department of Geology & Geophysics
U-45, Room 207
University of Connecticut
Storrs, CT 06268

Prof. Anton Dainty
Earth Resources Laboratory
Massachusetts Institute of Technology
42 Carleton Street
Cambridge, MA 02142

Prof. Steven Day
Department of Geological Sciences
San Diego State University
San Diego, CA 92182

Art Frankel
U.S. Geological Survey
922 National Center
Reston, VA 22092

Marvin Denny
U.S. Department of Energy
Office of Arms Control
Washington, DC 20585

Dr. Cliff Frolich
Institute of Geophysics
8701 North Mopac
Austin, TX 78759

Dr. Zoltan Der
ENSCO, Inc.
5400 Port Royal Road
Springfield, VA 22151-2388

Dr. Holly Given
IGPP, A-025
Scripps Institute of Oceanography
University of California, San Diego
La Jolla, CA 92093

Prof. Adam Dziewonski
Hoffman Laboratory, Harvard University
Dept. of Earth Atmos. & Planetary Sciences
20 Oxford Street
Cambridge, MA 02138

Dr. Jeffrey W. Given
SAIC
10260 Campus Point Drive
San Diego, CA 92121

Prof. John Ebel
Department of Geology & Geophysics
Boston College
Chestnut Hill, MA 02167

Dr. Dale Glover
Defense Intelligence Agency
ATTN: ODT-1B
Washington, DC 20301

Eric Fielding
SNEE Hall
INSTOC
Cornell University
Ithaca, NY 14853

Dr. Indra Gupta
Teledyne Geotech
314 Montgomery Street
Alexanderia, VA 22314

Dr. Mark D. Fisk
Mission Research Corporation
735 State Street
P.O. Drawer 719
Santa Barbara, CA 93102

Dan N. Hagedon
Pacific Northwest Laboratories
Battelle Boulevard
Richland, WA 99352

Prof Stanley Flatte
Applied Sciences Building
University of California, Santa Cruz
Santa Cruz, CA95064

Dr. James Hannon
Lawrence Livermore National Laboratory
P.O. Box 808
L-205
Livermore, CA 94550

Dr. John Foley
NER-Geo Sciences
1100 Crown Colony Drive
Quincy, MA 02169

Dr. Roger Hansen
AFTAC/TTR
Patrick AFB, FL 32925

Prof. Donald Forsyth
Department of Geological Sciences
Brown University
Providence, RI 02912

Prof. David G. Harkrider
Seismological Laboratory
Division of Geological & Planetary Sciences
California Institute of Technology
Pasadena, CA 91125

Prof. Danny Harvey
CIRES
University of Colorado
Boulder, CO 80309

Prof. Donald V. Helmberger
Seismological Laboratory
Division of Geological & Planetary Sciences
California Institute of Technology
Pasadena, CA 91125

Prof. Eugene Herrin
Institute for the Study of Earth and Man
Geophysical Laboratory
Southern Methodist University
Dallas, TX 75275

Prof. Robert B. Herrmann
Department of Earth & Atmospheric Sciences
St. Louis University
St. Louis, MO 63156

Prof. Lane R. Johnson
Seismographic Station
University of California
Berkeley, CA 94720

Prof. Thomas H. Jordan
Department of Earth, Atmospheric &
  Planetary Sciences
Massachusetts Institute of Technology
Cambridge, MA 02139

Prof. Alan Kafka
Department of Geology & Geophysics
Boston College
Chestnut Hill, MA 02167

Robert C. Kemerait
ENSCO, Inc.
445 Pineda Court
Melbourne, FL 32940

Dr. Max Koontz
U.S. Dept. of Energy/DP 5
Forrestal Building
1000 Independence Avenue
Washington, DC 20585

Dr. Richard LaCoss
MIT Lincoln Laboratory, M-200B
P.O. Box 73
Lexington, MA 02173-0073

Dr. Fred K. Lamb
University of Illinois at Urbana-Champaign
Department of Physics
1110 West Green Street
Urbana, IL 61801

Prof. Charles A. Langston
Geosciences Department
403 Deike Building
The Pennsylvania State University
University Park, PA 16802

Prof. Thorne Lay
Institute of Tectonics
Earth Science Board
University of California, Santa Cruz
Santa Cruz, CA 95064

Dr. William Leith
U.S. Geological Survey
Mail Stop 928
Reston, VA 22092

James F. Lewkowicz
Phillips Laboratory/GPEH
Hanscom AFB, MA 01731-5000

Mr. Alfred Lieberman
ACDA/VI-OA State Department Building
Room 5726
320-21st Street, NW
Washington, DC 20451

Prof. L. Timothy Long
School of Geophysical Sciences
Georgia Institute of Technology
Atlanta, GA 30332

Dr. Robert Masse
Denver Federal Building
Bos 25046, Mail Stop 967
Denver, CO 80225

Dr. Randolph Martin, III
New England Research, Inc.
76 Olcott Drive
White River Junction, VT 05001

Dr. Gary McCartor
Department of Physics
Southern Methodist University
Dallas, TX 75275

3

Prof. Thomas V. McEvilly
Seismographic Station
University of California
Berkeley, CA 94720

Prof. John A. Orcutt
IGPP, A-025
Scripps Institute of Oceanography
University of California, San Diego
La Jolla, CA 92093

Prof. Art McGarr
U.S. Geological Survey
Mail Stop 977
U.S. Geological Survey
Menlo Park, CA 94025

Prof. Jeffrey Park
Kline Geology Laboratory
P.O. Box 6666
New Haven, CT 06511-8130

Dr. Keith L. McLaughlin
S-CUBED
A Division of Maxwell Laboratory
P.O. Box 1620
La Jolla, CA 92038-1620

Howard Patton
Lawrence Livermore National Laboratory
L-025
P.O. Box 808
Livermore, CA 94550

Stephen Miller & Dr. Alexander Florence
SRI International
333 Ravenswood Avenue
Box AF 116
Menlo Park, CA 94025-3493

Dr. Frank Pilotte
HQ AFTAC/TT
Patrick AFB, FL 32925-6001

Prof. Bernard Minster
IGPP, A-025
Scripps Institute of Oceanography
University of California, San Diego
La Jolla, CA 92093

Dr. Jay J. Pulli
Radix Systems, Inc.
2 Taft Court, Suite 203
Rockville, MD 20850

Prof. Brian J. Mitchell
Department of Earth & Atmospheric Sciences
St. Louis University
St. Louis, MO 63156

Dr. Robert Reinke
ATTN; FCTVTD
Field Command
Defense Nuclear Agency
Kirtland AFB, NM 87115

Mr. Jack Murphy
S-CUBED
A Division of Maxwell Laboratory
11800 Sunrise Valley Drive, Suite 1212
Reston, VA 22091 (2 Copies)

Prof. Paul G. Richards
Lamont-Doherty Geological Observatory
 of Columbia University
Palisades, NY 10964

Dr. Keith K. Nakanishi
Lawrence Livermore National Laboratory
L-025
P.O. Box 808
Livermore, CA 94550

Mr. Wilmer Rivers
Teledyne Geotech
314 Montgomery Street
Alexandria, VA 22314

Dr. Carl Newton
Los Alamos National Laboratory
P.O. Box 1663
Mail Stop C335, Group ESS-3
Los Alamos, NM 87545

Dr. George Rothe
HQ AFTAC/TTR
Patrick AFB, FL 32925-6001

Dr. Bao Nguyen
AFTAC/TTR
Patrick AFB, FL 32925

Dr. Alan S. Ryall, Jr.
DARPA/NMRO
3701 North Fairfax Drive
Arlington, VA 22209-1714

Dr. Richard Sailor
TASC, Inc.
55 Walkers Brook Drive
Reading, MA 01867

Prof. Charles G. Sammis
Center for Earth Sciences
University of Southern California
University Park
Los Angeles, CA 90089-0741

Prof. Christopher H. Scholz
Lamont-Doherty Geological Observatory
 of Columbia University
Palisades, CA 10964

Dr. Susan Schwartz
Institute of Tectonics
1156 High Street
Santa Cruz, CA 95064

Secretary of the Air Force
(SAFRD)
Washington, DC 20330

Office of the Secretary of Defense
DDR&E
Washington, DC 20330

Thomas J. Sereno, Jr.
Science Application Int'l Corp.
10260 Campus Point Drive
San Diego, CA 92121

Dr. Michael Shore
Defense Nuclear Agency/SPSS
6801 Telegraph Road
Alexandria, VA 22310

Dr. Matthew Sibol
Virginia Tech
Seismological Observatory
4044 Derring Hall
Blacksburg, VA 24061-0420

Prof. David G. Simpson
IRIS, Inc.
1616 North Fort Myer Drive
Suite 1400
Arlington, VA 22209

Donald L. Springer
Lawrence Livermore National Laboratory
L-025
P.O. Box 808
Livermore, CA 94550

Dr. Jeffrey Stevens
S-CUBED
A Division of Maxwell Laboratory
P.O. Box 1620
La Jolla, CA 92038-1620

Lt. Col. Jim Stobie
ATTN: AFOSR/NL
Bolling AFB
Washington, DC 20332-6448

Prof. Brian Stump
Institute for the Study of Earth & Man
Geophysical Laboratory
Southern Methodist University
Dallas, TX 75275

Prof. Jeremiah Sullivan
University of Illinois at Urbana-Champaign
Department of Physics
1110 West Green Street
Urbana, IL 61801

Prof. L. Sykes
Lamont-Doherty Geological Observatory
 of Columbia University
Palisades, NY 10964

Dr. David Taylor
ENSCO, Inc.
445 Pineda Court
Melbourne, FL 32940

Dr. Steven R. Taylor
Los Alamos National Laboratory
P.O. Box 1663
Mail Stop C335
Los Alamos, NM 87545

Prof. Clifford Thurber
University of Wisconsin-Madison
Department of Geology & Geophysics
1215 West Dayton Street
Madison, WS 53706

Prof. M. Nafi Toksoz
Earth Resources Lab
Massachusetts Institute of Technology
42 Carleton Street
Cambridge, MA 02142

Dr. Larry Turnbull
CIA-OSWR/NED
Washington, DC 20505

DARPA/RMO/SECURITY OFFICE
3701 North Fairfax Drive
Arlington, VA 2203-1714

Dr. Gregory van der Vink
IRIS, Inc.
16116 North Fort Myer Drive
Suite 1440
Arlington, VA 22209

HQ DNA
ATTN: Technical Library
Washington, DC 20305

Dr. Karl Veith
EG&G
5211 Auth Road
Suite 240
Suitland, MD 20746

Defense Intelligence Agency
Directorate for Scientific & Technical Intelligence
ATTN: DTIB
Washington, DC 20340-6158

Prof. Terry C. Wallace
Department of Geosciences
Building #77
University of Arizona
Tuscon, AZ 85721

Defense Technical Information Center
Cameron Station
Alexandria, VA 22314 (5 Copies)

Dr. Thomas Weaver
Los Alamos National Laboratory
P.O. Box 1663
Mail Stop C335
Los Alamos, NM 87545

TACTEC
Battelle Memorial Institute
505 King Avenue
Columbus, OH 43201 (Final Report)

Dr. William Wortman
Mission Research Corporation
8560 Cinderbed Road
Suite 700
Newington, VA 22122

Phillips Laboratory
ATTN: XPG
Hanscom AFB, MA 01731-5000

Prof. Francis T. Wu
Department of Geological Sciences
State University of New York
 at Binghamton
Vestal, NY 13901

Phillips Laboratory
ATTN: GPE
Hanscom AFB, MA 01731-5000

AFTAC/CA
(STINFO)
Patrick AFB, FL 32925-6001

Dr. Michel Bouchon
I.R.I.G.M.-B.P. 68
38402 St. Martin D'Heres
Cedex, FRANCE

DAARPA/PM
3701 North Fairfax Drive
Arlington, VA 22203-1714

Dr. Michel Campillo
Observatoire de Grenoble
I.R.I.G.M.-B.P. 53
38041 Grenoble, FRANCE

DARPA/RMO/RETRIEVAL
3701 North Fairfax Drive
Arlington, VA 22203-1714

Dr. Kin Yip Chun
Geophysics Division
Physics Department
University of Toronto
Ontario, CANADA

Prof. Hans-Peter Harjes
Institute for Geophysics
Ruhr University/Bochum
P.O. Box 102148
4630 Bochum 1, GERMANY

Prof. Eystein Husebye
NTNF/NORSAR
P.O. Box 51
N-2007 Kjeller, NORWAY

David Jepsen
Acting Head, Nuclear Monitoring Section
Bureau of Mineral Resources
Geology and Geophysics
G.P.O. Box 378, Canberra, AUSTRALIA

Ms. Eva Johannisson
Senior Research Officer
National Defense Research Inst.
P.O. Box 27322
S-102 54 Stockholm, SWEDEN

Dr. Peter Marshall
Procurement Executive
Ministry of Defense
Blacknest, Brimpton
Reading FG7-FRS, UNITED KINGDOM

Dr. Bernard Massinon, Dr. Pierre Mechler
Societe Radiomana
27 rue Claude Bernard
75005 Paris, FRANCE (2 Copies)

Dr. Svein Mykkeltveit
NTNT/NORSAR
P.O. Box 51
N-2007 Kjeller, NORWAY (3 Copies)

Prof. Keith Priestley
University of Cambridge
Bullard Labs, Dept. of Earth Sciences
Madingley Rise, Madingley Road
Cambridge CB3 OEZ, ENGLAND

Dr. Jorg Schlittenhaardt
Federal Institute for Geosciences & Nat'l Res.
Postfach 510153
D-3000 Hannover 51, GERMANY

Dr. Johannes Schweitzer
Institute of Geophysics
Ruhr University/Bochum
P.O. Box 1102148
4360 Bochum 1, GERMANY